



HAL
open science

Ultrafast photogeneration and photodetection of coherent acoustic phonons in ferroelectric BiFeO₃

Mariusz Lejman

► **To cite this version:**

Mariusz Lejman. Ultrafast photogeneration and photodetection of coherent acoustic phonons in ferroelectric BiFeO₃. Materials Science [cond-mat.mtrl-sci]. Le Mans Université, 2015. English. NNT : 2015LEMA1015 . tel-01299211

HAL Id: tel-01299211

<https://theses.hal.science/tel-01299211>

Submitted on 7 Apr 2016

HAL is a multi-disciplinary open access archive for the deposit and dissemination of scientific research documents, whether they are published or not. The documents may come from teaching and research institutions in France or abroad, or from public or private research centers.

L'archive ouverte pluridisciplinaire **HAL**, est destinée au dépôt et à la diffusion de documents scientifiques de niveau recherche, publiés ou non, émanant des établissements d'enseignement et de recherche français ou étrangers, des laboratoires publics ou privés.

Thèse de Doctorat

Mariusz LEJMAN

*Mémoire présenté en vue de l'obtention du
grade de Docteur de l'Université du Maine
sous le label de L'Université Nantes Angers Le Mans*

École doctorale : *3MPL*

Discipline : *Physique*

Unité de recherche : *Institut des Molécules et Matériaux du Mans, UMR 6283 CNRS*

Soutenue le *06.10.15*

Ultrafast Photogeneration and Photodetection of Coherent Acoustic Phonons in Ferroelectric BiFeO₃

JURY

- Rapporteurs : **Matias BARGHEER, Professor, Potsdam University, Germany**
Bernard PERRIN, CNRS research director, INSP-Univ. Pierre et Marie Curie
- Examineurs : **Jens KREISEL, CNRS research director, LIST, Luxembourg**
Davide BOSCHETTO, Professor, LOA-Ecole Polytechnique, Palaiseau
- Invité(s) : **Brahim DKHIL, Professor, SPMS-CNRS, Centrale-Supelec**
- Directeur de Thèse : **Pascal RUELLO, Professor, IMMM-CNRS, Maine University**
- Co-directeur de Thèse : **Vitali GUSEV, Professor, LAUM-CNRS, Maine University**
- Co-superviseur de Thèse : **Gwenaëlle VAUDEL, Research Engineer, IMMM-CNRS, Maine University**

Acknowledgements

First of all I would like to express my gratitude to my PhD director Prof. Pascal Ruello. I'm very glad for his support and guidance during all my thesis. I would like to thank to Prof. Ruello for inspiring scientific discussions and substantive advice in order to improve my work.

I would also like to thank a lot to co-director of my PhD Prof. Vitaly Gussev for his valuable advices during my PhD and very reasonable look at all scientific issues connected to my topic.

Finally I would like to thank to my PhD co-supervisor Gwenaelle Vaudel for support in the laboratory and important assistance in the implementation of complex pump-probe experiment.

Subsequently I would like to express my gratitude to our collaborators Ingrid Canero Infante and Brahim Dkhil from Ecole Centrale Paris for preparation and preliminary characterization of great samples.

I would also like to thank to Mathieu Edely for devoted time and help in adaptation of some important samples for experiment as well as to Prof. Alain Bulou, Thomas Pezeril and Vasily Temnov for valuable scientific advices and discussions.

In the next, I would like to thank to my colleagues and friends, especially Sergey Nikitin and Victor Shalagaskyi for free scientific discussions and also Ievgienilia Chaban and Tymur Parpiiev for some company during PhD adventure.

I would like to especially thank to my friend Alla Abramova, I could always rely on her help and support. I would also like to thank to other people who have contributed to my PhD and to my friends not mentioned here.

Finally I'm very grateful to my mother for her support in difficult moments.

I would like to dedicate this work to my mother, to my sweetheart and to my little son Filip, who strongly motivated me to work hard and with whom I could not always be in the important moments of their lives.

Chapter 1 Introduction	9
Chapter 2 : Ultrafast acoustics, ultrafast phononics	13
2.1 Introduction	15
2.2 Principle of ultrafast acoustics, ultrafast phononics	15
2.2.1 Generalities about ultrafast acoustics.....	15
2.3. Generation mechanisms of high frequency phonons by pulsed lasers.....	19
2.3.1. Thermoelasticity (TE).....	19
2.3.2. Deformation potential (DP).....	22
2.3.3. Inverse piezoelectricity (PE).....	24
2.3.4. Electrostriction (ES).	26
2.4. Why ferroelectrics/multiferroics for ultrafast acoustics?	27
2.4.1. Introduction.....	27
2.4.2. Basics of piezoelectricity and ferroelectricity	28
2.4.3. Structure and general properties of bismuth ferrite (BFO).....	31
Chapter 3 : Generation and detection of coherent acoustic phonons in BiFeO₃	37
3.1 Introduction	39
3.2. Literature survey : Ultrafast electron and phonon dynamics and ultrafast strain in BFO.....	39
3.2.1. Study of ultrafast electron dynamics in BFO	39
3.2.2. Study of ultrafast photoinduced strain in BFO	44
3.3. Results : Ultrafast light-induced tunable LA and TA phonons source in BFO at room temperature	54
3.3.1. Sample preparation and characterization.....	54
3.3.2. Photoinduced coherent shear and longitudinal strain in specific orientations of BFO grains at GHz frequency.	57
3.4. Results : Role of magnetic ordering on the photogeneration and photodetection of coherent acoustic phonon in BFO (high temperature investigation)	78
3.4.1. Experimental conditions and procedure.....	79
3.4.2. Effect of temperature variation on generation and detection of acoustic phonons in ferroelectric BFO	79
3.5 Conclusion.....	86
Chapter 4 : Ultrafast mode conversion of light induced by coherent phonons in birefringent media	87
4.1. Introduction	89
4.2. Theory	89
4.3. Ultrafast mode conversion of light induced by coherent phonons in ferroelectric BFO	94
4.4. Ultrafast mode conversion of light induced by coherent phonons in ferroelectric lithium niobate (LNO)	99
4.4. Detection of LA phonons in birefringent crystal of calcite (CaCO ₃)	112
4.5. Calculations of detected light intensity changes by different scattering processes in simple geometries	116
4.6 Conclusion.....	120
Chapter 5. General Conclusion and perspectives	121
Appendix 1 : Pump-probe setup characteristics	127
Appendix 2 : Grain orientation probed by optical birefringence ...	131

Appendix 3 : Mode conversion in calcite axis oriented at 45 degrees
versus surface (rotation of photo-elastic tensor by 45 degrees).. 134
Bibliography 137

Chapter 1 Introduction

Ultrafast science is the study of physical phenomena and processes that occur on very short time scales ranging from attoseconds to picoseconds through femtoseconds. Ultrashort pulses of light generated by pulsed lasers enable to study fundamental mechanisms and interactions in matter. Currently laser pulses with duration of several femtoseconds at the limit corresponding to wavelength of light are obtained. Ultrafast science is concerned with the applications of pulsed lasers for time-domain measurements of ultrafast electronic and phononic processes in various media (mostly condensed matter). In the domain of pump-probe spectroscopy, a pump pulse excites the matter leading to trigger different dynamics (electron, phonon, spin), and a probe pulse detects evolution of processes with time resolution limited only to its duration.

Ultrashort pulses are used to observe chemical reactions on time scale they occur, what belongs to the field of femtochemistry. Nobel Prize in chemistry was awarded in 1999 for development and achievements in this discipline. Ultrashort lasers are employed in research of dynamics of electrons recombination, thermalization and spin relaxation as well as lattice dynamics, i.e. phonons. Mutual ultrafast interactions between these particles and quasi-particles are investigated simultaneously. Metals, semiconductor and complex oxides as well as nanostructures made of them were intensively studied in this way during last 30 years.

Furthermore, new kind of pump-probe spectroscopy has been developing recently very rapidly thanks to great progress of sources of ultrashort X-ray radiation (plasma source, synchrotron, X-free electron laser). This time resolved X-ray scattering employs pulses of X-ray radiation as probe pulses even at attoseconds time scales. As an example, time-resolved X-ray diffraction allows to study directly the lattice dynamics and can catch ultrafast strain or structural changes at phase transitions induced by pulsed laser excitation.

In the domain of picosecond acoustics (or ultrasonics), that is the field of the research presented in this manuscript, visible pump pulses are used to generate high frequency acoustic pulses in GHz up to THz frequency range. It corresponds to spatial extension of excited acoustic strain of the order of tens of nanometers, which is enough to resolve in space and investigate different properties of nanostructures like elastic, optical, electronic, and thermal. Subsequently probe pulses follow processes of generation propagation of acoustic phonons in studied medium.

Moreover picosecond acoustics allows to understand fundamental processes of conversion of optical energy into mechanical one, what is necessary to develop new sources of high frequency acoustic waves. Mechanisms of generation of acoustic phonons induced by light were investigated on the beginning in simplest materials as metals, then in semiconductors and currently attention is also focused on ferroelectrics.

Piezoelectric properties of ferroelectrics are used traditionally in generation of ultrasounds by electric stimulation. Piezoelectric transducers are applied for example in medical ultrasonography for imaging of internal body structures and in nondestructive testing (NDT) for examination and inspection of material properties in industry. They can be potentially very efficient optically triggered sources of coherent acoustic phonons thanks to their unique and superior properties. As ferroelectrics possess very high internal polarization in

ferroelectric domain and strong piezoelectric response, photoinduced inverse piezoelectric effect can be very important mechanism of acoustic generation by optical excitation.

In this Ph.D. manuscript, after this introduction, we will then give in chapter 2 a general introduction presenting the fundamentals of ultrafast acoustics-ultrafast phononics. We will make a brief literature survey on coherent acoustic phonons generation mechanisms. Then, we will describe why we have chosen the ferroelectrics as a new source of coherent acoustic phonons by summarizing the main properties of the selected ferroelectric material BiFeO_3 (BFO). In the third chapter, the photogeneration and photodetection of longitudinal and transverse coherent acoustic phonons in polycrystalline BFO will be presented. By selecting some micrometric grains, it is possible to tune the acoustic spectrum. In particular, spectacular photogeneration/photodetection of transverse coherent acoustic phonons will be reported.

In the chapter 4, the photoelastic coupling in optically anisotropic medium, such as BiFeO_3 , LiNbO_3 (LNO) or CaCO_3 will be discussed. In particular, the time-resolved Brillouin light scattering will be investigated in details. We will show that the two ferroelectric materials BFO and LNO exhibit the unique properties to induce a light mode conversion of the probe beam (ordinary/extraordinary) while this effect is not observed for “classical” anisotropic solid (CaCO_3). This offers a unique possibility to modulate at the picosecond time scale the polarization of light pulses.

This manuscript will be concluded with some perspectives opened by these researches.

Chapter 2: Ultrafast acoustics, ultrafast phononics

2.1 Introduction

In the following chapter we will introduce the basics of the so-called ultrafast acoustics and the well-known femtosecond pump-probe method. We will present the current description of mechanisms of generation of coherent acoustic phonons. We will then focus on the properties of piezoelectric and ferroelectric materials to explain why this class of materials is of particular interest for the ultrafast generation of strain and for potential applications in next generation of optically triggered acoustic transducers.

2.2 Principle of ultrafast acoustics, ultrafast phononics

2.2.1 Generalities about ultrafast acoustics

Ultrafast acoustics aims at generating, detecting and controlling the coherent acoustic phonons in the typical range of frequency of GHz-THz. This is possible thanks to a conversion of the optical energy into mechanical energy. When light interacts with a solid (pump beam excitation), the internal energy of this solid, within a given irradiated volume, is modified, this leads from the thermodynamic point of view to a stress (pressure change) [1]. This photo-induced stress is a source of coherent lattice vibration. In a typical experiment as shown in Fig. 2.1, the sample (here a thin film) is excited by ultrashort laser pulses (picosecond or subpicosecond) and an acoustic pulse with duration of several tens to hundreds of picoseconds is generated at the surface for example (with corresponding frequencies in GHz range). For such experiment laser light is divided into two beams, first one is the so-called pump beam, which excites sample and generate acoustic phonons, and second one called probe beam, which detects generated acoustic pulse.

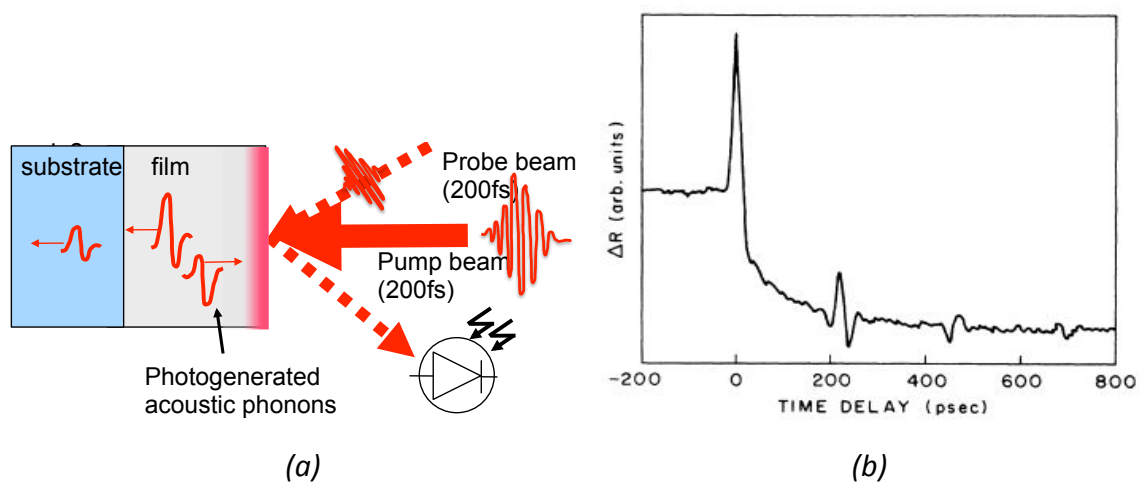


Fig. 2.1. (a) Principle of the pump-probe experiment in ultrafast acoustics (case of a thin film deposited on a substrate). The acoustic pulse is generated (pump beam) on the free surface of an absorbing material and, after reflection on the substrate, can be optically detected with the delayed probe beam. This typically gives rise to periodic acoustic echoes as shown in (b) Photoinduced changes in reflectivity of a 2200\AA film on As_2Te_3 sputtered onto a sapphire substrate [4].

The coincidence time, *i.e.* $t=0$ in Fig. 2.1(b), corresponds to the arrival time of the pump beam on the material and usually leads to a pretty large variation of the optical properties (so-called “electronic peak coincidence”). In absorbing solid, this time corresponds to the excitation time of the electronic cloud whose dynamics is crucial for the emission of coherent acoustic phonons. One important parameter that drives the generation mechanism is the depth penetration of the pump light. We will then distinguish the case of solids with important (thermoelastic, deformation potential and inverse-piezoelectric effect processes) or negligible (electrostriction process) optical absorption. This will be discussed more in the next sub-part 2.3. Optical phonons can also be generated through this interaction providing the time resolution is shorter than the optical phonon period but for the purpose of this manuscript and we will focus on acoustic phonon and invite the reader to literature reviews focusing on optical phonons for more details [2,3].

The general equation of motion (atoms displacement $u(z, t)$) can be written according to the classical Newton law (for the typical range of frequency we deal with GHz-THz) even if the quantum theory has to be taken into account for describing the photoinduced stress we will detail latter on. We have [4, 5]:

$$\frac{\partial^2 u(z,t)}{\partial t^2} - v_a^2 \frac{\partial^2 u(z,t)}{\partial z^2} = \frac{1}{\rho} \frac{\partial \sigma(z,t)}{\partial z} \quad \text{Eq. 2.1}$$

where: $u(z, t)$ – displacement of atom

v_a – speed of propagation of acoustic pulse

ρ – density of medium

$\sigma(z, t)$ – time and space dependence of the photo-induced stress

In the description of acoustic motion, we can assume the 1D approximation geometry as soon as the area over which the energy is deposited by the pump beam is much larger than the propagation distance of the coherent acoustic phonons. Moreover, it should be mentioned, that spectrum of acoustic phonons ($u(k, \omega)$), where k and ω are the acoustic wave vector and the pulsation, is completely governed by dynamics (time evolution) of stress profile and it can be obtained with proper mathematical treatment with use of Fourier and Laplace transforms [5].

The time-resolved detection of coherent acoustic phonons is realized by delaying the probe pulse with respect to the pump pulse, what allows to detect change of transient reflectivity (transmission) at selected time after excitation. It is accomplished by monitoring the optical path of probe pulse with the so-called delay line (Fig. 2.2(a)). The change of the optical path (ΔL) of probe pulse is directly converted into a time delay (Δt). Shift of delay line by 3mm corresponds for example to a time delay of probe pulse of 20 ps. In this experiment, it is important to keep in mind that ultrafast phenomena under investigation are as fast as 1ps typically (and sometimes shorter). The standard electronic devices bandwidth cannot

reach such high frequency. That is the reason why a high bandwidth optical delay line is used.

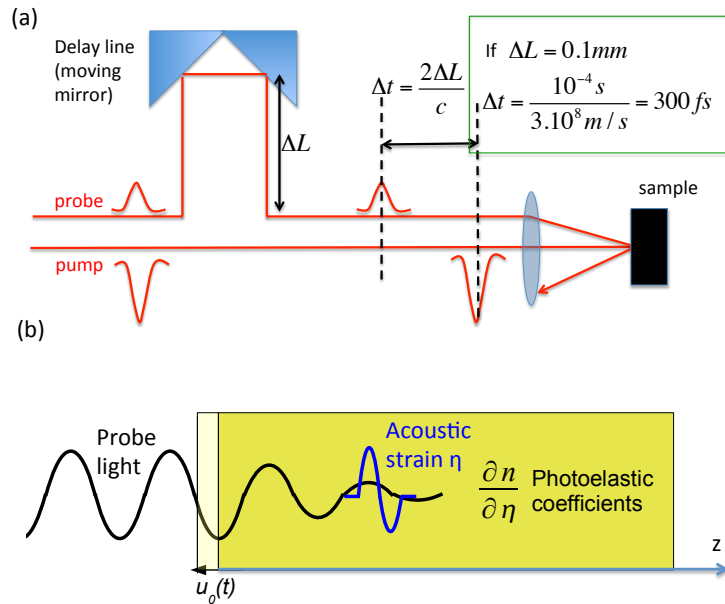


Fig. 2.2. (a) Principle of the optical delay line to realize ultrafast time-resolved pump-probe experiments. (b) Detection process: scattering of the probe light by the acoustic strain.

The coherent acoustic phonons are detected thanks to the modulation of the dielectric function induced by the acoustic strain or/and the surfaces/interfaces displacement caused by these phonons. Depending on detection scheme, reflected or transmitted probe light is collected by a photodiode whose signal provides, only indirectly, some information about the photo-induced dynamics. We say indirect in a sense that we do not have access directly to the photoinduced strain but only through the modification of the optical properties. There are the interferometric contribution due to the free surface motion $u(0)$ and the photoelastic coupling leading to probe light scattering (Fig. 2.2(b)). For example, in the case of a semi-infinite system it has been shown that the complex transient optical reflectivity δr is given by [4]:

$$\frac{\Delta r}{r} = -2ik_o u(0) + \frac{4ik_o n}{1-n^2} \frac{\partial n}{\partial \eta} \int_0^\infty \eta(z, t) e^{2ink_o z} dz \quad \text{Eq. 2.2}$$

where: k_o – probe light wave vector in vacuum

$u(0)$ – free surface displacement of the sample

η the strain

n – complex refractive index

$\frac{\partial n}{\partial \eta}$ – photoelastic coefficient

The intensity change of the optical reflectivity is then [4]: $\frac{\Delta R}{R} = 2\text{Real}\left(\frac{\Delta r}{r}\right)$

It is worth to notice that depending on the optical properties of the solid under investigation, we can somehow divide the detection process into two categories [4]. The first one is the broadband detection process which is performed with a probe beam that does penetrate only slightly the solid: in that case, the characteristic length of the penetrating probe beam is very short, *i.e.* the detection process is sensitive to a broad frequency range of acoustic spectrum. In that case, we can detect short acoustic pulse as shown in Fig. 2.1(b). On the opposite, if the probe beam penetrates over a large distance (usually hundreds nanometers to several micrometers for the visible range at least), the detection process is a narrowband process. In that case, as shown in Fig. 2.3(a), it is possible to “follow” the acoustic pulse in the transparent medium and to detect its propagation. That detection is based on local modulation of refractive index of medium by acoustic strain through the photoelastic effect and is sensitive to only one mode, called the Brillouin mode. That latter detection process can also be understood as an interference of probe light beams reflected on free surface and interfaces with the beam backscattered by the moving acoustic pulse (see Fig. 2.3(a)). Moving front of acoustic strain changes the optical path of probe light travelling inside the medium. This leads to continuous change of phase of scattered probe light. This change of phase leads to optical interferences, which are either destructive or constructive for a given position of acoustic pulse. Finally it gives a periodic modulation of the detected intensity which manifests itself by oscillations on the transient reflectivity signal (ΔR). Change of phase occurs at rate proportional to speed of acoustic propagation so frequency of detected Brillouin oscillations is also proportional to speed of acoustic pulse.

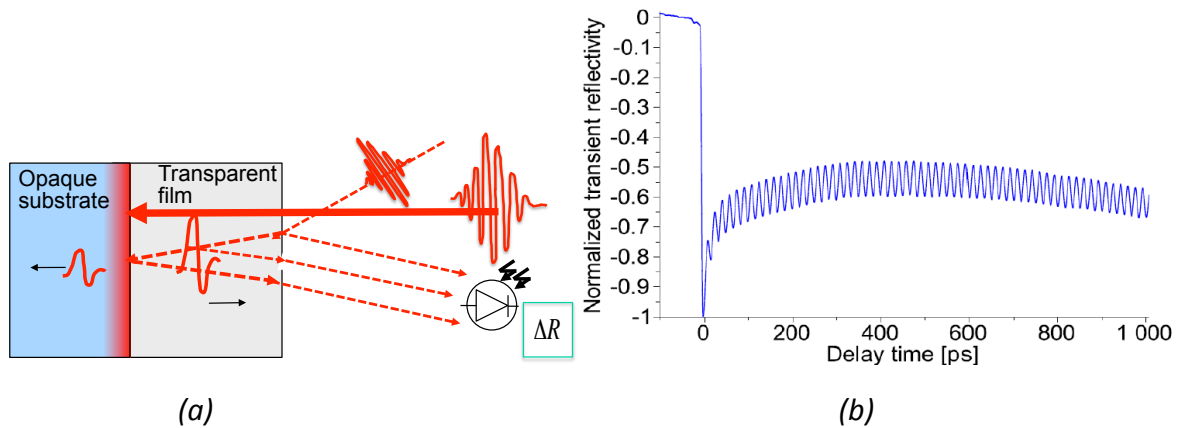


Fig. 2.3: (a) Example of the detection of coherent acoustic phonon in a transparent solid. The acoustic phonons are first generated in the opaque substrate and then are detected by the Brillouin process (interference effect of the three dashed beams). (b) Example of a transient optical reflectivity signal obtained in LiNbO_3 revealing the clear Brillouin oscillations.

This detection process is usually called picosecond interferometry. The Brillouin frequency is given by [4]:

$$f_B = 2v_a \sqrt{n^2 - \sin^2(\theta)} / \lambda \quad \text{Eq. 2.3}$$

where n , θ and λ are the refractive index of the solid, the incidence angle of the probe beam relative to the normal of the surface and the probe wavelength in vacuum.

Most of the signals we will deal with in this research will be obtained through that second process. A more detailed discussion of this Brillouin process will be given in Chapter 4. An example of these Brillouin oscillations is shown for the case of LiNbO₃ (Fig. 2.3(b)). In that case the acoustic phonons are generated at the surface with a chromium film (20 nm) and the emitted coherent longitudinal acoustic phonons are detected with a probe beam deeply penetrating in the wafer (590 nm).

2.3. Generation mechanisms of high frequency phonons by pulsed lasers

The photoinduced stress that we briefly introduced in the previous sub-section ($\sigma(z,t)$) has different physical origins that are thermoelasticity (TE), deformation potential (DP), inverse piezoelectricity (PE) and electrostriction (ES). In this part we will briefly detail the underlying physics associated to each of the process. We cannot intend to make a general review and invite the reader to the dedicated review papers [4,5, 6].

2.3.1. Thermoelasticity (TE)

The most familiar mechanism of generation of GHz-THz coherent acoustic phonons is the thermoelasticity. This mechanism generally prevails in metals. For this mechanism optical energy deposited by laser pulse is converted into thermal energy (lattice energy) through different channels of hot electrons relaxation. This leads to sudden increase of lattice temperature and ultrafast expansion of the irradiated metal for example. In consequence there is an emission of acoustic pulse from expanded region. As ultrafast heating happens in picosecond time scale under irradiation by femtosecond pulse (typical electron-phonon coupling time), this leads to emission of phonons with frequencies of tens to hundreds of GHz. In that case, the generation of stress can be described analytically considering the temperature rise follows the depth penetration profile of the pump light (neglected diffusion of electrons, Fig. 2.4(a)). Ultrashort light pulse of energy Q irradiating area A of the metal surface with absorption length ζ leads to profile of temperature rise given by formula [4]:

$$\Delta T(z) = \frac{(1-R)Q}{CA\zeta} e^{-\frac{z}{\zeta}} \quad \text{Eq. 2.4}$$

where: R – reflectivity of metal

Q – energy of pulse light

C – specific heat per unit volume

A – irradiated area

ζ – absorption length of light (skin depth for given wavelength of light)

z – distance from the surface into volume of metal

In Eq. 2.4, the temperature profile is simply obtained by the ratio of the deposited energy density by the pump pulse and the volumic heat capacity. In the case of isotropic thermal expansion, this sudden temperature rise leads to the stress profile $\sigma(z)$ given by:

$$\sigma(z, t) = -3B\beta\Delta T(z, t) \quad \text{Eq. 2.5}$$

Where: B – bulk modulus
 β – linear expansion coefficient

This stress launches longitudinal acoustic waves into the medium. From each point strain waves are launched in the positive and negative directions. The backward going pulse is reflected at the free surface of the film with a sign change (Fig. 2.4(c)). After a long time compared to the time ζ/v_a (where v_a is a sound velocity) required for sound to propagate through a distance equal to absorption length (therefore after the sound pulse has left the region of excitation), the form of the strain pulse inside the film is given by [4]:

$$\eta(z, t) = -\frac{3(1-R)QB\beta}{2CA\zeta} e^{-\frac{z-v_a t}{\zeta}} \text{sgn}(z - v_a t) \quad \text{Eq. 2.6}$$

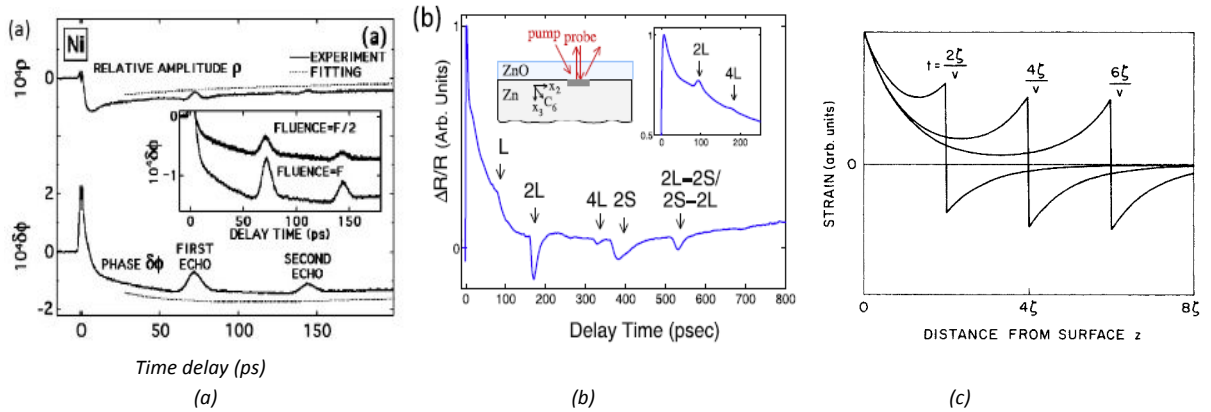


Fig. 2.4. (a) Results showing acoustic echo detected in strong electron-phonon coupling nickel (Ni) [7]. (b) Thermoelastic generation of longitudinal (LA) and transverse (TA) coherent acoustic phonons in disoriented Zn single crystal [8]. (c) Space and time dependence of the photoinduced strain profile according to Eq. 2.6.

Anisotropic thermoelastic stress can also be used to generate transverse acoustic waves as shown in Fig. 2.4(b) [8, 9, 10, 11]. This is realized thanks to a proper low-symmetry orientation of the metal, which is a requirement for breaking the symmetry. In this way GHz shear acoustic phonons (normally with frequency up to 50GHz) were quite efficiently generated [8-11].

This thermoelastic model (Eq. 2.4) works well for large electron-phonon coupling metals where hot electrons are nearly confined to the skin depth (Fig. 2.4(a)). When hot carrier

super-diffusive effect occurs, the photoinduced strain field is broadened because the electron thermalization, which leads to the lattice heating, takes place out of the initial light pump absorption [12, 13, 14]. The hot electrons diffusion has been evidenced (Figs. 2.5(a),(b) and (c)) and leads to the emission of coherent acoustic phonons over a large distance that usually is 10 times larger than the skin depth in noble metals (Au, Cu) [12-14].

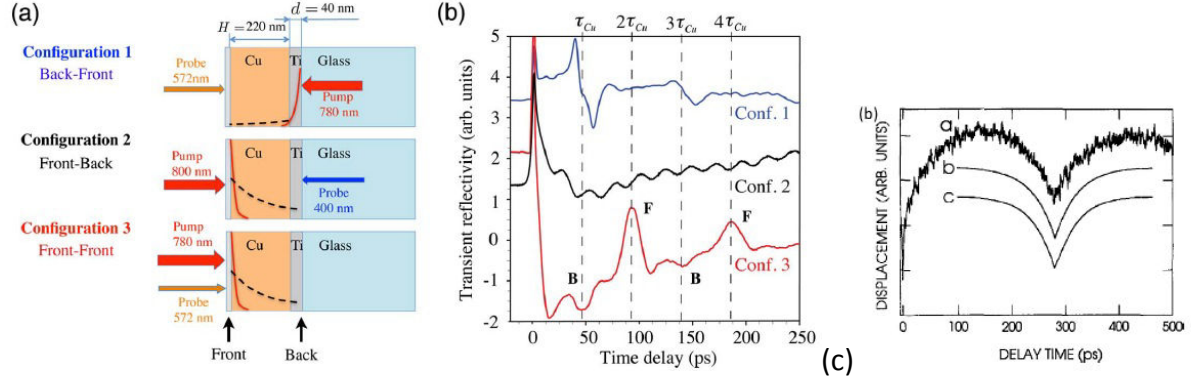


Fig. 2.5. (a-b) Description of the three different front–back and front–front experimental configurations. The optical excitation is depicted as red lines and indicate the evanescent light penetration in the metals (copper or titanium). The dashed lines depict the energy distribution of the excited hot electrons, consecutively to their superdiffusive transport. (b) Time-resolved optical reflectivity measurements according to the three configurations (1, 2, and 3). The time constant $\tau_{Cu} = H/V_{Cu}$ corresponds to the time of flight of the acoustic wave packet through the copper layer of thickness H at the acoustic speed V_{Cu} . B, and F refers to coherent acoustic phonons emitted from the back and the front, respectively [13]. (c) Broadening of the acoustic pulse in gold up to 100ps due to the hot electrons diffusion [14].

The study of acoustic generation during electronic relaxation can give information about dynamics of diffusion of electrons and about strength of their interaction with lattice (electron-phonon coupling constant). It was stated that acoustic strain profile provides “snapshot” of the initial spatial temperature distribution of the lattice, therefore it can be treated as a sensitive probe of non-equilibrium dynamics of the electronic diffusion [12-14]. As problem is described by non-equilibrium diffusion equation which is nonlinear, to find analytical solutions with good approximation it was used linearized formulation. It gives generalized solution for induced strain from thermal expansion of lattice taking into account ultrafast diffusion of electrons [14]:

$$\eta(z, t) \propto e^{-\sqrt{g/\kappa_e}(z-v_a t)} \text{sgn}(z - v_a t) \quad \text{Eq. 2.7}$$

where: g – electron-phonon coupling constant

κ_e – electronic thermal conductivity

Parameter $L = \sqrt{\kappa_e/g}$ is the distance over which excited electrons transfer their energy into the lattice. It is intuitive that the weaker the interaction of electrons with phonons, the

higher is the electronic thermal conductivity; consequently further thermal energy of electrons is transported and deposited. A typical profile of heat deposition in copper is shown by dashed line in Fig. 2.5(a).

2.3.2. Deformation potential (DP)

Deformation potential mechanism relates the modification in energy of electronic distribution to the induced strain in solids. Modification of electronic distribution (for example by optical excitation) leads at microscopic level to change of interaction between electrons-cations and cations-cations and electrons-electrons. This in turn causes a change of the interatomic forces since they are dependent on the electronic distribution. Modification of interatomic forces leads to change of equilibrium position of cations in lattice and hence to crystal deformation [4-6]. Consequently, as soon as the carriers are out-of equilibrium, this process induces a lattice deformation and consequently coherent acoustics phonons are emitted. The general description is given by equation [6]:

$$\frac{\delta V}{V} = \frac{\delta U}{d_{eh}} \quad \text{Eq. 2.8}$$

where: $\frac{\delta V}{V}$ – strain caused by acoustic phonons (V is volume of crystal)

δU – modification of electronic energy

d_{eh} - deformation potential parameter

This equation shows direct connection between variation of electronic energy and the lattice strain. Modification of one side of equation leads to modification of other. By considering band structure of materials, it can be viewed in opposite way (Fig. 2.6(a)). When strain appears in the crystal, it modifies overlapping of the atomic orbitals (by changing of atomic distance or angle between bonds), what leads in consequence to a shift of electronic levels (δU). Even single electron travelling through crystal lattice modifies locally potential and force neighbor atoms to move (i.e. creation/annihilation of phonons). Deformation potential mechanism can be also understood better by considering the molecular picture (Fig. 2.6(b)). Excitation of carriers promotes them to empty electronic levels, what means creation, or destruction of interatomic bonds what leads to increase or decrease of the equilibrium interatomic distances, depending on the nature of bonds (bonding, or anti-bonding) [6].

By taking into account existence of bands in the electronic structure of the solid, the light induced modification of electrons population at different levels (E_k) describes more correctly the photoinduced stress in this case [4]:

$$\sigma_{DP} = - \sum_k \delta n_e(k) E_k \gamma_k = \sum_k \delta n_e(k) \frac{\partial E_k}{\partial \eta} \quad \text{Eq. 2.9}$$

where: k – wavenumber of electron

$\delta n_e(k)$ – change in electronic concentration at level k
 E_k – energy of electron at level k
 γ_k – Grüneisen coefficient for level k
 $\frac{\partial E_k}{\partial \eta}$ – change of electronic energy at level k with induced strain

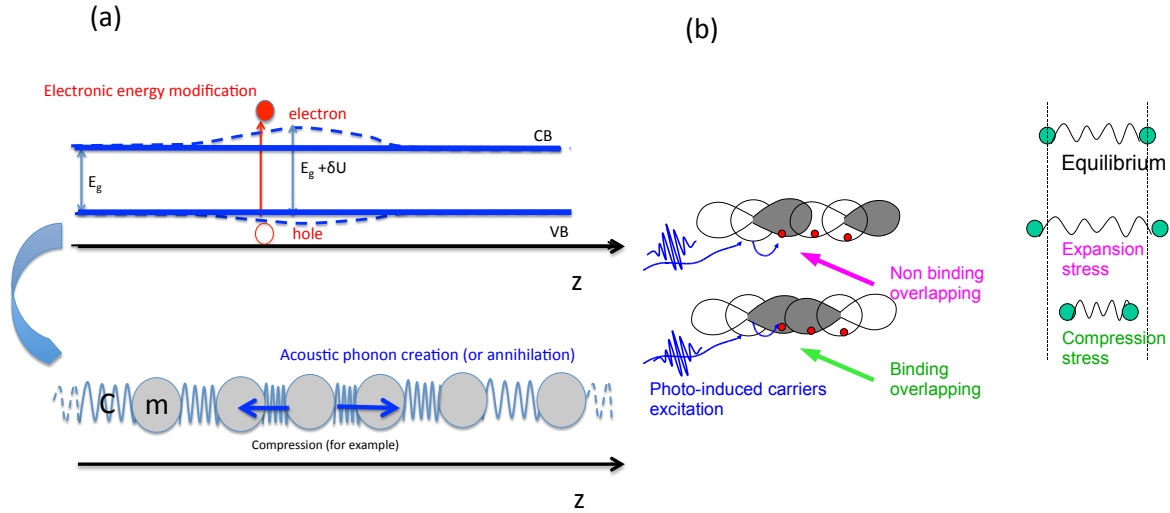


Fig. 2.6. a) Deformation potential in band structure picture: excitation of electron hole pair disturbs electronic distribution and modifies interatomic interaction leading to change of atomic positions and manifestation of strain, b) Deformation potential in molecular picture: excitation of electron from one orbital to another leads to modification of electronic distribution and appearance of bonding or antibonding interactions between atoms, what force them to compression or expansion (Figure adapted from [6])

Because of ultrafast thermalization of electron gas with lattice in metals, electronic deformation potential can be only relevant (enough efficient to launch strain) in the first ps from excitation time. After electron-phonon thermalization, only thermoelasticity plays an important role in generation of strain [4-6]. There are experimental results showing relevance of photoinduced deformation potential in metals. To explain expansion and vibrations of metallic nanoparticles correctly, DP stress has to be taken into account [15]. It means that DP plays important role just after excitation in the confined systems for which hot electrons cannot escape from excited region, so that electronic pressure remains significant.

For semiconductors, in the case of very fast intraband relaxation processes (relaxation of hot electrons towards the bottom of the conduction bands and relaxation of the holes towards the top of the valence bands), the deformation potential stress can be simplified by Eq. 2.10. This model is correct to explain the emitted acoustic spectrum for acoustic phonons

frequencies that are typically smaller than the inverse of the time of the intraband relaxation process. Otherwise, the detailed expression (Eq. 2.9) has to be taken into account.

$$\sigma_{DP} = \sum_k \delta n_e(k) \frac{\partial E_k}{\partial \eta} = N \frac{\partial E_g}{\partial \eta} = -NB \frac{\partial E_g}{\partial P} = -d_{eh}N \quad \text{Eq. 2.10}$$

where: B – bulk modulus

N – concentration of photoexcited electrons

E_g – energy of band gap of semiconductor

DP stress in semiconductors can be either compressive or tensile, depending on the nature of electronic levels where carries are excited [4-6]. Both possibilities are determined by the sign of corresponding deformation potential parameter, which can be obtained from pressure dependence of the band gap. When the value of bandgap increases with pressure $\frac{\partial E_g}{\partial P} > 0$, then DP parameter is positive what means expansion of crystal under excitation of electrons through the band gap. In opposite situation this leads to contraction of lattice. It is strictly connected to the fact that orbitals in the crystal can be bonding, non-bonding, or anti-bonding. Therefore under ultrafast excitation of electrons over the band gap, DP mechanism can lead to expansion or contraction of lattice. For silicon (Si) deformation potential is negative what means contraction of lattice under optical excitation with sufficient energy of photons to promote electrons to conduction band. Contraction of silicon surface was experimentally observed by illumination by femtosecond pulse and detection of transient surface displacement [16].

2.3.3. Inverse piezoelectricity (PE)

Piezoelectric materials belong to non-centrosymmetric crystal classes. It means that they do not have center of symmetry, what results in lack of inversion symmetry (broken symmetry). This have very important consequences for piezoelectric material. Because of non-centrosymmetric structural property of piezoelectrics, there are possible coupling of different degrees of freedom, like electric field and strain, stress and polarization and electric field and stress. It means for example that applied stress can induce polarization and this is referred as piezoelectric effect (PE), or applied electric field can induce stress (and simultaneously strain) what leads to deformation of piezoelectric crystal, what is called inverse piezoelectric effect. The stress associated to an electric field (E) in the piezoelectric material is [17]:

$$\sigma_j = e_{ij}E_i \quad \text{Eq. 2.11}$$

where e_{ij} is the inverse piezoelectric constant ($i=1,2,3\dots6$). We will come back to the piezoelectric effect in the next part (2.4). To generate acoustic phonons by optical excitation through PE mechanism, modulation of internal electric field is necessary. Light can first

create mobile photoexcited carriers which can modulate the internal electric field, which through the inverse piezoelectric effect (Eq. 2.11), induces some lattice strain (Fig. 2.7). The pre-existing electric field can have different origins : external application of electric field, build-in field in junction or close to the surface of semiconductor, electric field generated by dynamic separation of electrons and holes (so called Dember field [18]), or finally internal polarization within the ferroelectric domains. A sketch of this mechanism is given in Fig. 2.7.

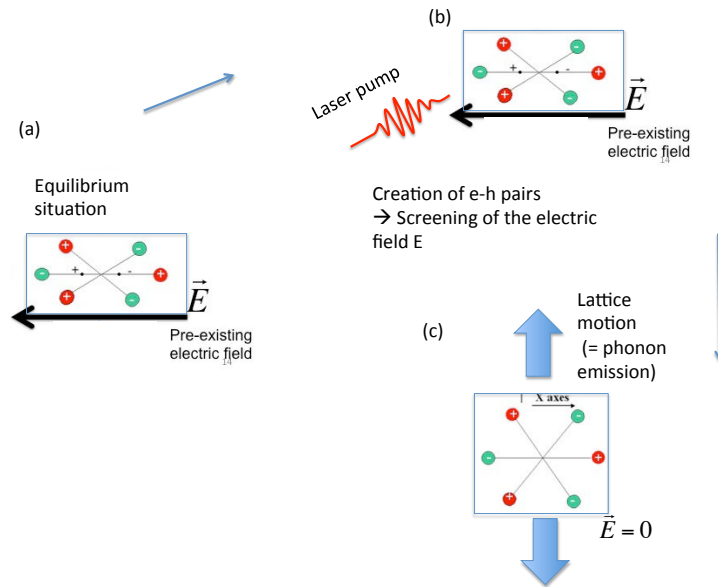


Fig. 2.7. Picture illustrating the photoinduced inverse piezoelectric effect.

Several studies of ultrafast acoustic generation by subpicosecond laser pulses have reported the generation of phonons by PE mechanism. Convincing report about this phenomenon was obtained in gallium nitride (GaN) p-n junction [19]. Studied junction was localized about $1\mu\text{m}$ beneath the surface of structure, so pump light had to propagate through the semiconductor to excite free charges in the region of junction where there is localized electric field. Band gap of this material is about 3.4eV and it was excited by near UV radiation for which penetration depth was about 700nm . This allowed the excitation of carriers within the junction. A clear emission of coherent acoustic phonons coming from the embedded junction was identified [19]. On the contrary, when pump light did not reach the junction, the disappearance of the acoustic pulse was reported.

Another observation of acoustic generation by PE effect was obtained on highly p-doped GaAs with crystallographic orientation [111] (Fig. 2.8(a)). The coherent acoustic phonons were probed with the picosecond interferometry detection process (Brillouin oscillations) [20, 21]. There were two main signatures of piezoelectric effect. One is the change of the Brillouin signals phases for excitation on two opposite faces (A and B). This effect is directly connected to the opposite sign of piezoelectric constants between both sides. Another observation confirming this effect was saturation of generated acoustic amplitudes. Interpretation of this process was that, carriers excited in strong local electric field (built-in electric field oriented perpendicular to the surface in this case) were accelerated and

screened this field leading to generation of stress and emission of acoustic phonons by inverse PE mechanism [20].

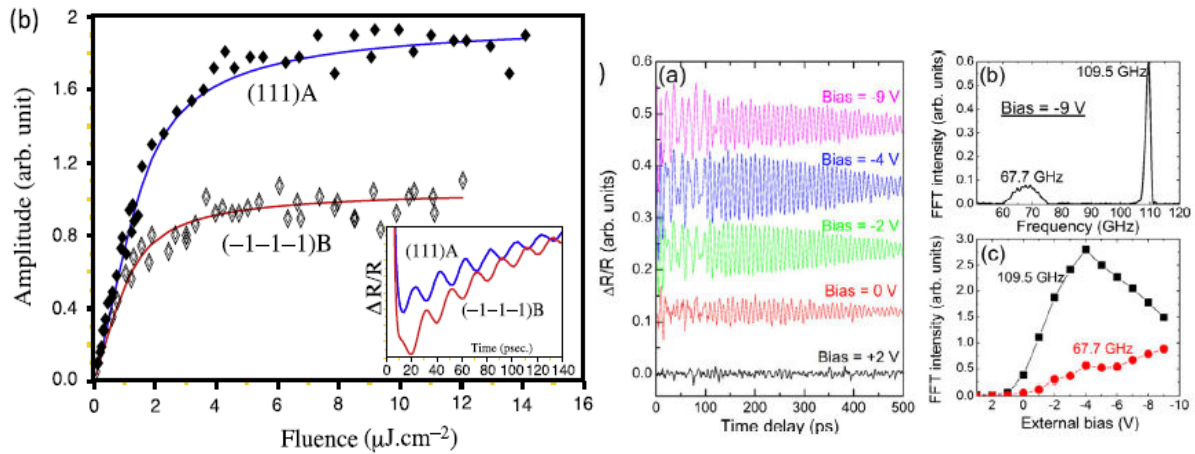


Fig. 2.8. (a) Fluence dependence of amplitude of acoustic phonons generated on two faces (A and B) of p-doped piezoelectric [111] GaAs wafer by inverse PE mechanism. It can be noticed saturation of generated strain. In the inset there are shown Brillouin oscillations, which are out-of-phase in result of generation of strain with opposite sign by inverse PE effect on two faces (A-B) of sample. This feature confirms origin of acoustic phonons as cannot be explained by other mechanisms of ultrafast acoustic generation [20].(b) Dependence of LA mode photo-generation by inverse PE effect as a function of external bias [23]. These results clearly show that generation process can be enhanced by application of external electric field with selected amplitude.

Acoustic generation by inverse PE effect was also observed in InGaN/GaN superlattice [22]. There are also interesting results showing that generation of coherent acoustic phonons by the inverse PE mechanism can be tuned by applied external electric field (Fig. 2.8(b)). It was revealed that external bias can enhance amplitude of acoustic phonons generated by PE effect in InGaN/GaN multiple quantum wells [23] (Fig. 2.8(b)).

2.3.4. Electrostriction (ES).

Generation of ultrafast stress can also take place even without absorption of light, so for transparent medium. As intensity of light is proportional to square of electric field so for light with high intensity, an associated electric fields can be significant. This is the case for pulsed lasers (femtosecond). Consequently, it is possible to polarize matter and force ions to move. This is principle of generation of strain and phonons by pulsed laser light in transparent matter (without creation of electron-hole pairs), which is called electrostriction. Polarization of medium by electric field of light can be treated as centrosymmetry breaking induced by light electric field, which in consequence leads to second order piezoelectric effect (electric field of light can induce in such case contraction or expansion of matter) [6]. Because of that electrostriction can be treated as second order process in respect to electric field, whereas

piezoelectric effect as first order. Stress induced by electrostriction mechanism described by simplified scalar formula has form [5, 6]:

$$\sigma_{ES} = -\frac{1}{2}\rho \frac{\partial \varepsilon}{\partial \rho} E^2 \quad \text{Eq. 2.12}$$

where: $\rho \frac{\partial \varepsilon}{\partial \rho}$ – electrostrictive parameter

It is worth to notice that electrostriction mechanism can lead to generation both longitudinal and transverse stress (LA and TA phonons can be emitted) since the light-induced lattice polarization can be achieved with an electric field perpendicular to the propagation direction of the pump beam (*i.e.* transverse displacement).

Generation of acoustic phonons by ES mechanism was experimentally demonstrated by application of the transient optical-grating method [24]. It is based on irradiation of surface of studied medium by two crossed laser beams with selected angle of incidence. Interference between these two beams leads to intensity pattern (so also in some sense electric field pattern) and periodicity of this pattern can be modified by changing angle between incident laser beams. Wavelength (so also frequency) of emitted acoustic wave generated by ES mechanism is determined by periodicity of gratings. Therefore it gives finally possibility of manipulating of generated acoustic wave by relative orientation of two incident laser beams.

2.4. Why ferroelectrics/multiferroics for ultrafast acoustics?

2.4.1. Introduction

There exists a broad range of materials in which light-matter interactions lead to various light-induced strain with, sometimes, efficient conversion of light energy into mechanical energy as briefly introduced previously. The light induced strain (sometimes called photostriction) is observed in very different materials such as metals, semiconductors, correlated oxides [25, 26], as well as in organic-based materials [27, 28]. Among mechanisms, which we introduced in the previous sub-part, it has been already shown that ultrafast optical generation of coherent acoustic phonons by inverse piezoelectric effect can be efficient in piezoelectric semiconductors. It was demonstrated that such mechanism of acoustic generation by inverse piezoelectric effect can be as efficient as deformation potential, or even more efficient at low excitation fluences before saturation of the internal electric field [9, 18-21]. Such mechanism is expected to be very promising in ferroelectrics [25]. The reason of that is the existence of a strong internal electric polarization and high values of piezoelectric coefficients. This should lead to a strong response of such materials when the internal electric field is modified by the application of an external field, or when photoexcited carriers are photoinjected in the polarized ferroelectric domains. Because of a large electro-mechanical coupling, ferroelectrics are already widely used as transducers of ultrasonic waves but mainly in the kHz-MHz range [29]. These materials convert very efficiently electric energy into acoustic one, therefore they are very good sources of acoustic

waves. We would like to extend their application to the field of light-controlled piezotransducers (GHz-THz).

Beyond the electromechanical coupling, the properties of ferroelectrics are also very rich. Ferroelectrics have a reversible spontaneous electric polarization whose magnitude and direction can be tuned by varying temperature, pressure, electric field, strain or chemical composition [29]. It is worth to mention that quite recently, a special attention has been drawn towards a new class of ferroelectrics called photosensitive ones (photoferroelectrics). Such materials exhibit very interesting interactions and coupling with light [30, 31]. Among the applications, very promising are ferroelectric photovoltaic materials. In particular, it was recently shown some very large above bandgap open-circuit voltage, related with polarization based charge separation mechanism. The charge separation appears to be fundamentally different compared with that of classical semiconductor solar cells. The photovoltage can be significantly increased thanks to the existence of the internal electrical fields. As we will show and discuss in this manuscript, several investigations performed in the field of photoferroelectrics are very useful to help us to analyze and understand the photoinduced strain in ferroelectrics since the fundamental properties of photoexcited carriers are crucial for both goals.

2.4.2. Basics of piezoelectricity and ferroelectricity

Piezoelectric materials have the ability to change the internal electrical polarization in response to an applied mechanical stress or to be mechanically strained in response to an applied electric field. The crystallographic requirement for a solid to exhibit piezoelectricity is to exhibit non-centrosymmetry. This is the case of semiconductors like GaAs or insulator SiO₂ (quartz) [7].

The inverse piezoelectric effect describes the strain generated in a piezoelectric material in response to an applied electric field. This effect is written as:

$$\eta_j = p_{ij}E_i \quad \text{Eq. 2.13}$$

where η_i is the electric field induced strain, E_j is the applied electric field and p_{ij} is the piezoelectric coefficient. The piezoelectric coefficient is a third rank tensor, although is written in Equation (2.13) in reduced matrix notation by representing the mechanical strain as a 1-dimensional matrix with Voigt notation $i = 1, 2, \dots, 6$.

The direct piezoelectric effect describes a change in polarization due to an applied stress and is written as:

$$P_i = d_{ij}\sigma_j \quad \text{Eq. 2.14}$$

where P_i is the dielectric displacement and σ_j is the applied stress.

When an electric field is applied parallel to the z-direction and strain is also measured in the z-direction, the piezoelectric coefficient of relevance is then the longitudinal piezoelectric coefficient p_{33} :

$$\eta_3 = p_{33}E_3 \quad \text{Eq. 2.15}$$

The longitudinal piezoelectric coefficient described by the inverse piezoelectric effect (Eq. 2.15) is equivalent to the longitudinal piezoelectric coefficient described by the direct piezoelectric effect:

$$P_3 = d_{33}\sigma_3 \quad \text{Eq. 2.16}$$

Solid	Quartz	BaTiO ₃	PbTiO ₃	PZT	LiNbO ₃	BiFeO ₃	GaAs (d41)
p_{33} (pm/V)	2.3	190	120	140	6	2-4	2.6^{32}

Table 2.1: Some piezoelectric constants.

It is also possible to link directly the internal electric field to the piezoelectric stress as shown in Eq. 2.11.

In ferroelectric materials, a spontaneous polarization exists due to the separation of negative and positive charge centers in the crystallographic unit cell. This effect usually leads to a natural breaking of symmetry and the disappearance of the center of symmetry making them piezoelectric materials (see Fig. 2.9). These ferroelectric materials usually exhibit enhanced piezoelectric properties compared to semiconductors (see Table 2.1 above). The physics of ferroelectric material is very rich and we do not intend to give an extensive description but only the most important properties [1, 33]. The canonical structure which exhibits a spontaneous polarization (ferroelectricity) is the perovskite structure, ABO₃ like PbTiO₃ or BaTiO₃ for example. The ferroelectricity appears below a given temperature (Curie temperature) where a lowering of the symmetry (rhombohedral, monoclinic, tetragonal) compared usually to the high temperature cubic phase, makes the centro-symmetry disappearing. It is to be noticed that some complex ferroelectrics, like relaxor-ferroelectric (PMN) do not exhibit clear macroscopic loss of centro-symmetry [34].

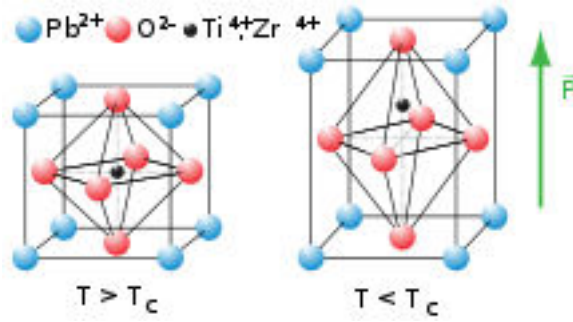


Figure 2.9: Temperature dependence of the structure of the ferroelectric PZT material.

In ABO_3 structure (where in the case of the Fig. 2.9, $A=Pb$ and $B=Ti$), the center atom (B) and the oxygen octahedron displace non-uniformly relative to the corner atom (A), resulting in a non-centrosymmetric structure. When cooling a material through the Curie temperature, different regions of the material take different crystallographic orientations of the lower symmetry crystal structure. These different regions are called ferroelectric domains and the regions that separate different domains are referred as domain walls. Ferroelectricity is characterized by the ability of a material to change its direction of spontaneous polarization in response to application of an electric field. The electric field required for this reorientation to occur is known as the coercive field (E_c) and typically involves the motion of ferroelectric domain walls (Fig. 2.10).

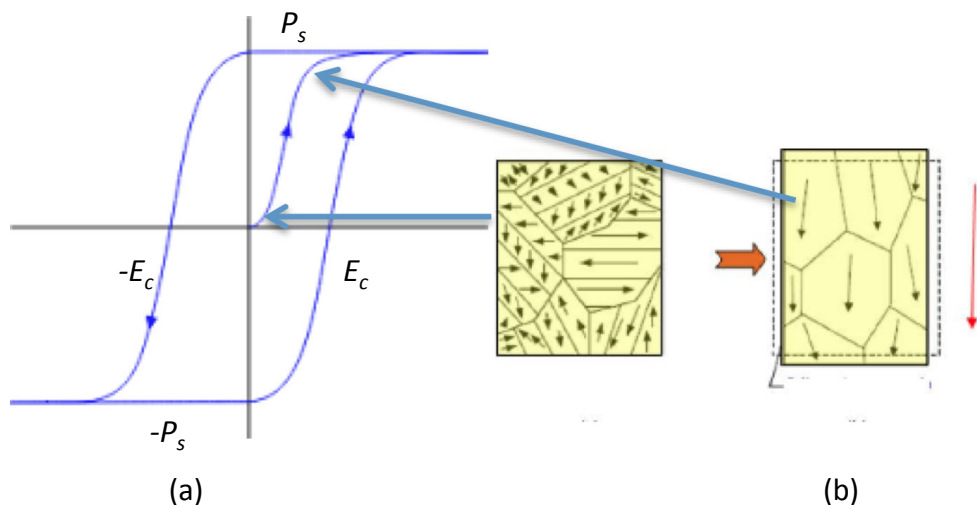


Figure 2.10: (a) Ferroelectric loop that shows the saturation polarization and the coercive field. (b) Poling of a material under external electric field.

The macroscopically observed coercive field (E_c) is the electric field required to obtain zero macroscopic polarization due to compensating positive and negative local polarization states. Polycrystalline samples usually do not exhibit neither macroscopic spontaneous polarization nor piezoelectricity. This is because the structure is composed of an equal number of all possible domain orientations (see Fig. 2.10(b)) whose local polarization cancel each other. To exhibit piezoelectricity at the macroscopic length scale it must be polarized according to a poling process that can be achieved by applying an electric field in order to align the domains (polarization saturation P_s).

2.4.3. Structure and general properties of bismuth ferrite (BFO)

BFO has received a great deal of attention during the last 15 years and it is impossible to make a summary within a few pages. While review presenting BFO as bulk [35] or thin films materials [36] can provide more extensive information, we will limit ourselves here to most relevant properties connected to the research subject of this manuscript.

Structure:

Bismuth ferrite belongs to the ferroelectrics family and even to the largest family of multiferroic materials. The room-temperature and ambient pressure phase of BFO is rhombohedral (point group $R3c$). The perovskite-type unit cell has a lattice parameter, a_{rh} of 3.965\AA and a rhombohedral angle, α_{rh} of $89.3\text{--}89.48^\circ$ at room temperature, with ferroelectric polarization along $[111]$ pseudocubic. The unit cell can also be described in a hexagonal frame of reference, with the hexagonal c -axis parallel to the diagonals of the perovskite cube ($[001]$ hexagonal direction parallel to $[111]$ pseudocubic direction). The hexagonal lattice parameters are $a_{hex} = 5.58\text{\AA}$ and $c_{hex} = 13.90\text{\AA}$ (Fig. 2.11).

The rhombohedral structure allows antiphase FeO_6 octahedral tilting around the $[111]$ direction and ionic displacements from the centrosymmetric positions along $[111]$ pseudocubic directions (see Fig. 2.11). The FeO_6 octahedra tilting angle is about 11° . At room temperature and ambient pressure, BFO is ferroelectric ($T_c = 1100\text{K}$) and also exhibits a magnetic ordering ($T_N \approx 640\text{K}$). It has an antiferromagnetic order with the spin in the (111) plane having a spatially modulation to form a cycloid with a period of about 62 nm . BFO exhibits a pretty complex phase diagram versus temperature and pressure (Fig. 2.12) that we will not specifically comment here. We can underline that even there is a magnetic transition ($T_{N\acute{e}el}$), there is no change of the crystallographic symmetry.

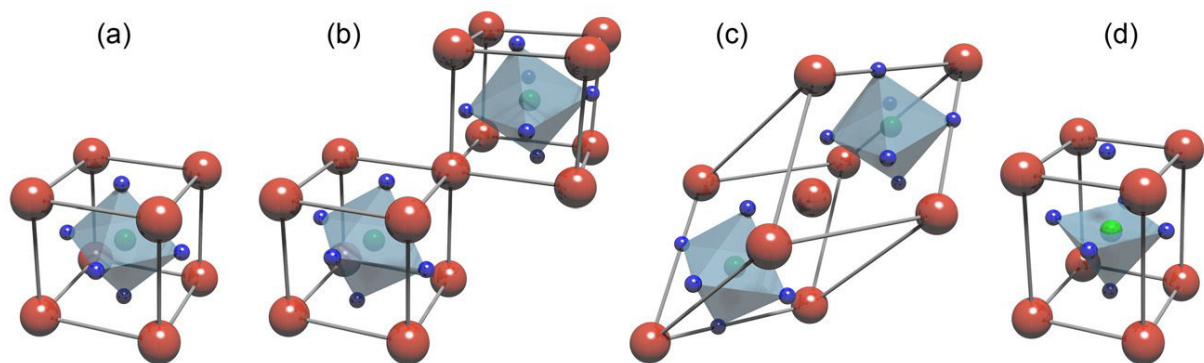


Figure 2.11. Structures of BiFeO_3 (large red spheres are bismuth, medium green spheres are iron, small blue spheres are oxygen) (a) Perfect cubic perovskite unit cell. (b) Two pseudocubic cells with cation shifts ($[111]$ direction) and with octahedra rotations around $[111]$ that finally makes the structure shown in (c) which is the rhombohedral cell. (d) The highly distorted tetragonal-like phase of BFO. Figure adapted from [36]

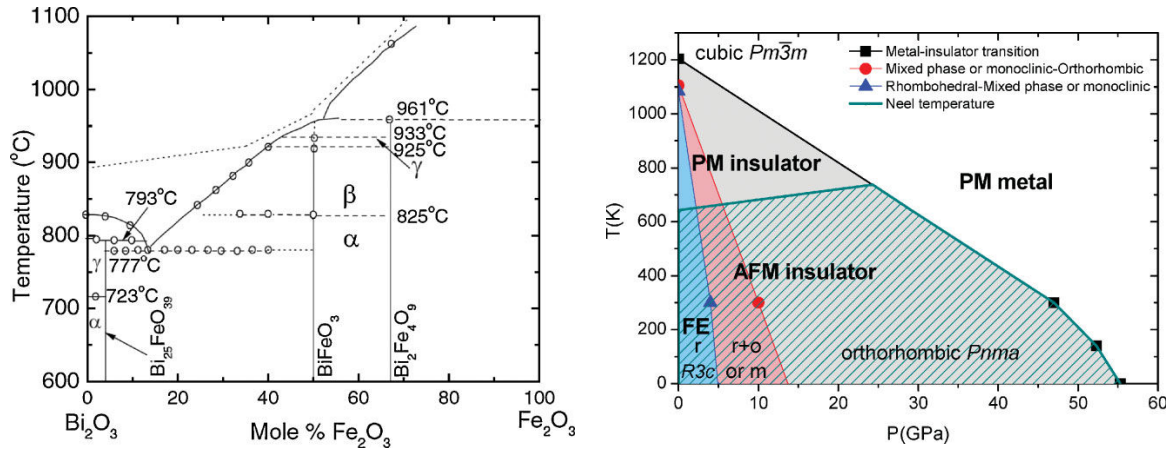


Fig 2.12: Phase diagram of BFO versus composition, temperature and pressure [35,37].

Transport properties

The temperature dependent resistivity of BFO is shown in Fig. 2.13(a) [37,38]. There is no change in the absolute value of resistivity but the Arrhenius plot shows a change in slope, with the activation energy of the charge carriers decreasing from 1.3 to 0.6 eV when the material is heated above T_N . This indicates that magnetic ordering affects the conductivity band gap or the carriers mobility activation energy, in the antiferromagnetic phase. At even higher temperatures there are further resistive anomalies correlated with the α - β (rhombohedral–orthorhombic) transition (T_{Curie}), the β - γ (orthorhombic–cubic) transition and finally, the decomposition temperature. Specifically, the resistivity decreases (but remains semiconducting) at the α - β transition and the slope of the resistivity as a function of temperature changes sign at the β - γ transition, which is consistent with a metal–insulator (MI) transition and the nearly closing of the band gap we can see in Fig. 2.13(b) [37].

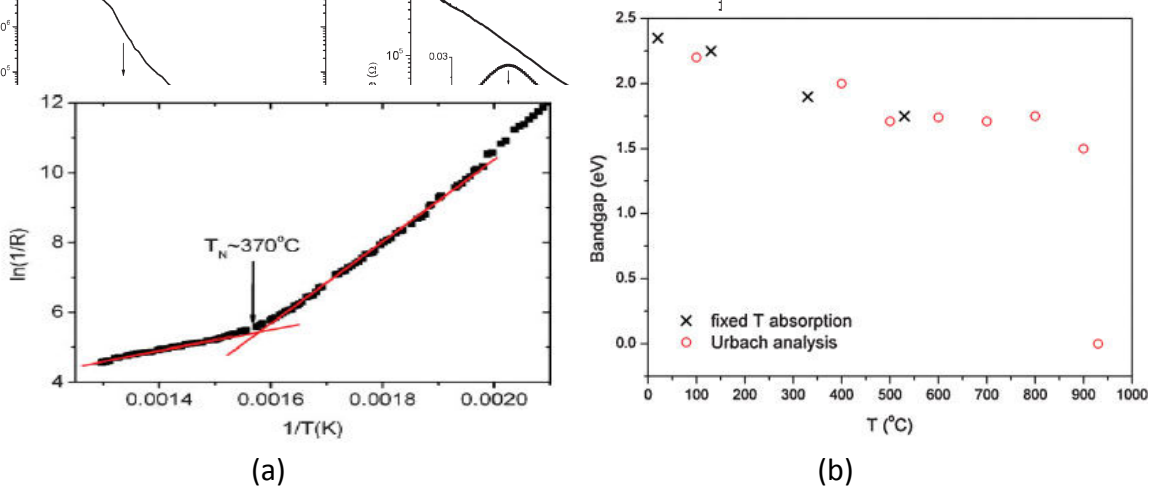


Figure 2.13: (a) Arrhenius plot of the two-probe resistivity of BFO single crystal showing a change of slope at the Neel temperature [37, 38]. (b) Temperature dependence of the band gap [37].

Optical properties

We can straightforwardly say that one of the two reasons that made us choosing BFO is its small band gap of around 2.6-2.8eV which is suitable for laser photoexcitation [39,40,41]. The refractive indices versus photon energy at room temperature are given in Fig. 2.14(a). The linear birefringence is particularly large ($\Delta n \approx 0.25$) and change slightly with temperature (Fig. 2.14(b)) [42].

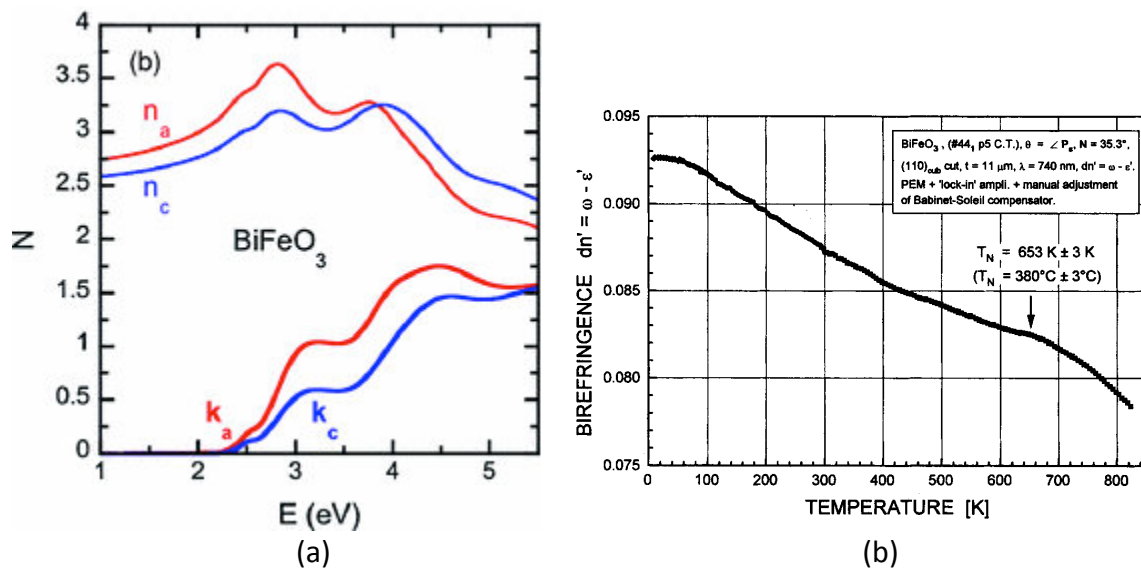


Figure 2.14: (a) Complex refractive index of a BFO thin film [42]. Letters “a” and “c” refers to ordinary and extraordinary components. (b) Temperature change of the birefringence ($n_a - n_c$) [42].

Ferroelectric and piezoelectric properties of BFO

The second reason why we have chosen BFO is its large internal polarization P . It was shown that in bulk BFO the polarization can reach up to $\sim 100 \mu\text{C}\cdot\text{m}^{-2}$ in the $[1\ 1\ 1]$ direction ($\sim 60 \mu\text{C}\cdot\text{m}^{-2}$ along $[0\ 0\ 1]$). As already pointed out, the BFO material remains ferroelectric up to $T_c = 1100\text{K}$. The polarization can point along one of eight directions (Fig. 2.15(a)), giving rise to eight possible domain variants. Accordingly, there are three possible types of boundaries separating the domain regions: 71° , 109° and 180° domain walls (Fig. 2.15(a)). The various domain types can be imaged using Piezo Force Microscopy (PFM), and through a combination of in-plane (IP) and out-of-plane (OP) responses at various cantilever/crystal axis angles, it is possible to visualize the 3D domain structure (Fig. 2.15(b)).

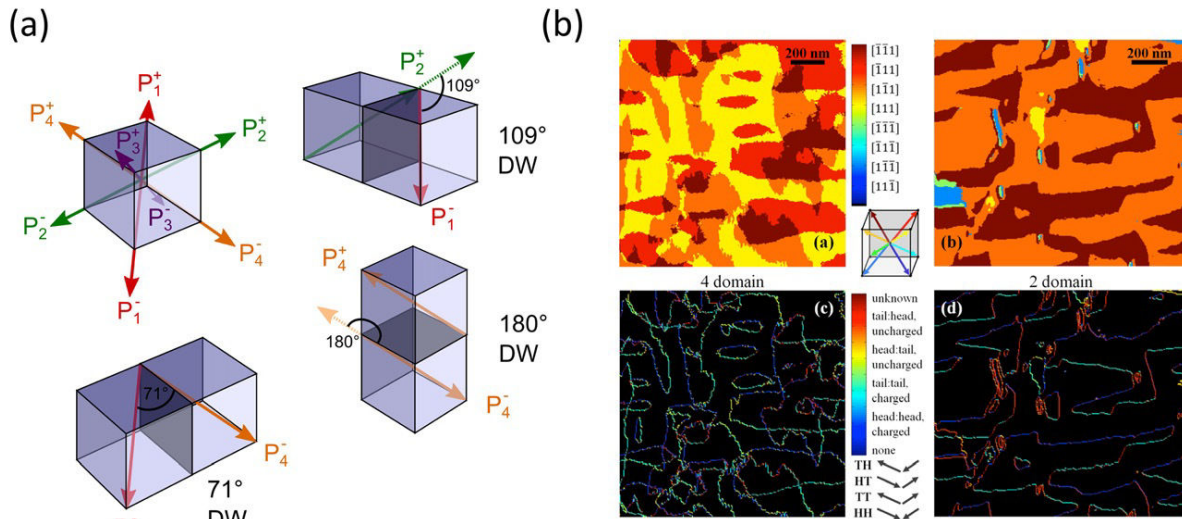


Fig. 2.15: (a) Picture of different domain directions and domain walls in BFO. The polarization can point along any one of the eight directions. Domain walls can be of three types: 109° , 180° or 71° . (b) Piezoresponse force microscopy (PFM) images of BFO thin films. Using various scans with different cantilever angles, the domain structure (top) can be obtained, and the type of domain walls (bottom) can be identified. Figure adapted from [36]

Polarization hysteresis loops are obtained (mainly on thin films since smaller electrical bias is required) when the leakage is sufficiently low (this leakage is a current problem for small band gap BFO material due to the existence, sometimes, of a too large free carriers concentration [35,36]). In (1 1 1)-oriented films, the total ferroelectric polarization can be measured in a capacitor geometry, and values close to $100\mu\text{C}\cdot\text{m}^{-2}$ have been reported. A typical polarization loop obtained for a single crystal is shown in Fig. 2.16.

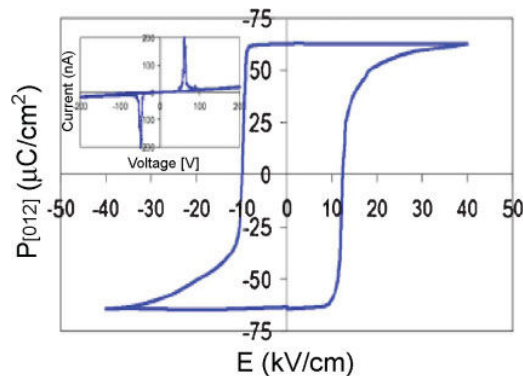


Fig. 2.16. Polarization hysteresis loop for BFO crystal [43].

Coupled properties:

The coexistence of remarkable structural, ferroelectric, magnetic and optical properties at room temperature, and the existence of coupling between them (Fig. 2.17), makes BFO a very interesting multifunctional material that could find some applications in several fields (electronics, spintronics, piezoelectric transducers, actuators and sensors, photonics, etc.).

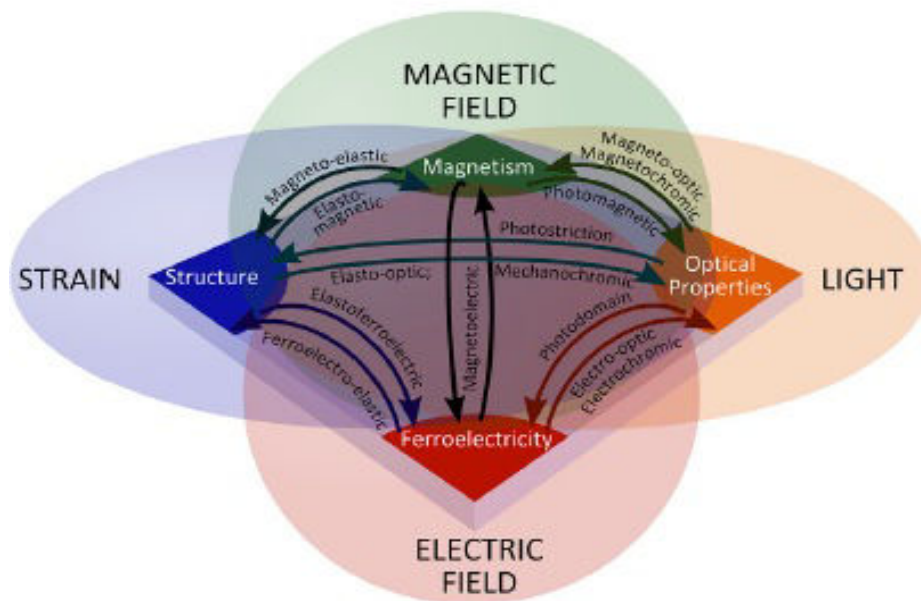


Fig. 2.17: Sketch of possible couplings between the various functionalities of BFO [36].

To illustrate some of the coupled properties we present the magnetoelectric effect which is at the core of the multiferroic properties. Through this magnetoelectric coupling, it is possible to act on the ferroelectric response with a magnetic field or, vice-versa, to control magnetism by electric fields (Fig. 2.18(a)). This property is for example appealing for the design of lowpower spintronics devices in which information could be stored by magnetization, and written by electric fields [44]. An example of possible new RAM, named MERAM (Magneto Electric Random Access Memory), based on exchange bias is shown below (Fig. 2.18(b)) [45].

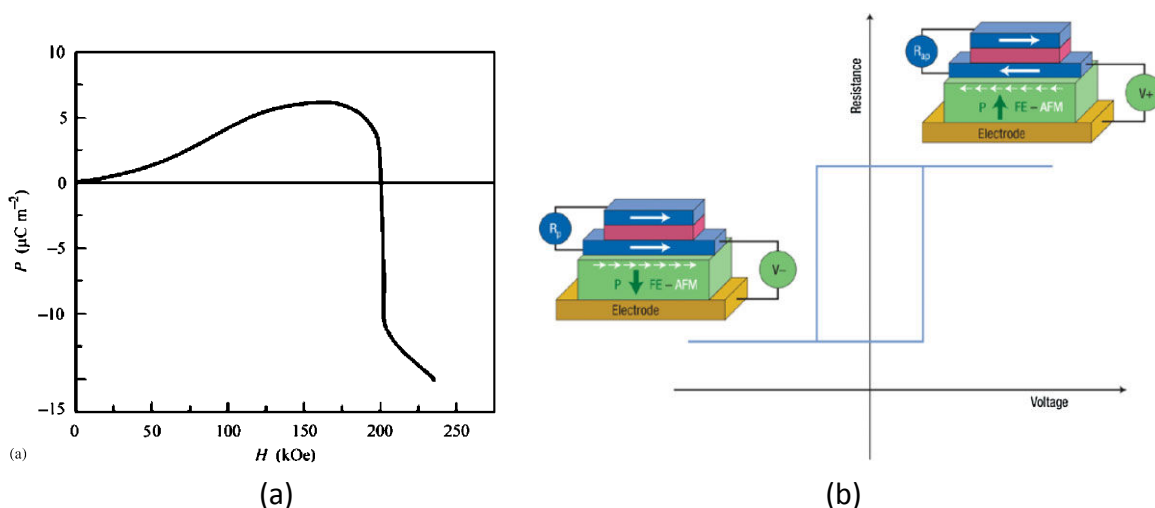


Fig. 2.18: (a) Dependence of the electrical polarization versus external magnetization showing the magneto-electric effect [42]. (b) Example of a MERAM: the green layer is the multiferroic compound while the blue one is the ferroelectric film [43].

In the next chapter we will introduce more specific literature results dealing with ultrafast phenomena in BFO and ferroelectric materials in order to explain the current understanding we have and the remaining issues to address. In this next chapter, we will also present our results and findings concerning the photogeneration and photodetection of longitudinal and transverse coherent acoustic phonons in BFO.

Chapter 3: Generation and detection of coherent acoustic phonons in BiFeO₃.

3.1 Introduction

In this chapter we will present the results obtained in the study of the photogeneration and photodetection of coherent acoustic phonons in multiferroic material BiFeO_3 . This chapter will start with a literature survey dealing with ultrafast electron and phonon dynamics in BFO and also in some other ferroelectric materials like PbTiO_3 . In particular, we will introduce the current understanding and the issues to be still addressed for this rich physics of photoinduced phenomena in ferroelectrics. Then, we will present our results dealing with photogeneration of LA and TA modes in polycrystalline BFO sample with an emphasis on the generation and detection processes. Both room temperature and high temperature measurements ($T > T_{\text{Néel}}$) have been carried out. We will show that BFO is a really interesting solid for the generation of transverse acoustic waves (TA) whose microscopic mechanism is likely to be associated to the inverse piezoelectric effect. We will also show that the detection of coherent acoustic phonons in anisotropic solid like BFO can be complex but reveals original time-resolved Brillouin signals that will be detailed in the dedicated chapter 4.

3.2. Literature survey: Ultrafast electron and phonon dynamics and ultrafast strain in BFO

Different photoinduced dynamics have been studied in BFO over a time scale ranging from hundreds of femtosecond to several nanoseconds and even quasi-static investigation were performed. The dynamics of hot electrons, involving the relaxations processes, the trapping lifetime measurement, as well as the coherent phonons dynamics have been investigated. For the later one, full optical pump-probe experiments as well as visible pump/ X-ray probe were conducted. In this part, we make a brief review of the relevant results in connection with our discussion of the processes of photogeneration and photodetection of coherent phonons that will be presented in the part 3.3.

3.2.1. Study of ultrafast electron dynamics in BFO

A study of the dynamical behavior of the photoinduced carriers is essential for understanding the photoinduced effects in matter (as for example ultrafast photoinduced strain and emission of coherent phonons). Different processes (intra and interband processes) can occur after carrier photogeneration. The relaxation of carriers is usually driven by electron-phonon coupling and because of that depends on the density of states of both electrons and phonons [46, 47]. Both densities are usually different when the crystallographic structure is modified. The structure dependence of the electron relaxation process has been evidenced in two phases of BFO films, namely the rhombohedral and the tetragonal structure. It was shown first that the band gap is different in the two phases as

expected (Fig. 3.1). Secondly, the ultrafast electron-phonon coupling (electron-phonon relaxation time) is also modified (Fig. 3.2) [48]. It turns out that the value of tetragonal film bandgap ($E_g \sim 2.48\text{eV}$) is about 0.2 eV smaller than the bandgap of rhombohedral film ($E_g \sim 2.67\text{eV}$). This result is consistent with the theoretical calculation, which predicts a higher band gap in rhombohedral BFO film [48].

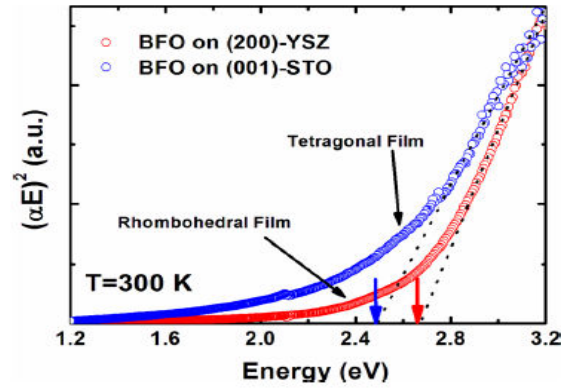


Figure 3.1. Dependence of $(\alpha E)^2$ versus photon energy E allowing determination of bandgap for two crystallographic structures of BFO thin films in room temperature [48].

In the time-domain optical measurements, the relaxation of hot electron exhibits two decay constants corresponding to two distinct processes : the authors have claimed that the faster one corresponds to the scattering of excited electrons with phonons (described by electron phonon coupling constant) while the slower one is attributed to spin-lattice thermalization [48]. It was revealed that electron-phonons interaction strength is larger for tetragonal structure of BFO films than for rhombohedral one. Even if not straightforward, and only qualitative at that time, it was suggested that e-ph interaction is enhanced because of the symmetry breaking in tetragonal BFO films.

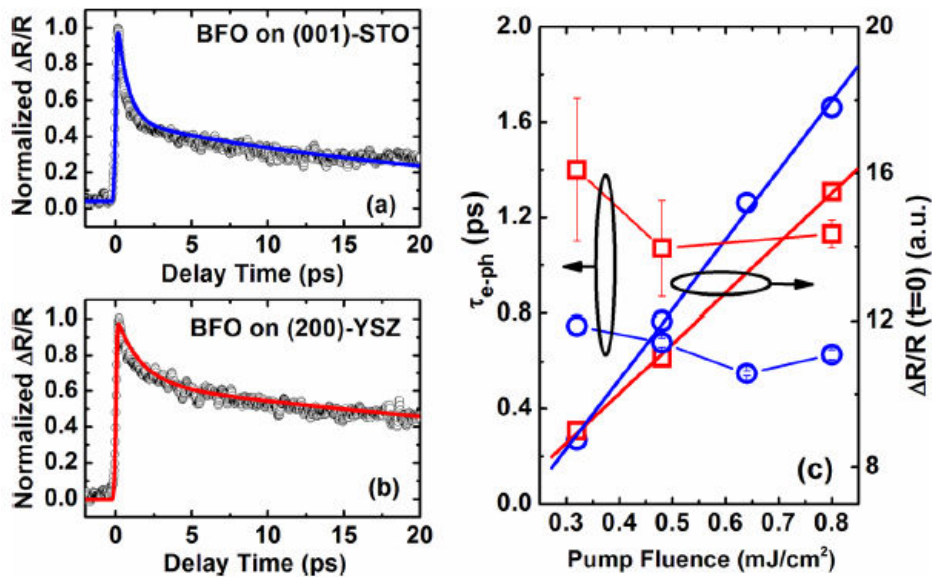


Figure 3.2. Normalized transient reflectivity of a) tetragonal and b) rhombohedral BFO films on (001)-STO and (200)-YSZ respectively. c) Left scale of fluence dependence is e-ph decay time constant for tetragonal (blue) and rhombohedral (red) BFO thin films, right scale

corresponds to amplitude of electronic peak at the moment of excitation (linear with fluence) [48].

There is also reported comprehensive study of ultrafast carrier dynamics in single crystal of BFO [49]. It was realized by degenerate pump-probe spectroscopy, what means that BFO crystal was excited and probed by the same wavelength 400nm ($>3.1\text{eV}$). It was revealed that after relaxation of photoexcited electrons to conduction band minimum, through scattering on phonons in picosecond time scale, the electrons subsequently leave conduction band and primarily decay via radiative recombination on nanosecond time scale. These results are also supported by photoluminescence (PL) measurements. It was mentioned that carrier relaxation dynamics is very similar to that one in bulk semiconductors (intra and interband processes).

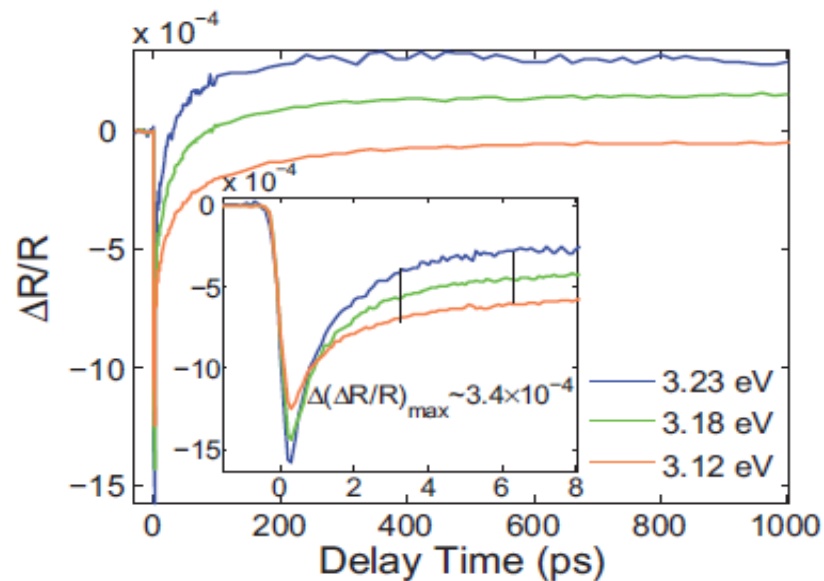


Figure 3.3. Degenerate pump-probe reflectivity measurements at 3 different photon energies at room temperature. The inset displays the early time dynamics showing that the signals, obtained at highest and lowest pump photon energies, reach their maximum difference at $\sim 3\text{ps}$ [49.]

The intraband process electron(hole)-phonon collision in the conduction (valence) band occurs within around 3ps. Furthermore, it is argued that levels of signals after the decay depends on the deposited pump photon energy as shown in Fig. 3.3. Report emphasizes that if consecutive recombination of electrons (at longer time scale than 10ps) was non-radiative, then difference of levels of signals obtained by different pump photon energies would have been the opposite (Fig. 3.3). Therefore authors conclude that radiative recombination is the main mechanism in the ns time range by statement “If the majority of photoexcited electrons radiatively recombine across the gap, then the 0.11eV difference between the highest and lowest photon energies compared to the $\sim 0.4\text{eV}$ excess energy (over bottom of conduction band) should be large enough to visibly change reflectivity signal level” (Fig. 3.3 and 3.4).

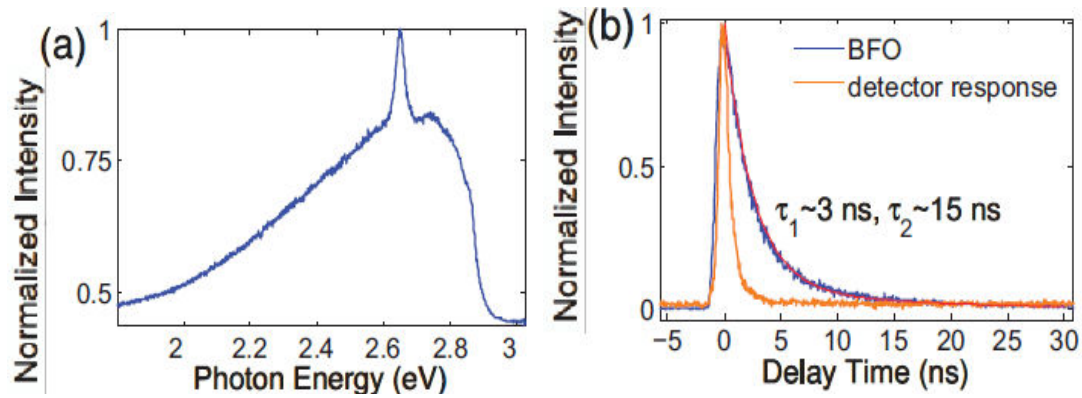


Figure 3.4. a) Photoluminescence spectrum measured by 3.06 eV excitation at room temperature b) Spectrally integrated time-resolved PL measured at room temperature [49].

As it can be observed the measured PL spectrum consists of a sharp peak at about 2.65eV which is contained in a broadband (2.3-2.85eV) PL signal (Fig. 3.4). Sharp peak corresponds to reported bandgap of BFO and originates from electron-hole radiative recombination across the bandgap. Broadband emission is connected to smearing of absorption edge to lower energies. The origin of it can be attributed to the presence of low lying electronic structure (intrinsic effect due to lattice distortion, leading to enhancement of transitions forbidden in principle) or defect states as already observed in semiconductors (extrinsic effect). Since this effect is observed in most ferrites (in different forms) and is stronger in materials with larger crystal distortion, it is likely that it is intrinsic property of BFO [49].

Finally temperature-dependent experiments was also performed to test the influence of antiferromagnetic (AFM) order on carrier dynamics in BFO (Fig. 3.5). Decrease of electronic peak amplitude (initial magnitude of transient reflectivity signal in the moment of excitation) with temperature was observed. Shift to the earlier times of the point where signal changes from negative to positive was also observed. It can be explained by higher deposition of thermal energy with increased temperature during relaxation of electrons in conduction band, which is probably caused by bandgap decreasing with temperature ($dE_g/dT < 0$) [37] and correspondingly more excess of electron energy versus bottom of conduction band takes place.

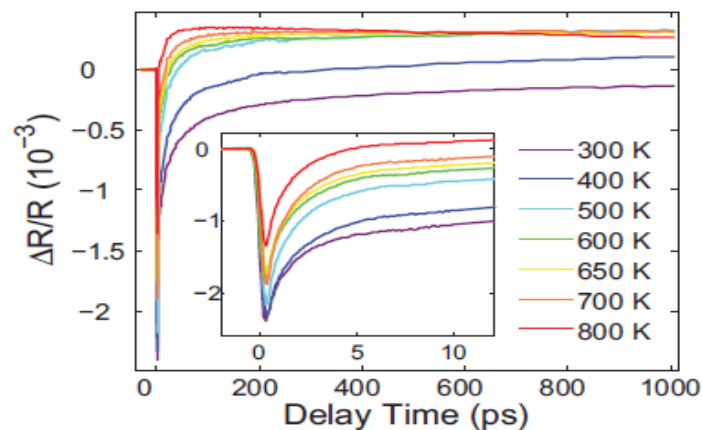


Figure 3.5. Photoinduced (pump photon energy ~ 3.18 eV) transient reflectivity change at various temperatures. The inset shows the dynamics on short timescales [49].

No significant temperature dependence of the electron relaxation time was reported versus temperature and even through the Néel temperature. They also mention, that up to their observation, the spin-lattice relaxation does not play a significant role in observed dynamics, since no abrupt change in measured signal was observed across T_N [49]. In chapter 3 (part 3.4) we will further discuss this phenomenon.

Another group obtained complementary characteristics of electron dynamics. They studied optical response and dynamical behavior of photocarriers in BFO by measurements of transient photoabsorption (TA) and photocurrent (PC) in BFO thin films [50]. In their work relaxation and recombination of photocarriers in BFO thin films were investigated using a combination of transient absorption, which revealed two exponential decay components, and time-resolved photocurrent, which reflects population of free photocarriers. In the experiment, sample was excited over the bandgap by pump pulse with photon energy 3.1eV and was probed by white light pulses. The TA and PC decay dynamics revealed a fast component (~ 1 ns) attributed to the localization of free carriers to shallow trap states and slow one (~ 100 ns) corresponding to the recombination of trapped carriers (Fig. 3.6). Obtained results are claimed as the evidence of long-living trapped photocarriers.

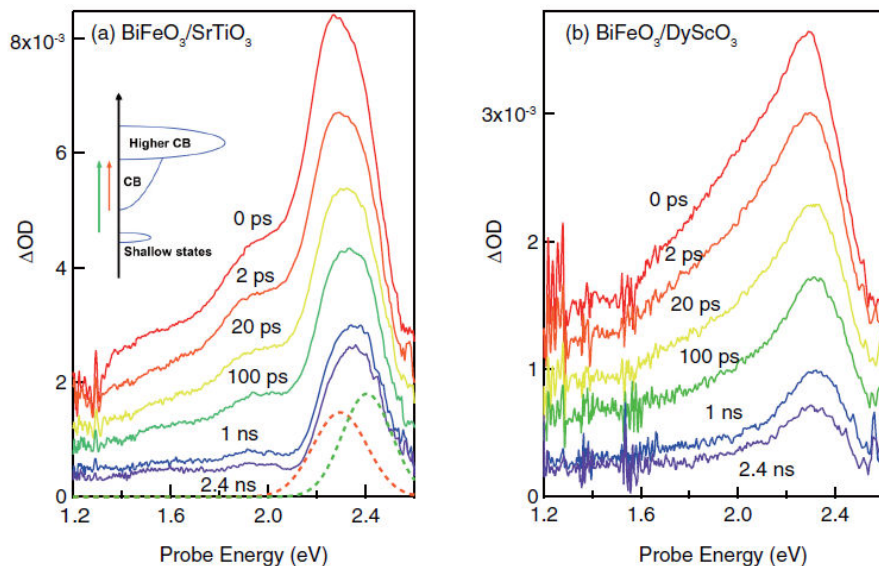


Figure 3.6. Transient absorption spectra of a) BiFeO₃/SrTiO₃ and b) BiFeO₃/DyScO₃ for different delay times. The inset illustrates the energy levels of BiFeO₃ [50].

It is worth to notice that on transient absorption spectra obtained for two kind of thin films, absorption peak about 2.3-2.4eV is revealed which corresponds to the energy of bandgap of studied samples (this value is slightly smaller – 0.2-0.3eV- than that reported in [38-41]). This can be caused by preparation procedure or selected substrates of thin films (epitaxial stress is one of the key point in BFO thin film properties [36]).

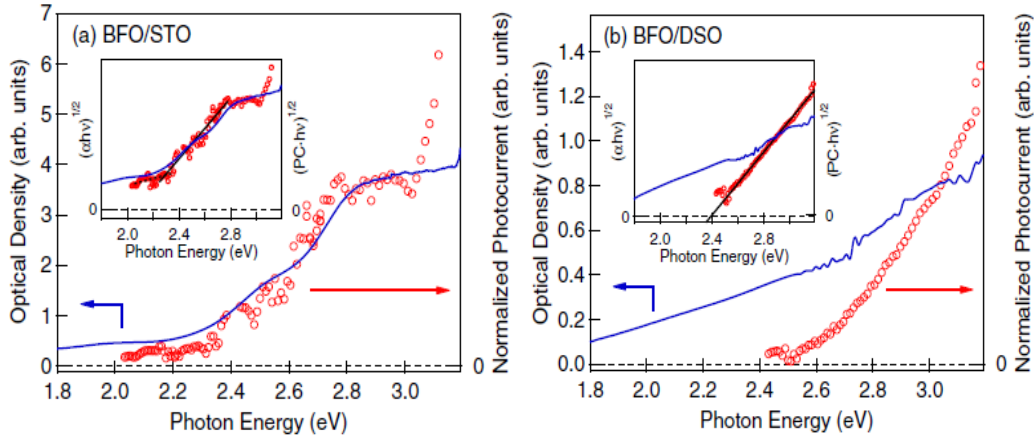


Figure 3.7. Optical absorption and PC excitation spectra of a) BFO/STO and b) BFO/DSO. The insets presents Tauc plots of optical absorption and PC to reveal value of bandgap [50].

In Fig. 3.7, the transient photocurrent (PC) is given. Since PC is sensitive only to mobile carriers, PC signal is not sensitive to trapped carriers and consequently does not exhibit signal in the region 1.8eV/ 2eV. Tauc plots of the PC reveal a linear variation in the PC of both BFO/STO and BFO/DSO, which is evidence of an indirect transition according to the authors.

3.2.2. Study of ultrafast photoinduced strain in BFO

The first experiment of photogeneration and photodetection of coherent acoustic phonons in BFO was reported in 2012 and was performed on single crystal [51]. The experiment was conducted with above band-gap excitation (400nm) and below band gap detection (800nm). Besides the electronic response (~ 1 ps), already generally discussed previously, the transient optical reflectivity signal revealed some oscillatory components arising from a Brillouin process (see Eq. 2.3). Because of the low symmetry orientation of the crystal, LA and two TA modes were evidenced. These results have permitted to show that BFO has an important potential for generating both LA and TA waves. Moreover, these results offer the opportunity to evaluate the elastic properties of this solid that at that time were not well known.

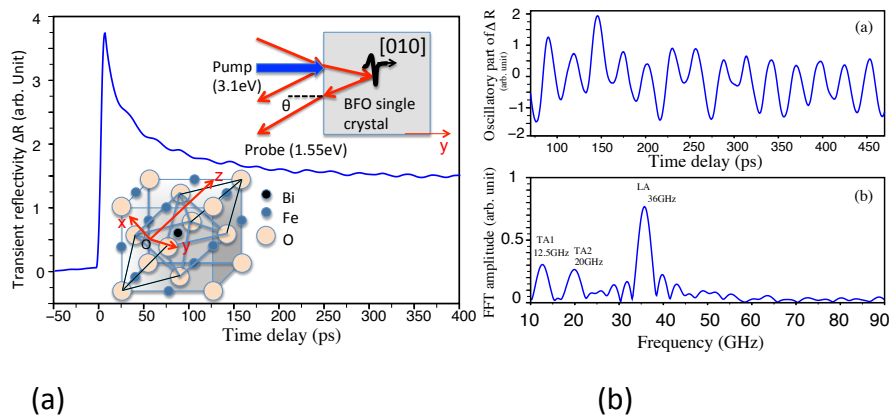


Figure 3.8: (a) Transient optical reflectivity signal obtained on single BFO crystal. (b) The corresponding FFT of the signal (with baseline removed) evidences the LA and TA coherent acoustic phonons [51].

Nearly in the same time, ultrafast photoinduced strain in BFO thin films with variable thicknesses was studied by dual-color pump-probe spectroscopy [52]. In this study it was argued that photoinduced strain (called by authors also as photostriction) is optically anisotropic and is mainly driven by the optical rectification effect. Samples were excited by pump light at wavelength 400nm and probed at 800nm. Change of amplitude and frequency of Brillouin oscillations during transmission of acoustic strain through the BFO/substrate interface was observed (Fig. 3.9(a)-(b)). By localization of this moment in time, it was possible to obtain the value of the propagation time of acoustic pulse through the different BFO thin film thicknesses and in consequence evaluate speed of propagation of acoustic strain through the (110) orientation of BFO. One can simply notice that propagation time through the film scales linearly with thickness. From this speed of propagation of acoustic strain along [110] direction of BFO was estimated to be about 4.76km/s.

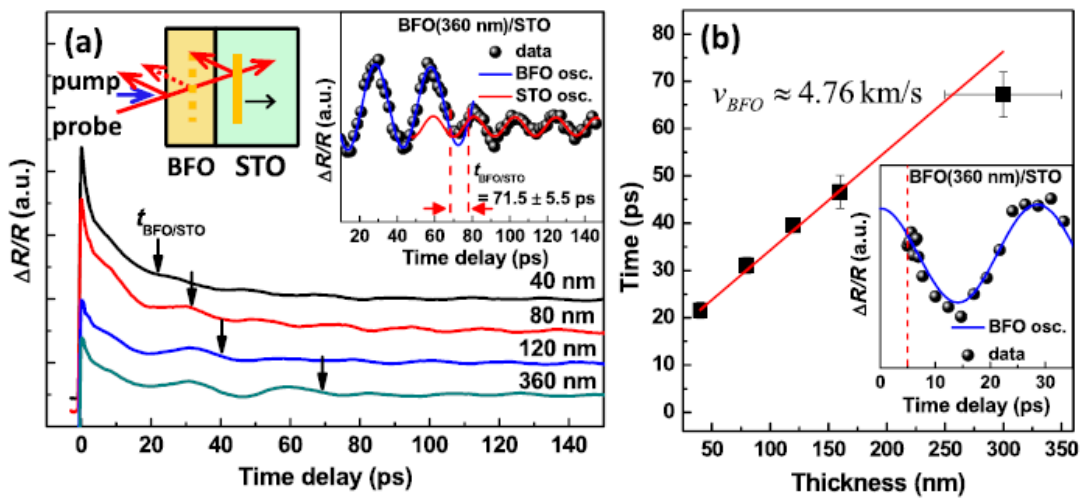


Figure 3.9. a) Transient reflectivity signal with oscillatory component for different thicknesses of (110) oriented BFO thin films. The arrows indicate BFO/STO interface. Left inset: schematic illustration of the propagation of strain pulse inside BFO and STO substrate. Right inset: example of extracted oscillatory signal. b) Linear dependence of acoustic strain propagation versus thin film thickness. Inset used to extract period of oscillations [52].

Speed of propagation can be also extracted from the period of Brillouin oscillations with a value 4.88km/s consistent with previous report [51]. To better understand the mechanism of ultrafast photo-generation of strain in BFO, further studies of dependence of transient reflectivity signal versus orientation of sample and pump polarization angle were carried out. It can be noticed that amplitude of signal at zero time (electronic peak at the moment of excitation) does not depend on orientation of sample, what indicates that photo-induced excitation is isotropic in BFO thin films. On the other hand, the amplitude of Brillouin oscillations varies a lot with orientation of thin film, what indicates anisotropy in process of generation and/or detection (Fig. 3.10(b)). In order to avoid influence of birefringence on the process of detection, a pump polarization dependence study was also realized with a fixed probe polarization. As shown in Fig. 3.10(d), a small modulation of Brillouin amplitude was observed with a maximum variation of around 21%.

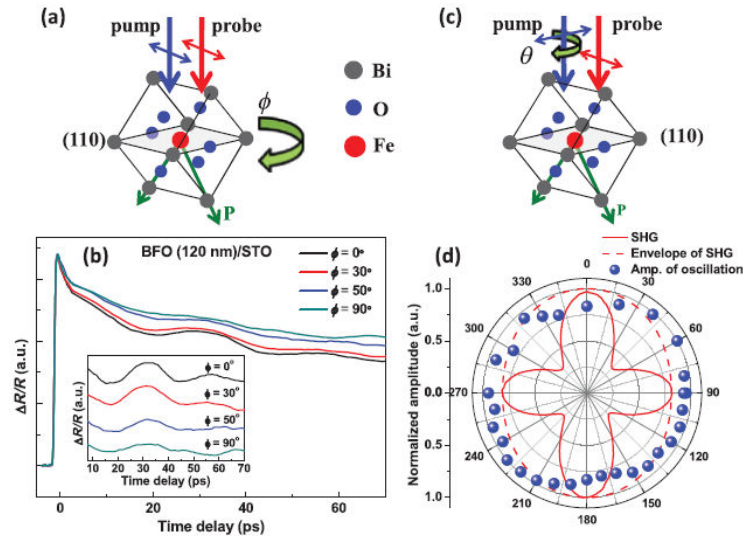


Figure 3.10. a) The experimental configuration (sample rotation) for signals presented in b). b) Measurements of transient reflectivity signal versus orientation of BFO thin film. Inset: extracted and magnified oscillatory component. c) The experimental configuration (pump polarization rotation) for results presented in d). d) Dependence of amplitude of Brillouin oscillations and SHG conversion efficiency versus pump polarization [52].

Similar two fold symmetry with maximum to minimum ratio (19%) was observed in envelope of second harmonic generation pattern from BFO thin film. Therefore it was supposed that similar modulation and dependence of these two processes share the same mechanism. It was argued that the optical rectification is responsible for the ultrafast anisotropic photostriction in BFO similarly to what was discussed in previous studies performed with single crystal of BFO in quasi-static light excitation regime [53].

Ultrafast strain generated by laser pulses can be also studied by time resolved X-ray diffraction (TRXRD). In these kind of experiment visible photoexcitation is carried out while the probe process is achieved with X-ray pulses. In that case, it is possible to observe direct evolution of lattice dynamics by this technique since Bragg shift is directly connected to the lattice strain. In such experiment it was shown that photoexcitation can induce large transient out-of-plane strain in BFO thin film [54].

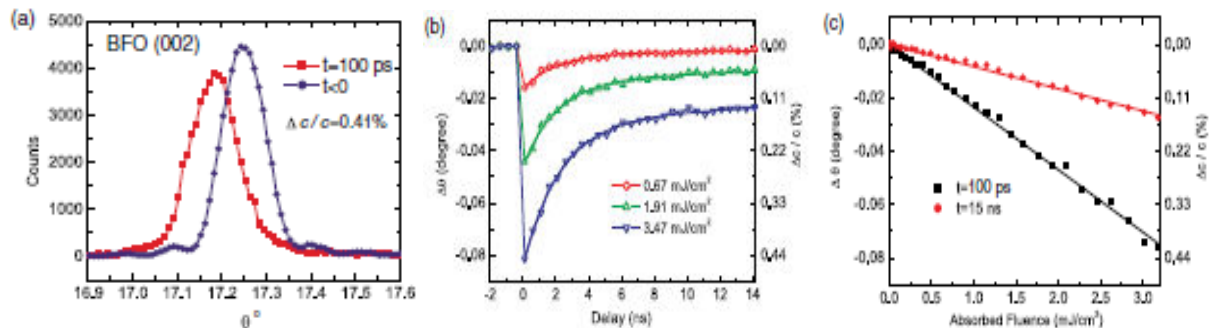


Fig. 3.11. a) Angular shift of (002) Bragg peak 100ps after laser excitation revealing ultrafast expansion of lattice, b) Time dependence of angular Bragg peak shift with recalculated evolution of induced strain for different fluences of excitation, c) Angular Bragg peak shift

and corresponding strain as a function of absorbed fluence at 100ps and 15ns after excitation [54].

Shift of Bragg peak to lower angles was observed under laser excitation, showing expansion of lattice. Broadening of shifted Bragg peak was also observed, caused probably by induced strain gradient arising from the inhomogeneity of the optical excitation (Fig. 3.11(a)). Time dependence of angular Bragg shift and corresponding evolution of strain was measured for different fluencies of excitation (Fig. 3.11(b)). From these measurements bi-exponential decay of strain was obtained with fast time constant about 2ns for all applied fluencies. Linear dependence of photoinduced strain versus absorbed fluence was also obtained (Fig. 3.11(c)) over a very large range of fluence (0-3mJ/cm²).

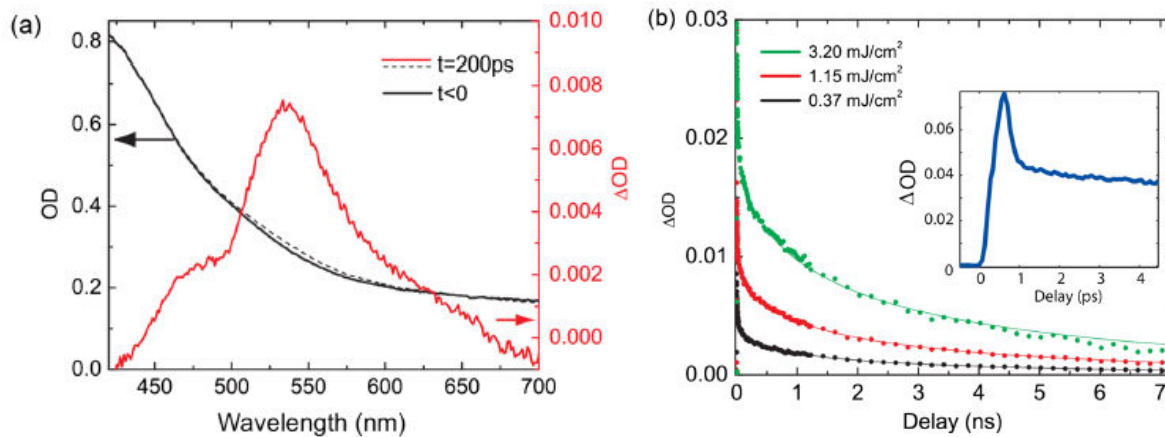


Fig. 3.12. a) Left scale: Optical absorption spectrum in units of optical density (OD) before (solid line) and after (dashed line) laser excitation of BFO film at fluence 3.2mJ/cm², Right scale: extracted change of optical density at 200ps after laser excitation (ΔOD , red curve), b) Transient absorption at 540nm as a function of time for 3 various absorbed fluences with fits using biexponential decay. The inset shows initial dynamics at picosecond time scale [54].

Additional measurements of ultrafast optical absorption were performed, which revealed that relaxation of charge carrier population occurs within similar time scale as decay of photoinduced strain (2ns) (Fig. 3.13(a)). Therefore it was shown that electronic and structural responses are correlated, what led to conclusion that electronic mechanism of lattice expansion mainly dominates, rather than thermal expansion. It was proposed that dominating nonthermal component of photoinduced strain is caused either by piezoelectric distortion due to screening of depolarization field by photoexcited carriers, or by direct modification of crystal structure through populating of the antibonding states of the transition metal [54].

Finally, because of duration of X-ray pulses (100ps), these measurements were not enough to resolve dynamics of strain formation under laser excitation. Only strain relaxation was accessible by this experiment.

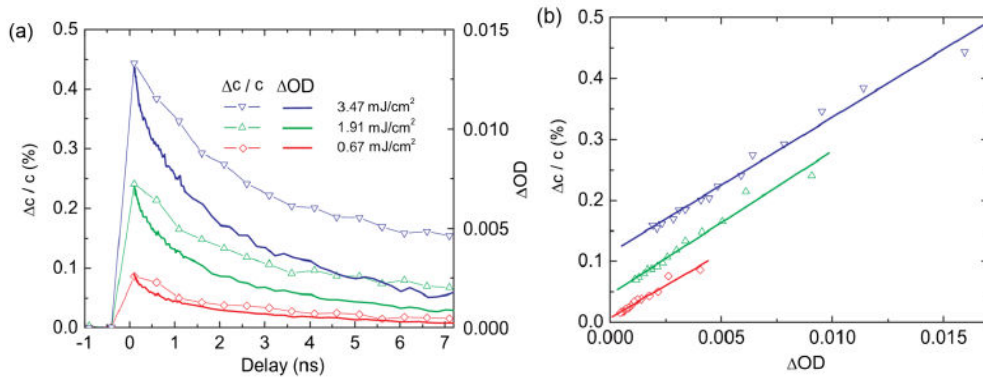


Fig. 3.13. a) Comparison of time evolution of photoinduced strain relaxation ($\Delta c/c$) with transient absorption decay (ΔOD) for various fluences of excitation, b) Linear dependence of photoinduced strain versus transient absorption at various fluences (with solid fits) [54].

To get insight into emergence of ultrafast strain in sub-picosecond time scale, complementary measurements were done with femtosecond X-ray pulses (200fs) obtained from laser-driven plasma x-ray source (PXS, pulses of x-ray radiation obtained by intense pulses of laser light). Evolution of structural response in about 10ps was observed [55]. Substantial Bragg peak broadening was again observed, indicating inhomogeneous spatial stress profile. It was concluded that negative strain (expansion) appeared quasi-instantaneously and decay of strain at nanosecond time scales was confirmed.

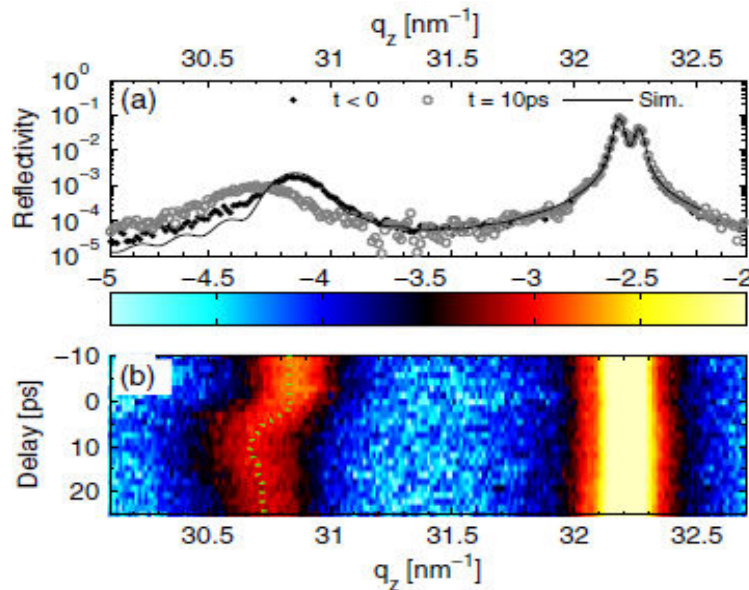


Fig. 3.14. a) Rocking curves of the 002 pseudocubic Bragg reflections from the BFO layer and STO substrate measured by the PXS, b) Measured transient rocking curves (diffracted intensity in logarithmic scale). The dotted line indicates the extracted center of the BFO Bragg peak [55].

As it can be observed on Fig. 3.14 the Bragg peak shift (decrease to smaller angles) occurs during about 10ps after laser excitation. The peak shift of the BFO 002 pseudocubic reflection measures the average out-of-plane strain (in the z direction) in the BFO thin film.

The observed shift to smaller q_z corresponds to an ultrafast expansion $\Delta c/c \approx 0.5\%$ of the BFO film along the surface normal [55].

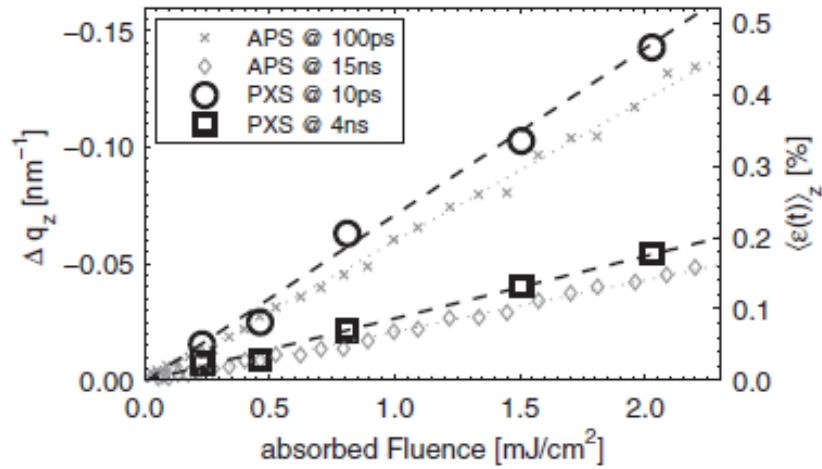


Fig. 3.15. Shift Δq_z of the 002 pseudocubic BFO Bragg peak and corresponding average strain $\langle \epsilon(z,t) \rangle_z$ measured as a function of fluence at different delays (for two different experiments). The dashed and dotted lines represent linear fits [55].

Linear dependence of Bragg shift versus pump fluence was again observed for different time delays, corresponding both to appearance of ultrafast strain (early delays at ps timescale) and decay of strain (late delays at ns timescale) as observed in Fig. 3.15 [55].

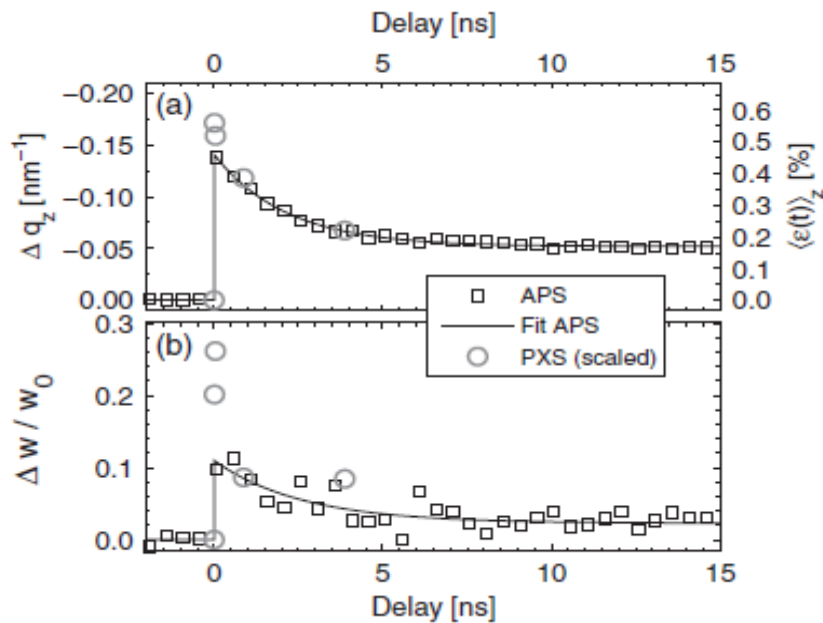


Fig. 3.16. a) Dependence of Bragg peak shift (with corresponding strain in z direction on right axis) versus delay time of probe pulse obtained from synchrotron (APS) and laser driven plasma x-ray source (PXS), b) Dependence of relative change of Bragg peak width $\Delta w/w_0$ versus delay time [55].

A relationship between Bragg shift decay (decay of strain) and width decay is then established as observed in Fig. 3.16. The decay of strain was fitted by exponential function

with time constant $\tau_{\text{shift}} \approx 2.29 \pm 0.14 \text{ ns}$ [55]. The width w inversely depends on the number of scattering atomic layers (size broadening) and on the inhomogeneous strain within the film (strain broadening). It was assumed that the change of the width Δw depends linearly on the spatial variation $\Delta_z \langle \varepsilon(z,t) \rangle$ of the strain: $\Delta w(t) \propto \Delta_z \langle \varepsilon(z,t) \rangle$. With only homogeneously strained film ($\Delta_z \varepsilon = 0$), no additional peak broadening would have been observed ($\Delta w = 0$). The transient width Δw revealed then a significant inhomogeneous strain profile in the BFO thin film over the whole observed time scale. It was extracted time constant of the width decay from the exponential fit which gave value $\tau_{\text{width}} \approx 2.31 \pm 0.92 \text{ ns}$ very similar to the time constant of strain decay. Based on these measurements, a discussion about the photoinduced strain mechanism was developed. First of all, the mechanism by thermal expansion was negligible as temperature rise was not enough for observed amplitude of strain. It was estimated that maximal thermal strain just after excitation is about 0.08%, which is only small fraction of observed value close to 0.5%. It was also argued that deformation potential mechanism can be excluded as if it would be dominant mechanism, it should lead to contraction of lattice under laser excitation, according to pressure dependence of the bandgap of BFO [56] (see equation 2.10). Finally it was concluded that depolarizing field screening (DFS) cannot be also dominant mechanism. According to this mechanism photoexcited electrons and holes should screen internal polarization of ferroelectric domains by macroscopic transport in internal electric field, what should lead to modification of this field and in consequence launch strain through inverse piezoelectric effect. It was stressed that as there is finite time required for transport of carriers through bulk material to the interfaces of the film to screen the depolarization fields, it cannot explain quasi-instantaneous stress required to be consistent with results. Finally, the lack of observation of saturation of strain with fluence (which is accepted as an evidence of the inverse piezoelectric effect [9, 19-21]) is also against this model of a screening of the internal electric field over a large distance. At high fluences saturation of DFS should be observed indeed, whereas it was observed only linear response of strain in all range of applied fluences. As all these mechanisms were excluded or claimed as not dominant, another mechanism was proposed. It was argued that directly after excitation there is mainly ultrafast (quasi-instantaneous) redistribution of electron density within single BFO unit cells what influences local ferroelectric polarization at the level of unit cell. A model of local charge carrier displacement was proposed within the BFO unit cell after photoexcitation leading to an instantaneous stress due to inverse piezoelectric effect.

Very similar TRXRD was realized with thin film of PbTiO_3 (PTO) [57] (Fig. 3.17 and 3.18). TRXRD were used to visualize atomic displacements on femtosecond time scales and photoinduced changes in unit-cell tetragonality were observed. It was shown that lattice dynamics was actually driven by the motion of photogenerated free carriers within the ferroelectric domain. Experiments were performed on 20nm PTO thin film deposited on SrTiO_3 (STO) substrate. PTO grown on STO forms below Curie temperature (T_c) out-of-plane c-axis oriented domains due to lattice mismatch imposed by STO. The sample was excited by third harmonic 266nm of the a Ti:Sa laser with duration of 40fs. It was irradiated with maximum fluence 5 mJ/cm^2 what corresponds to power applied by single pulse about 100 GW/cm^2 . Probe x-ray pulses with duration 60fs full width at half maximum (FWHM) and

wavelength 1.39\AA were obtained at the Linac Coherent Light Source giving about 10^{10} photons/pulse at repetition rate of 60Hz. The time resolution of this measurement was limited by timing jitter between laser and x-ray pulses, estimated to be 100fs [57]. From the position of Bragg reflections, out-of-plane lattice parameter c inside of thin film was probed as a function of x-ray pulse delay versus exciting laser pulse. When it is heated uniformly c -axis contracts as T_c is approached, because of negative thermal expansion coefficient in this direction. This contraction indicates decrease in the dipole moment of unit cell and leads to the shift of out-of-plane diffraction peak to higher scattering angles. Under laser excitation Bragg peak corresponding to out-of-plane lattice parameter shifts toward higher angles in about 5ps. This is consistent with a uniform contraction of the unit cell in the out-of-plane direction and occurs on an acoustically limited time scale, determined by the film thickness over the sound velocity ($v_s = 4000$ m/s). Subsequently, it was observed a long-lived, symmetric shift of the diffraction peak to lower angles occurring on a 10ps time scale, in contrast to what would be expected from simple heating of a ferroelectric [57]. Finally thin film relaxes to the initial state in nanosecond time scale before subsequent excitation.

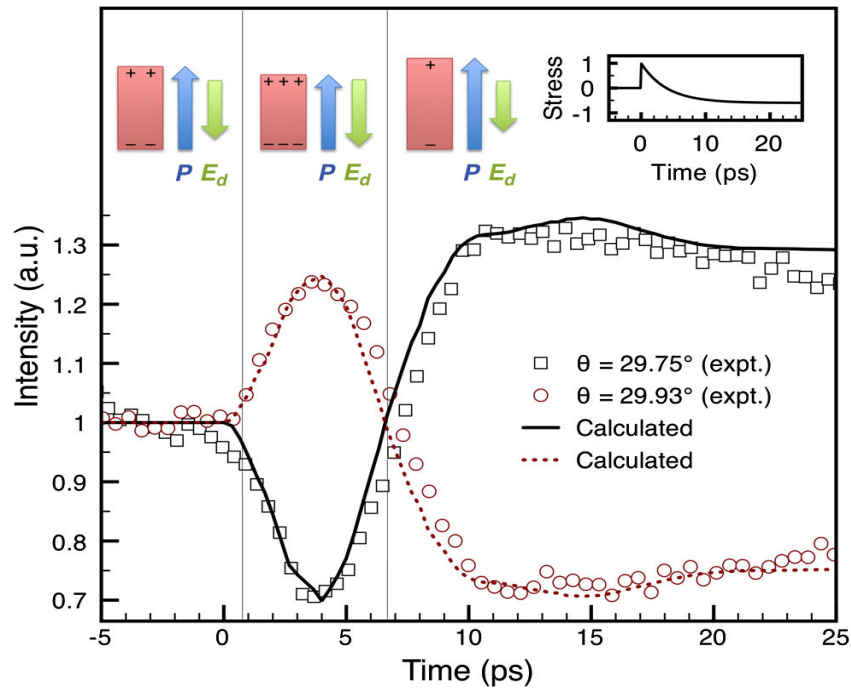


Fig. 3.17. Schematic of unit-cell response. At $t = 5$ ps, the c lattice parameter reaches a minimum due to the piezoelectric response to the increase in the depolarization field (E_d) induced by the shift current. At $t > 10$ ps, carriers have moved to screen the depolarization field, driving a long-lived expansion of lattice parameter [57].

To explain this shift of Bragg peak in two opposite directions (corresponding to subsequent ultrafast contraction and expansion of lattice) during several picoseconds it was proposed two step mechanisms driven by the displacement of electrons first against and then along the polarization direction. First, the initial decrease in the lattice parameter during the first 5ps is caused by a shift of current, associated with a photoinduced, coherent shift of electrons away from the free surface. This current, directed along the polarization direction, increases the charge density at the interfaces, giving rise to an increase in the depolarization

field and an impulsive stress which leads to contraction of the lattice [57]. Then, the transient current reverses direction as the generated electrons and holes move to screen the depolarization field, leading to an increase in the c lattice parameter what is schematically presented on the Fig. 3.17.

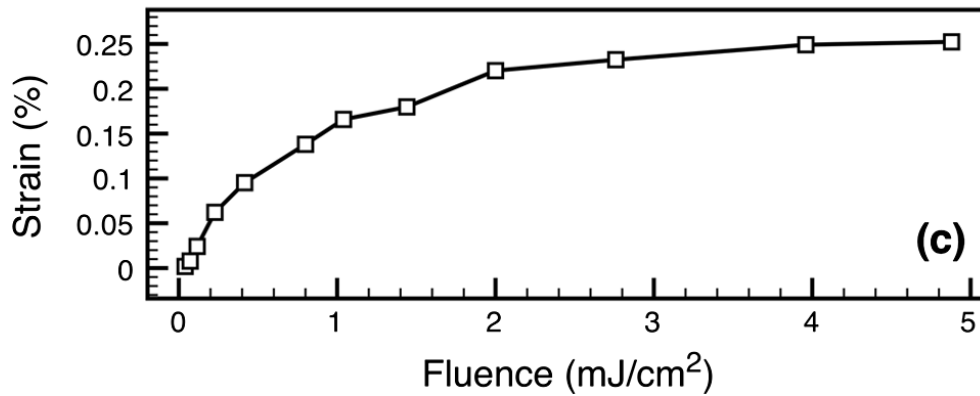


Fig. 3.18. Strain in the c parameter of monodomain PTO on STO as a function of fluence, measured at $t = 100\text{ps}$. It can be observed saturation of strain at high fluences [57].

Saturation of strain with increasing fluence of excitation was observed. This behavior is consistent with mechanism of screening of depolarizing field by excited free carriers as internal field saturates when is fully cancelled. This saturation is consistent with what was first observed in fully saturated piezoelectric semiconductors [9,19-21]. Besides, shift of Bragg peak and lattice dynamics is not observed in centrosymmetric paraelectric phase of PTO on another substrate DSO, where internal depolarizing fields do not exist because of centrosymmetric unit cell. This additionally confirms internal field screening by free charges in ferroelectric phase of PTO.

There is another class of experiments revealing the ultrafast dynamics of excited charges in ferroelectrics. These experiment are based on emission and detection of terahertz radiation (THz) [58, 59]. It has been shown that radiated terahertz pulse directly reflects polarization state of ferroelectric domains, indicating that THz radiation results from ultrafast modulation of spontaneous polarization. THz radiation has been observed from multiferroic BiFeO₃ thin films under illumination by femtosecond laser pulses (Fig. 3.19). The THz emission in BFO is explained as a time-dependent modulation of the internal electric field due to light-induced photo-excited carriers. In Fig. 3.19, the dependence of the polarization of the THz radiation generated in BFO on the bias electric fields applied to BFO thin film, is evidenced. Both pulses are nearly identical with similar amplitude and pulse width about 0.84ps, except of phase inversed by π [58, 59]. Different polarization of emitted pulse definitely reflects another ferroelectric polarization induced by electric field bias. Therefore it was shown that it is possible to inverse phase of emitted THz waveform by switching of ferroelectric polarization, and what is more such state is stable and memorized.

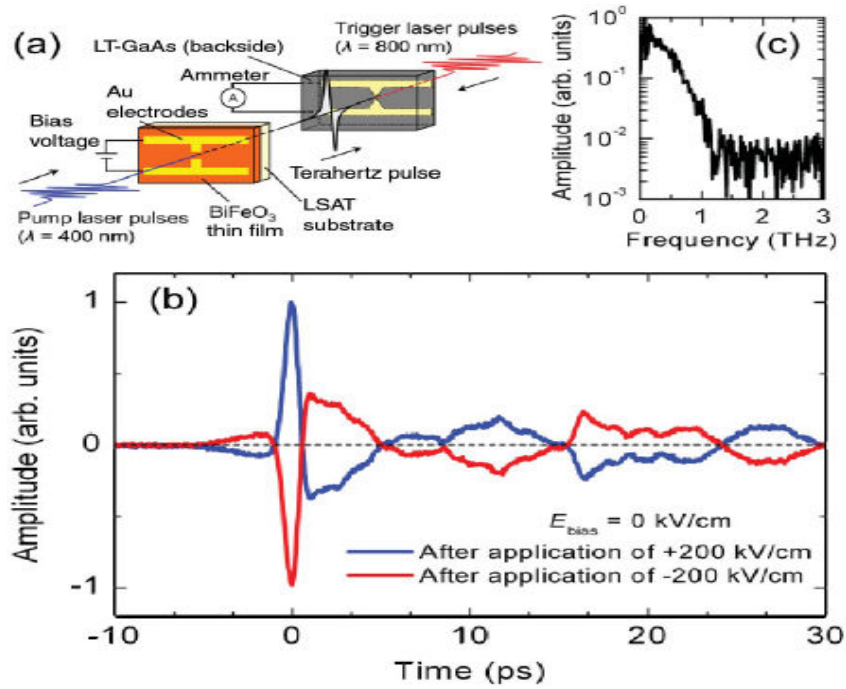


Fig. 3.19. a) Scheme of experiment for generation and detection of THz radiation. b) Time-domain waveform of the THz pulse radiated from the BiFeO₃ photoconductive switch measured at a zero-bias electric field after applying a bias electric field E_{bias} of ± 200 kV/cm. c) Frequency spectrum of emitted radiation form Fourier transform of detected amplitude spectrum [58].

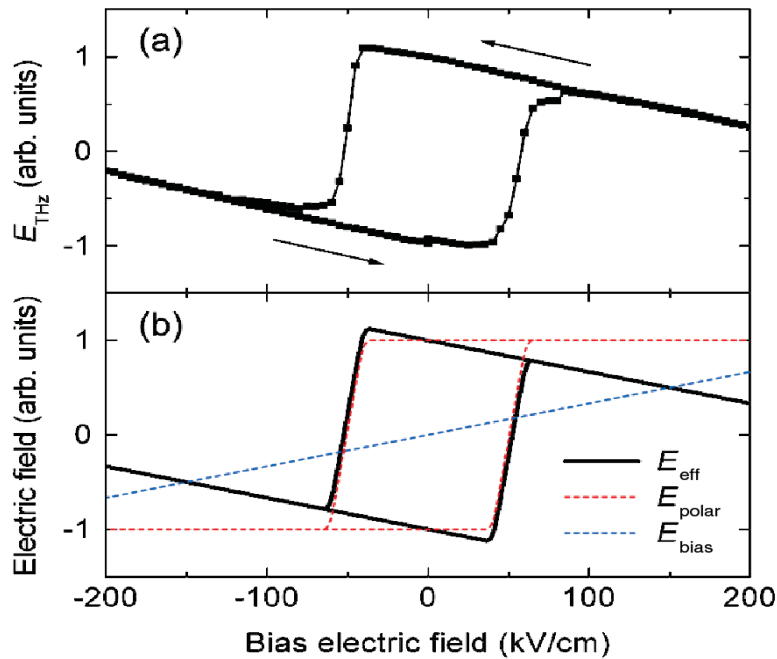


Fig. 3.20. Main peak amplitude of the THz pulse E_{THz} radiated from the BiFeO₃ photoconductive switch as a function of the applied bias electric field. b) Model of the macroscopic electric field induced to a pair of electrodes in typical ferroelectrics for understanding the tilted hysteresis loop in (a). E_{eff} , E_{polar} , and E_{bias} represents the effective electric field induced between the electrodes, the electric field derived by electric

polarization, and the applied bias electric field respectively. E_{eff} is expressed by $E_{polar} - E_{bias}$ [58].

To get more insight into process of THz generation, variable electric field was applied additionally to the BFO switch. Hysteretic behavior of THz radiation amplitude was observed in function of applied electric field. Besides hysteresis loop was titled additionally. For nonferroelectric photoconductive switches, linear relationship was reported before with applied electric field, with change of phase of emitted radiation together with inversion of electric field polarity. Therefore observed hysteresis loop in THz radiation reflects ferroelectric nature of BFO thin film. Such a hysteresis loop was explained by considering the macroscopic electric field biased to a pair of electrodes. The effective macroscopic electric field E_{eff} induced to a pair of electrodes can be expressed by $E_{eff} = E_{polar} - E_{bias}$, where E_{polar} represents the electric field derived from electric polarization. [54-55] Applied biasing electric field leads to tilting of hysteresis loop. These features show the direct relationship of THz radiation with polarization state, which emerges as a result of ultrafast polarization modulation introduced by the mobile photoexcited charge carriers. Following mechanism can be explained in the way that upon illumination by a single laser pulse, the accumulated charges associated with polarization become partially compensated instantaneously due to the screening by the photoexcited carriers. This modulation of polarization gives rise to THz radiation via dipole radiation according to classical electrodynamics.

3.3. Results: Ultrafast light-induced tunable LA and TA phonons source in BFO at room temperature

As a short introduction, we remind that we carried out the investigations on a polycrystalline sample. A single crystal have been studied previously in 2012 [51] but only one crystallographic orientation was available which limits the study of the generation and detection processes of coherent acoustic phonons. Moreover, the surface of that available single crystal was not as good, even after conventional polishing, which requires pretty long integration time. As we will see in the following, the polycrystalline samples offers unique possibility to investigate variable crystallographic orientations by selecting some grains and original findings are reported on the coherent acoustic phonons physics. All the experiments presented in part 3.3 have been conducted at room temperature. High temperature investigations have been conducted to evaluate the role of the antiferromagnetic order on the LA and TA modes generation that will be presented in part 3.4.

3.3.1. Sample preparation and characterization

3.3.1.1 Synthesis and preparation

BiFeO_3 powders were synthesized by conventional solid-state reaction by mixing in stoichiometric proportions high purity oxide of Bi_2O_3 and iron oxide Fe_2O_3 as starting compounds. Two consecutive calcinations in air at $T=800$ °C for 2h were needed to obtain pure perovskite BiFeO_3 , free of any impurity phase. The as-grown powders were then pressed to get a pellet which was heated in air at $T=800$ °C for 2h to finally obtain a BiFeO_3

ceramic with an average grain size of approximately 20 μ m. The samples were prepared in SPMS lab at Ecole Centrale Paris in the group of B. Dkhil.

3.3.1.2. Characterization of grains and their distribution in the polycrystalline sample.

Image obtained by scanning electron microscopy shows porous structure of polycrystalline BFO sample (Fig. 3.21). It can be noticed that average size of grains is about 20-30 μ m. With use of SEM, spectrum of secondary electrons emitted by BFO was also measured and based on this it was made component analysis showing average content of constituent elements.

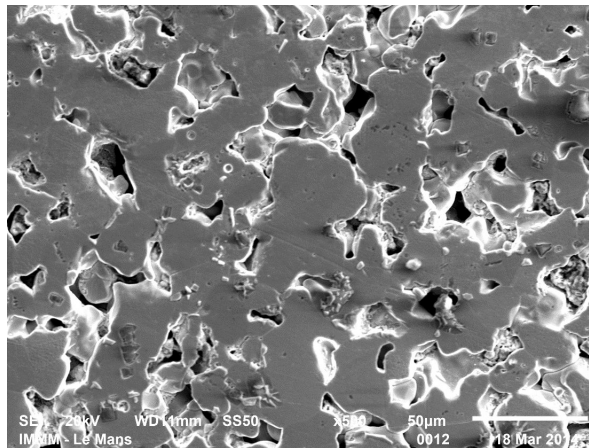


Fig. 3.21. Spectrum of secondary electrons emitted by BFO sample in SEM measurements.

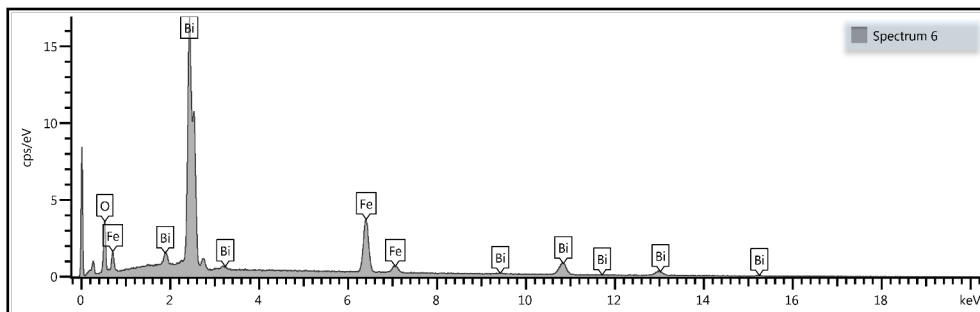


Fig. 3.22. Scanning electron microscopy (SEM) image polycrystalline BFO sample (Oxford Instruments).

Element	Atomic %
O	57.49
Fe	21.42
Bi	21.09
Total:	100.00

Table 3.1. The percentage content of constituent elements.

It can be noticed that based on obtained analysis there is a slight excess of iron and bismuth atoms and corresponding deficiency of oxygen atoms. It should be kept in mind that it can lead to defects and oxygen vacancies inside the BFO structure. Moreover, this technique is a surface technique only. The additional material characterization (Raman, EBSD), more sensitive to bulk properties, show however that the structure is the right one.

3.3.1.3. Electron Back Scattering Diffraction (EBSD) characterization (SPMS, Ecole Centrale Paris)

A Leo Gemini 1530 Carl Zeiss emission high resolution scanning electron microscope was used to map the surface of a polycrystalline ceramic. The average grain size was proved to be around $20\mu\text{m}$ and the mapping of the crystallographic orientation of each grain at the surface of the sample was possible using electron backscattering diffraction (EBSD).

The EBSD experiments were performed at a 70° detector position to sample surface and with a gun lens acceleration voltage of 20kV. These measurements were carried out and analyzed using the EDAX Orientation Imaging Microscopy software v7. EBSD patterns were collected following a scanning routine with different step size for large and reduced areas of sample surface. To deduce the local crystal orientation, each pattern was indexed according to the bulk R3c BiFeO₃ unit cell (hexagonal lattice $a=5.588\text{\AA}$, $c=13.867\text{\AA}$, point group [C3v] [3m]). Resulting EBSD mappings are depicted in Fig. 3.23, generated from overlapping of the inverse pole figures (in color scale, see the inset for crystal orientation in the rhombohedral frame) and quality images (in grey scale, dark grey indicating the largest error found when indexing using BFO reference unit cell). From these maps it can be confirmed that every grain presents a given crystal orientation within the confidence allowed by the EBSD pattern indexing and that no preferential orientation is seen in the ceramic sample (details about EBSD analysis can be found in [60]).

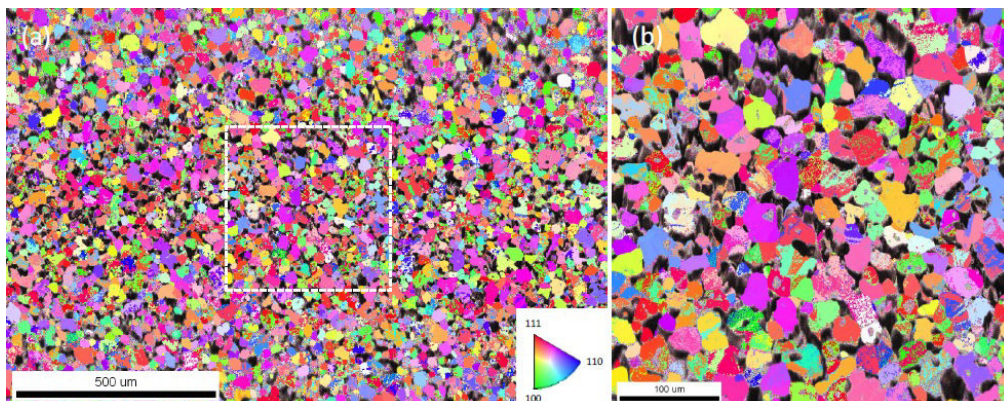


Fig. 3.23. EBSD orientation maps generated from inverse pole figures (color scale) on a) $(1000 \times 1500) \mu\text{m}^2$ large area and b) $(400 \times 400) \mu\text{m}^2$ selected area from (a) (indicated by square). Grey regions on the sample are identified as holes, as deduced from the topography

seen in SEM images. Inset: Color scale correspondence to the rhombohedral crystal directions on the EBSD mappings (prepared in Ecole Centrale Paris by I. C Infante).

3.3.1.4. Raman spectroscopy

Raman spectroscopy studies have been carried out on the BFO ceramic to study the structure and to illustrate that each single grain behaves like a single crystal and thus has its own crystallographic orientation. The Raman experiments were conducted using a Labram Horiba Jobin Yvon spectrometer at 632.8nm laser wavelength and beam focused by 50x objective lens. Typical spectra on single grains are depicted in Fig. 3.24, using analyzer/polarizer parallel (Fig. 3.24a) and perpendicular (Fig. 3.24b) configurations.

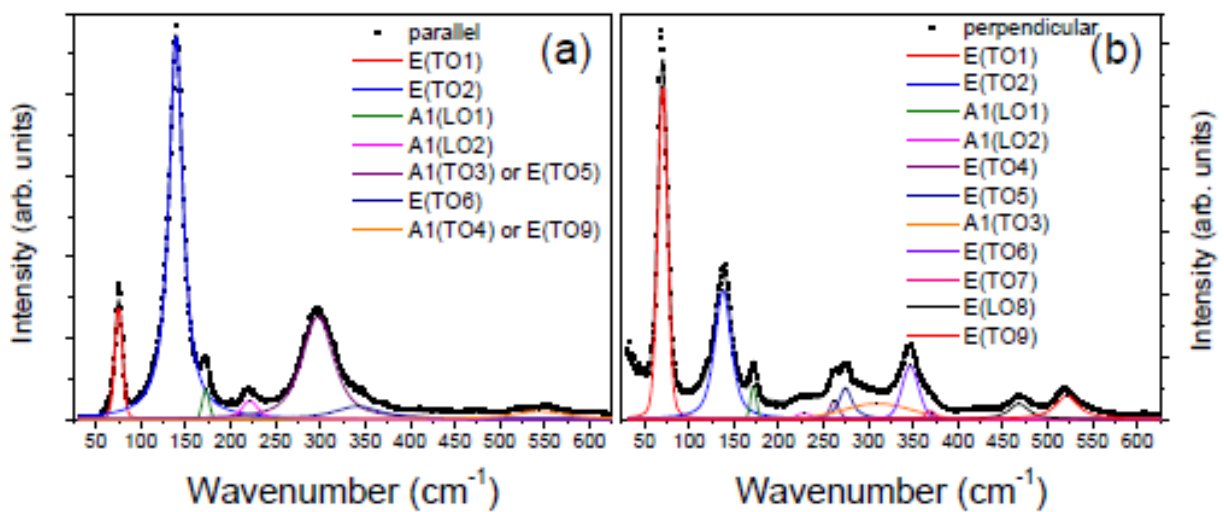


Fig. 3.24. Polarized Raman spectra collected at room temperature on single grain of the BFO sample, using a configuration of the linear polarization of the polarizer and analyzer a) parallel and b) perpendicular (prepared in Ecole Centrale Paris by P. Gemeiner).

These spectra are characteristics of bulk rhombohedral BFO [18, 19]. The change from parallel to perpendicular polarizations configurations shows a strong variation in the intensity of some modes, which is clear feature attesting that each grain behaves like a single crystal.

3.3.2. Photoinduced coherent shear and longitudinal strain in specific orientations of BFO grains at GHz frequency.

3.3.2.1. Pump probe experiments: experimental conditions and procedure

For pump-probe experiment Ti:sapphire femtosecond laser was used with pulse duration of 200fs (which establishes limit of time resolution), pulse repetition rate of 80MHz (80 million pulses per second, what corresponds to pulse every 12.5ns). In order to get some above band gap excitation, the BFO sample was excited by light obtained from second harmonic generation (SHG) with wavelength 400 (3.1eV) or 415nm (3 eV) depending on the setup used. 400nm pump was used when classical two-color pump-probe setup was ran with a

probe wavelength fixed at the harmonic 800nm. 415nm pump was used and obtained by SHG of the harmonic of the Ti:sapphire laser fixed at 830nm which is the required synchronously pumping wavelength of the OPO (Optical Parametric Oscillator). With this OPO, the sample was probed by wavelengths ranging from 560nm to 620nm. Intensities used usually were about 1mW both for pump and probe light and both beams were focused to the size close to 10 μ m. This gives a fluence of absorbed pump pulse of about 10 μ J/cm². Some details of the femtosecond setup are given in Appendix 1.

At first glance, it may be surprising that both pump and probe beam have the same intensities, since probe beam is expected not to disturb sample with respect to pump beam. The reason why it is correct, relies on the fact that probing was undertaken with below bandgap light-matter interaction. Skin depth of BFO for photon energies close to 3eV is in the range 40-50nm [39-42], therefore most of energy is absorbed close to the sample surface and high energy density of pump laser radiation is deposited. On the other hand photons of probe radiation (both 800nm and 590nm) have energies smaller than energy of band gap, therefore not enough to excite electrons from valence band to conduction band (it could happen only at very high fluencies in multiphoton absorption process). Consequently at these wavelengths, the sample weakly absorbs the probe radiation and BFO can be treated as semitransparent with skin depth at least of the order of several micrometers (it is actually difficult to know the exact value). If skin depth of probe radiation is of the order 10³ times bigger than that of pump (which is likely to be at least), then the density of deposited energy beneath the surface is about 1000 times smaller for probe than for pump beam. Therefore probe beam even at the same powers and intensities can be treated as weakly disturbing sample when compared to pump beam. For probe signal only important is light reflected from free surface and scattered from excited and propagating acoustic pulse.

The experiments were conducted at normal incidence (electric fields of pump and probe beams parallel to the irradiated surface) (Fig. 3.25). Transient reflectivity of probe beam was measured (evolution of reflectivity after pump excitation) versus time. Both pump and probe beams were perfectly superimposed in space and focused on sample surface with an achromatic microscope objective magnification of \times 6-10. Pump beam was modulated at a frequency of 80kHz. Probe beam reflected from sample surface was detected by photodiode. A balanced detection process is used in order to remove low frequency laser fluctuations. The difference between the sample signal and a reference signal is obtained with a balanced photodiode (cut-off frequency of 125kHz) and the signal demodulated with a lock-in amplifier. To find good signal on a selected grain, the sample was scanned in x-y surface plane perpendicular to incident beams with micrometric mechanical stages. During scanning of sample surface by probe beam, voltage on photodiode was recorded. When probe beam was for example located between two grains or on the edge of one grain it was strongly scattered and diffracted, therefore reflected light was weak and corresponding photodiode signal was low. Only when beam was centered on big enough grain and with

enough quality of surface, reflected beam was sufficiently strong and gave desired voltages.

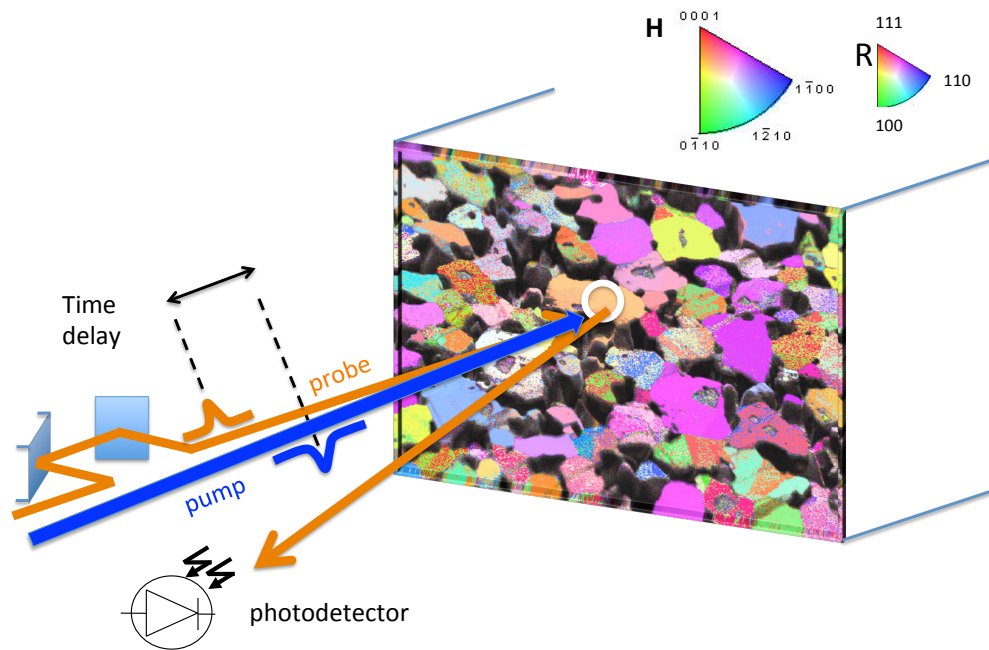


Fig. 3.25. Schematic representation of pump-probe experiment with pump and probe beams focused at normal incidence on single grain of polycrystalline BFO (white circle depicts area of laser irradiation). Probe beam is delayed versus pump and reflected part is received by photodetector (it is slightly deflected on picture for clarity). The colored mosaic indicates the correspondence between colors and the crystallographic orientation (H hexagonal or R rhombohedral frames (see Fig. 3.23 for EBSD analysis)). Figure adapted from [60].

When such position was found during scanning, signal from grain was registered. Good quality of signal was found in this way only from some grains. In a lot of cases signal was very noisy what indicated substantial scattering of light on the surface. Therefore only some of tested positions (some grains) were selected (20 over 100), studied deeper and analyzed. Signals were registered in range of delay times up to 3ns with clearly visible acoustic signals. Taking into account order of speed of longitudinal acoustic (LA) pulse $\sim 5000\text{m/s}$, it leads to conclusion that it was possible to detect coherent phonons in depth up to about $15\mu\text{m}$, which is distance comparable with size of the grain. It clearly shows that probe light could then deeply penetrate the grain up to several micrometers.

3.3.2.2. Results

One scan on full range of delay time took about 1-2 min. It was necessary to repeat and register at least several tens of such scans to remove noise and to get better statistics. More than 100 grains from thousands of grains in polycrystalline BFO sample were studied. More than 20 grains gave some signals with good quality. One full measurement to get good

quality signal took about 1h. The signals are shown in Fig. 3.26. The first two presented signals (grain 1 and 2) are obtained by a pump excitation fixed at 415nm (3.0eV) and probed at 590nm (Fig. 3.26(a)) and the two others (grain 3 and 4) obtained with a pump and probe wavelengths fixed at 400nm (3.1eV) and 800nm respectively (figure 3.26(c)). At time $t=0$ ps, a sharp variation of the transient optical reflectivity appears, due to the excitation of the electronic cloud. We do not focus on this electronic part already described in part 3.2.1. This electronic response (EE) is followed by oscillations that are Brillouin oscillations (see Eq. 2.3 and [51]). It can be noticed that whereas amplitude of electronic peak is very similar, Brillouin oscillations (BO) can be very different from grain to grain. One can conclude that the same population of photoexcited carriers couple differently with lattice to emit acoustic phonons. Contrary to what was previously observed in one single BFO crystal [51], a more rich coherent acoustic phonons spectrum is revealed (Fig. 3.26). Three acoustic modes are typically generated in the BFO grains: one quasi-longitudinal (QLA) and two quasi-transverse, or shear (QTA1 and QTA2).

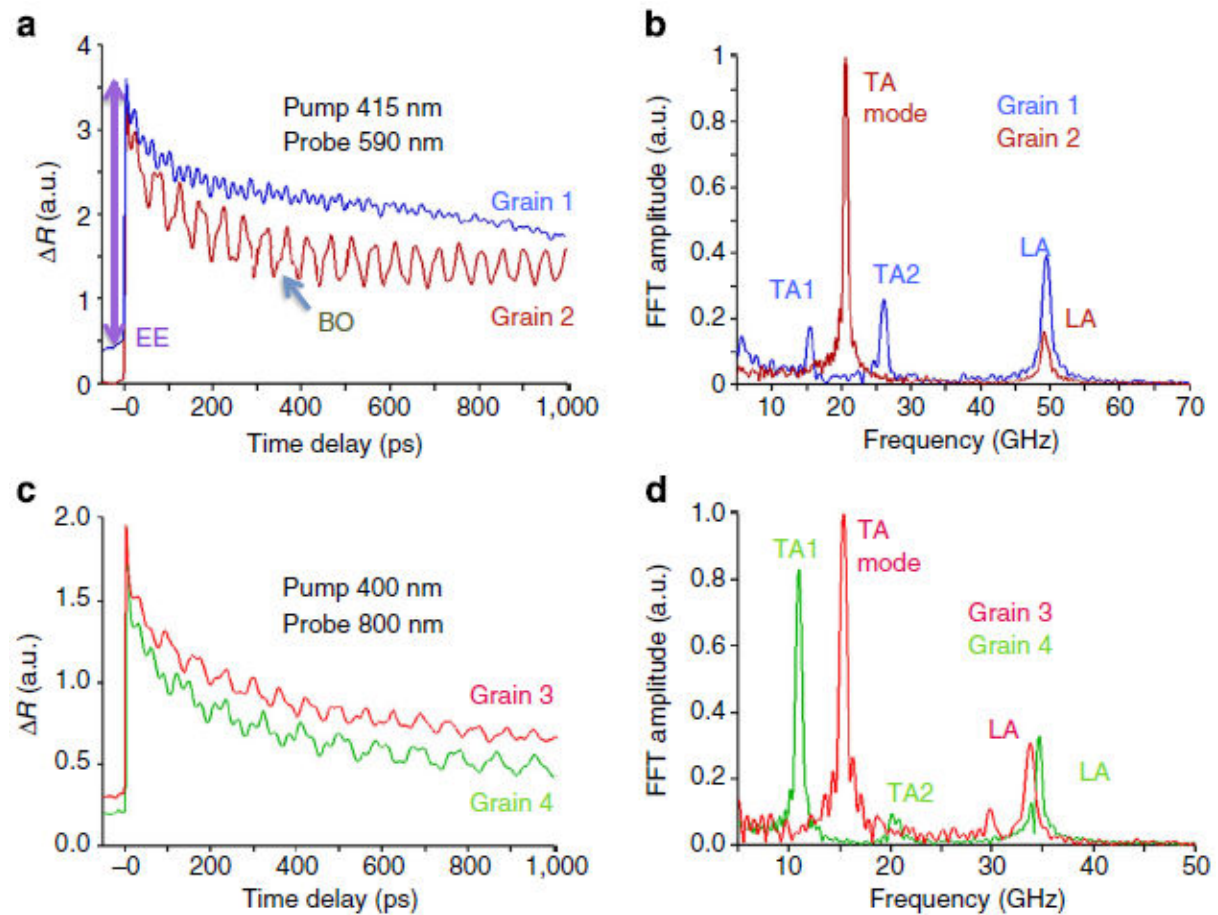


Fig. 3.26. Signals (a, c) and Fast Fourier Transforms (FFT) (b, d) obtained from different grains of polycrystalline BFO sample by pump 415nm and probe 590nm (a, b), or by pump 400nm and probe 800nm (c, d). Probe light was circularly polarized. Figure adapted from [60].

Moreover, we observed various responses indicating clearly that the photo-induced/photo-detected strain depends on the grain crystallographic orientation. The Fast Fourier Transforms (FFT) bring into prominence that the Brillouin frequency, i.e. the acoustic velocity, changes as a function of the lattice orientation, in particular that of the TA modes

(Fig. 3.26 (b) and (d)). For grain 2 (Fig. 3.26.b) we can notice a spectacular large TA amplitude which is roughly 6 times larger than that of the LA mode.

Such high amplitude of TA mode and especially ratio TA by LA mode amplitude has never been reported in any material or nanostructure before. In most of metals and semiconductors, the magnitudes of detected TA phonons are usually much weaker than that of the LA phonons. To enhance shear mode generation, broken symmetry is required. Despite many strategies to introduce asymmetry in metals [8,9] and semiconductors [61], only similar amplitude of TA as LA signal was obtained in the best case. In table 3.2, a summary of the reported ratio of TA/LA signals in various materials is given.

Material	GaAs [9]	Zn [8]	GaN [61]	BiFeO ₃ [60]
TA mode frequency (GHz)	~20	~25	63	10-25
TA sound velocity (m/s)	~3000	~2700-3200	4240	2000-2200
Ratio of TA/LA amplitude	~0.2	~0.2-0.5	~1	~6

Table 3.2. Comparison of TA to LA signal amplitude ratio obtained in different materials by introducing asymmetry in structure.

It is worth to notice that if we look carefully to the FFT spectrum for the grain 2 and 4, the LA peak exhibits some asymmetry or even there is split into two components. This effect arises from the optical birefringence and two components in the Brillouin peak come from the probe light scattering with ordinary and extraordinary component [42]. We can make profit of this splitting to locally probe the exact grain orientation, or at least to know how the $[111]_R$ direction (*i.e.* ferroelectric orientation) is oriented respectively to the surface of the grain [62]. The detailed procedure is given in Appendix 2. This splitting is clearly observed on the signal of the grain 5 (Fig. 3.27). In time-domain signal, the Brillouin signal evidences some modulation (beatings). The FFT reveals two very close frequencies at 37.3GHz and 34.5GHz with similar amplitudes corresponding to LA mode.

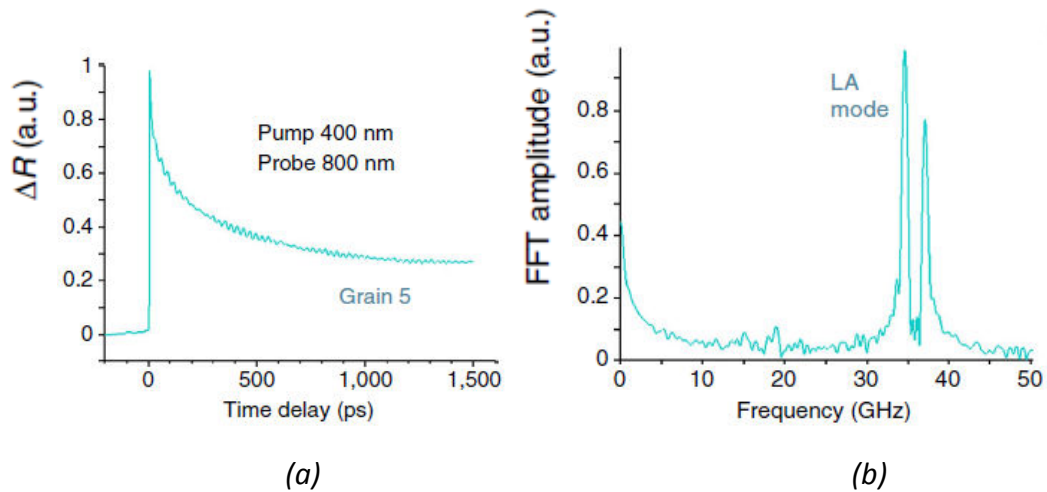


Fig. 3.27. (a): Signal with modulated Brillouin oscillations detected by probe wavelength 800nm, (b) FFT of modulated signal with splitted LA mode. Probe light was circularly polarized. Figure adapted from [60].

For this grain we can notice that there is no TA mode (Fig. 3.27(b)). The absence of TA mode will be of particular interest for discussing the generation process (see 3.3.2.3).

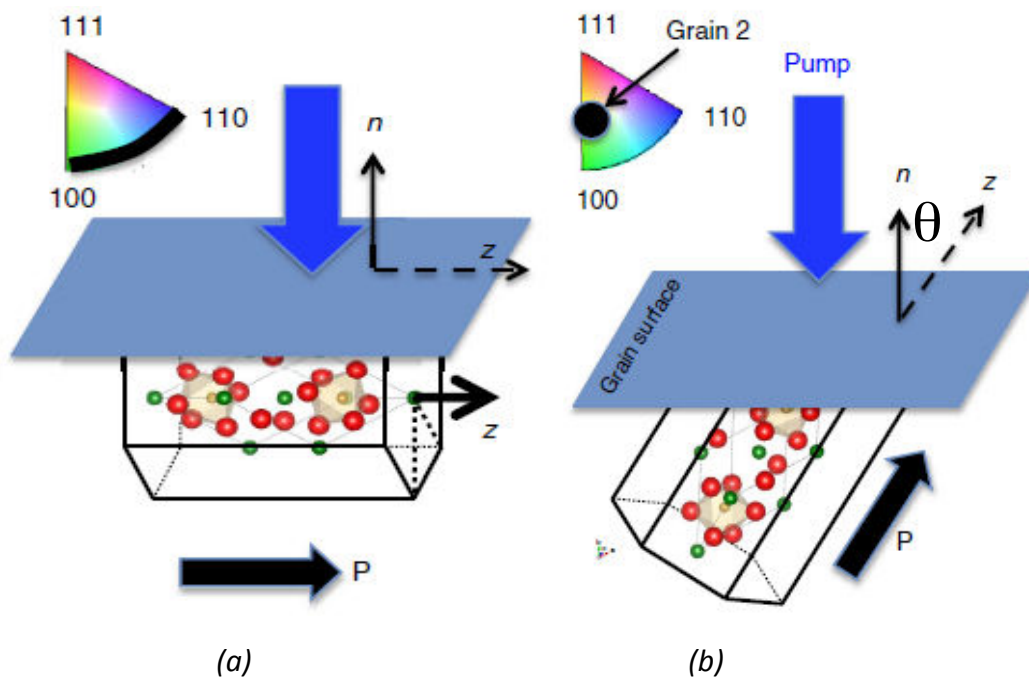


Fig. 3.28. (a) Typical orientation of grain 5: crystallographic axis, optical axis and ferroelectric polarization in plane ($\theta \cong 90^\circ$). (b) intermediate orientation of the grain 2 ($\theta \cong 24^\circ$) or the grain 6 ($\theta \cong 28^\circ$).

As the last example of the LA and TA signals we can see the response of a grain (grain 6) with an disorientation of 28° probed by linear polarization of light. This grains also exhibit large TA signals.

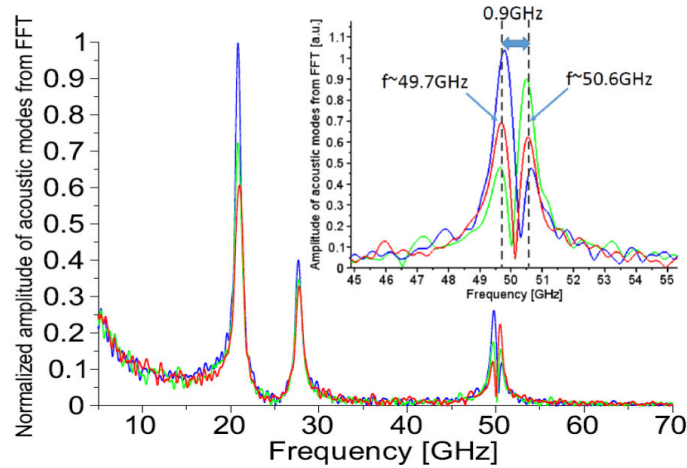


Fig. 3.29. FFT of the acoustic signal obtained for grain 6 ($\theta=28^\circ$). The grain exhibit large TA signals with a clear splitting of the LA mode coming from the optical birefringence effect. The signal has been recorded for variable probe polarizations to clearly evidence the contribution of the ordinary (mode at 50.6GHz) and extraordinary (49.7GHz) light.

Pump effect on acoustic generation – fluence and polarization dependence

To study the mechanisms of acoustic generation in selected grains, pump fluence dependence of signal was realized (Fig. 3.30). Linear dependence of amplitude of electronic excitation was obtained consistently with previous reports. Both the LA and TA mode amplitudes increase also linearly with the pump fluence consistently with previous work, for the LA mode at least [54, 55]. No effect of saturation of Brillouin amplitude was observed. Moreover, no preferential saturation of the TA mode in comparison to the LA mode is observed like it has been evidenced for GaAs [9].

The influence of pump beam polarization on signal was also checked. For the given grain 2 and pump fluence, polarization of pump beam was rotated by half- plate. No dependence of Brillouin amplitude versus pump polarization was observed. It means that direction of pump polarization does not have significant role in ultrafast process of electronic excitation and generation of acoustic strain. It was reported similar experimental result about Brillouin amplitude dependence versus pump polarization in thin BFO film which also did not show direct influence of pump polarization on generated strain in thin BFO film [52]. As we shall underline, this result rules out some predominant contribution of the electrostriction mechanism discussed in the part 3.3.2.3 (see also Eq. 2.12).

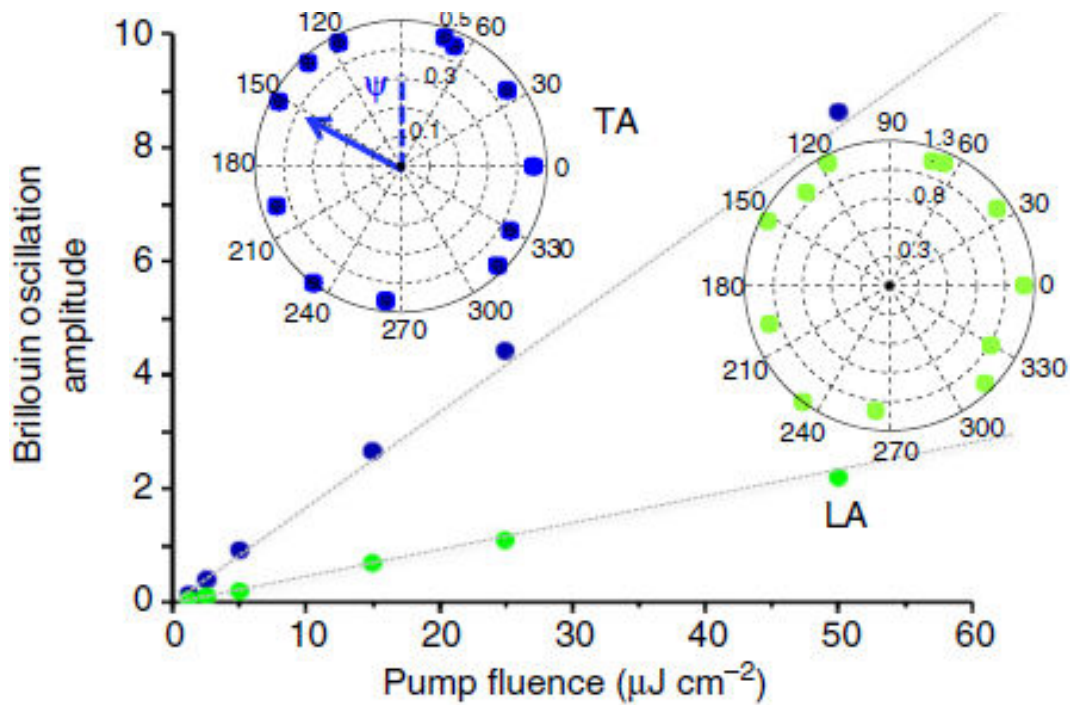


Fig. 3.30. Dependence of LA and TA mode amplitude versus fluence of pump pulse. Insets show lack of significant dependence of detected amplitude versus pump beam polarization for both modes. Figure adapted from [60].

Probe effect on acoustic detection – probe wavelength and polarization dependence

As a preliminary information, it is important to remind that photoelastic coefficients of BFO are currently unknown up to our best knowledge. Therefore, in the following we present a parametric study where the effect of variable probe wavelength and variable polarization is examined.

The wavelength dependence was carried on the grain 2 (such measurement is very time consuming because it requires to tune and stabilize probe beam from OPO each time and to adjust all the power). Quite big spread of measured amplitudes (depicted by vertical error bar in Fig. 3.31) can be also observed which is mainly caused by the fluctuation of probe intensity at different wavelengths. For both acoustic modes general tendency of increase in detected amplitude with decreasing probe wavelength can be observed. It can be connected with increasing sensitivity of acoustic strain detection with probe beam energy approaching some interband transitions [63]. No matter what is exact mechanism of better detection of Brillouin amplitude, it happens for both modes as it can be clearly noticed after normalization of LA and TA mode. Therefore observation of much higher amplitude of shear mode cannot be explained by wavelength enhancement of shear detection.

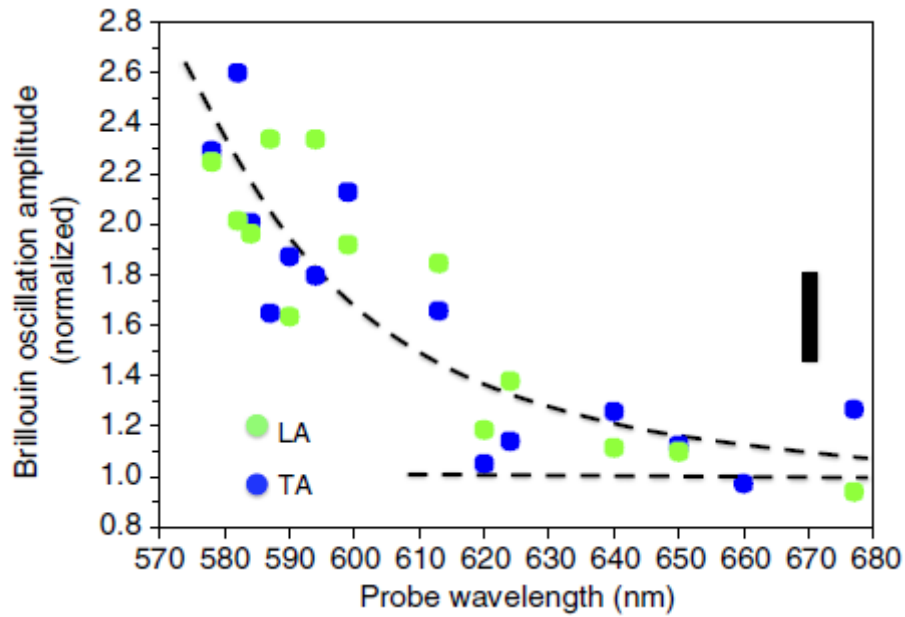


Fig. 3.31. Dependence of Brillouin amplitude (normalized for both acoustic modes at highest probe wavelength) versus probe wavelength. Figure adapted from [60].

Linear probe polarization effect has been studied for different grains exhibiting different orientations. Grain 6, whose Brillouin FFT signal was previously shown in Fig. 3.29 has been analyzed in details. It was found for this grain that sensitivity of detection of both LA and stronger TA mode could be enhanced simultaneously by rotation of probe polarization as shown in Fig. 3.32-3.34. Whatever the polarization angle, the lower frequency TA mode shows always the larger amplitude regarding to that of the LA mode.

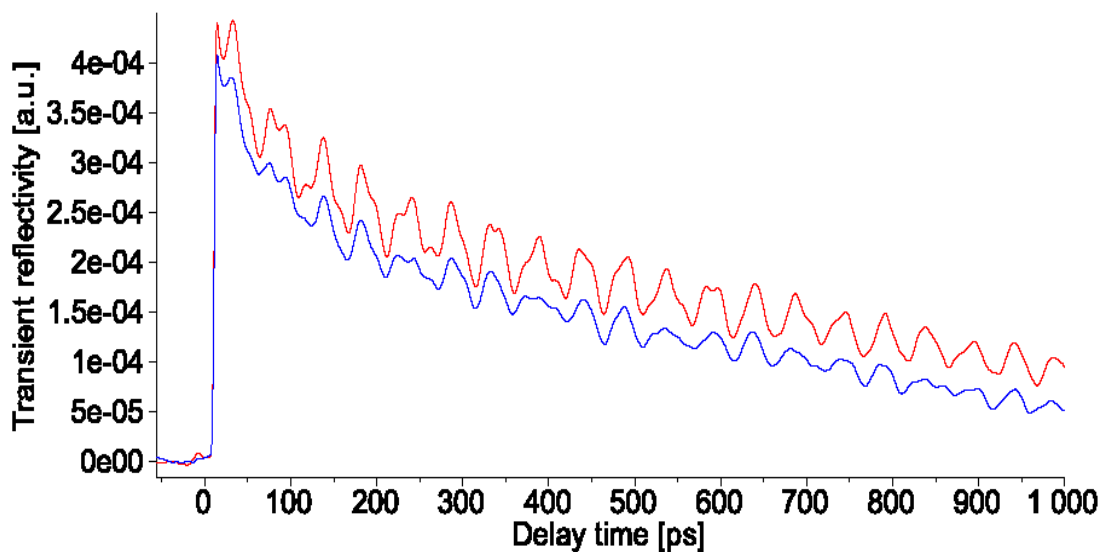


Fig. 3.32. Comparison of two signals obtained by exactly the same excitation with probe beam rotated by 60 degrees.

As an example, a comparison between two signals obtained by a probe beam with polarization rotated by 60 degrees shows that the direction of probe polarization plays an important role in the sensitivity of detection of Brillouin oscillations. There is a clearly visible component of Brillouin oscillations corresponding to the shear mode with a much smaller contribution from the LA mode.

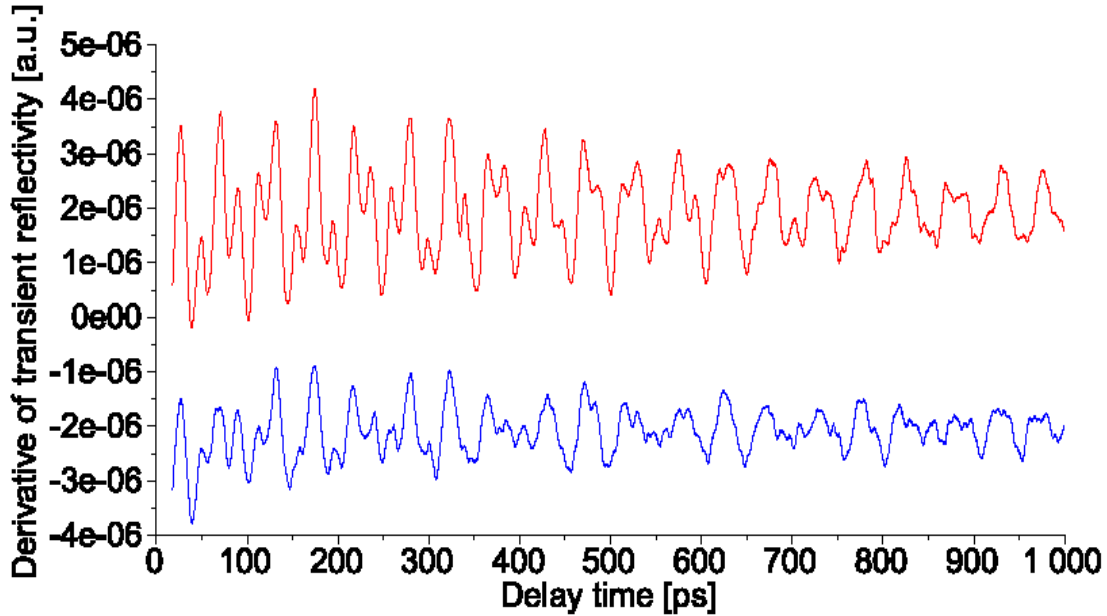


Fig. 3.33. Comparison of transient reflectivity derivatives obtained by different probe polarizations revealing a difference in the detection of Brillouin oscillations.

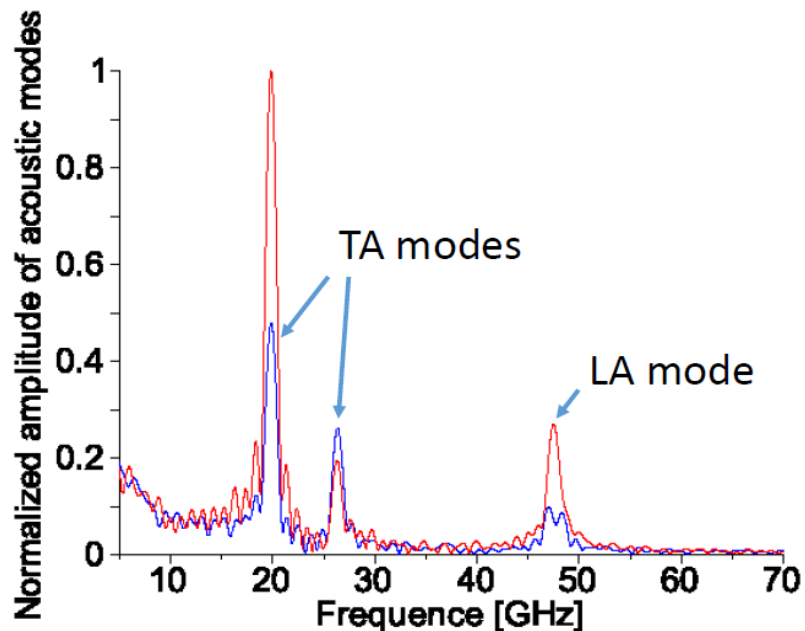


Fig. 3.34. Comparison of FFTs of signals obtained by rotated probe polarization (grain 6).

The amplitude of the TA mode having the lowest frequency and that of the LA mode have been extracted in details and are plotted versus the probe polarization dependence in Fig.3.35.

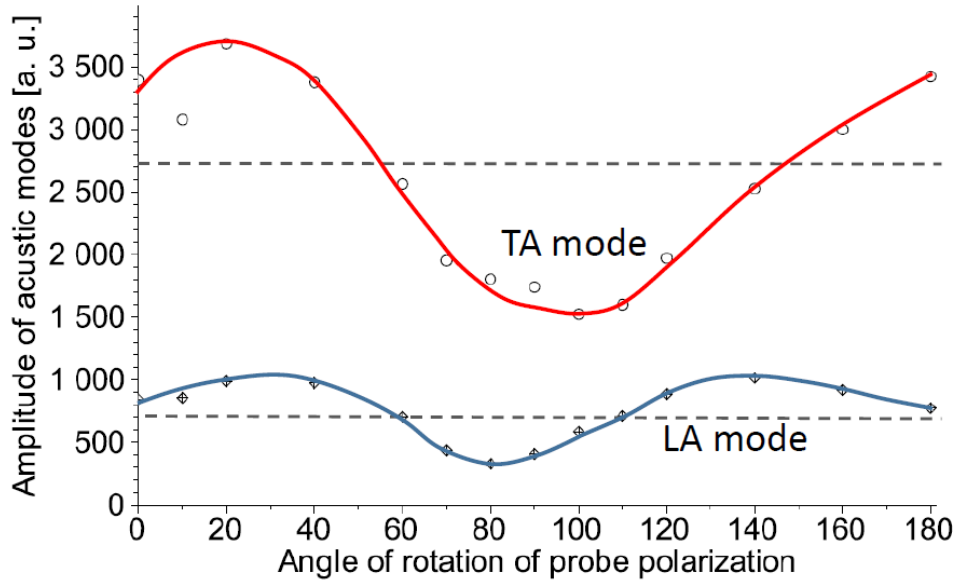


Fig. 3.35. Probe polarization dependence of detected amplitude of acoustic modes. Horizontal lines are installed as guidelines for average value of amplitude of modes in all range of angles.

It is visible that amplitude of stronger shear mode is higher in all range of probe angles. There are angles of probe polarization with enhanced and weakened detection. It can be also noticed that there is periodic (sinusoidal) dependence of acoustic amplitudes with probe polarization orientations. For LA mode, the study of periodicity of the amplitude is not straightforward since the birefringence is clearly visible in Fig. 3.34 (see FFT curve in blue). In that case, it is not possible, sometimes, to give only one value of the LA mode amplitude since we can evidence two modes.

It was found another grain (grain 7 with $\theta \cong 27$) for which amplitude of detected modes changed even more drastically with orientation of probe polarization. It was possible to find polarizations for which detection of TA mode nearly vanished and LA mode dominated as well as polarization for which amplitude of detected shear mode was higher than longitudinal one. On the blue plot presented in fig. 3.36 detection of LA mode clearly dominates. On the other hand, for another probe polarization the red plot indicates that shear modes becomes predominant while the LA mode is weakened.

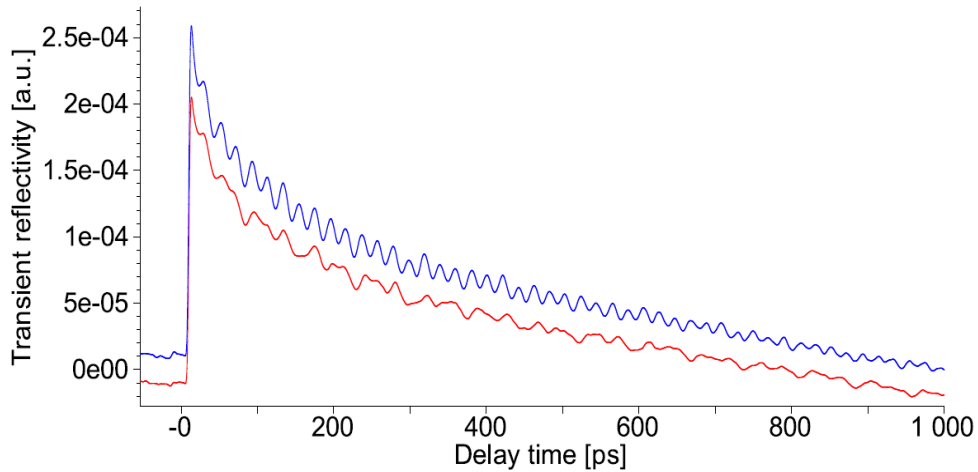


Fig. 3.36. Comparison of signals obtained by probe polarization rotated by 90 degrees. It is directly visible either enhancement of LA mode or TA mode.

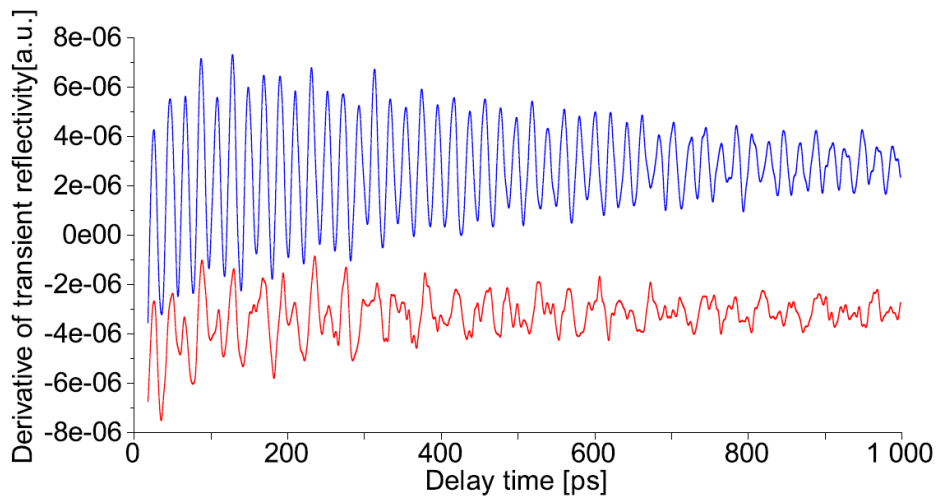


Fig. 3.37. Comparison of derivatives of signals obtained by probe rotated by 90 degrees.

Brillouin oscillations are more clearly visible on plots showing comparison of derivatives where the difference in detected signals is striking (Fig. 3.37). To show directly these differences in acoustic spectra, FFTs are shown in Fig. 3.38. On plot showing comparisons of FFTs, it is clearly visible that for one probe polarization state LA mode dominates over TA mode. Rotation of probe polarization by 90 degrees can inverse this trend in detection. Detected amplitude of LA mode was decreased several times, whereas detected amplitude of TA mode increased about 2 times making it stronger. To get full influence of probe polarization on detection, the amplitudes have been plotted versus probe polarization and shown in Fig. 3.39.

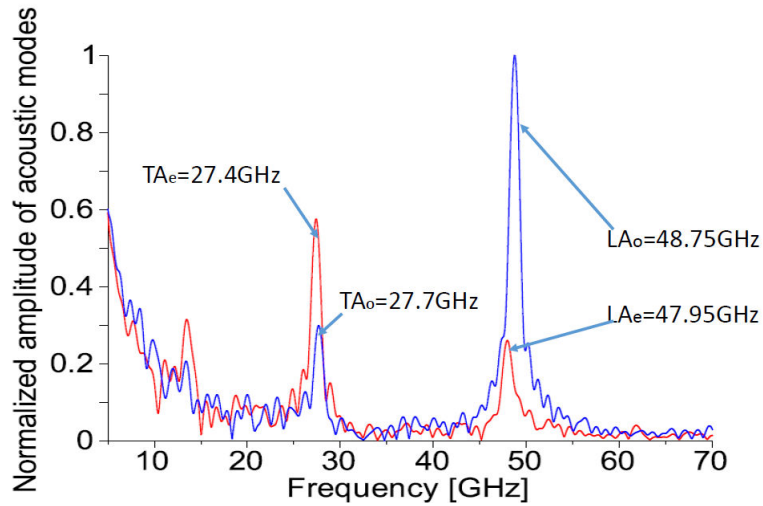


Fig. 3.38. Comparison of FFTs of signals obtained by probe polarization rotated by 90 degrees (grain 7). The shift of the Brillouin frequency of the LA mode is a clear indication of the birefringence effect which allows us to determine the grain orientation.

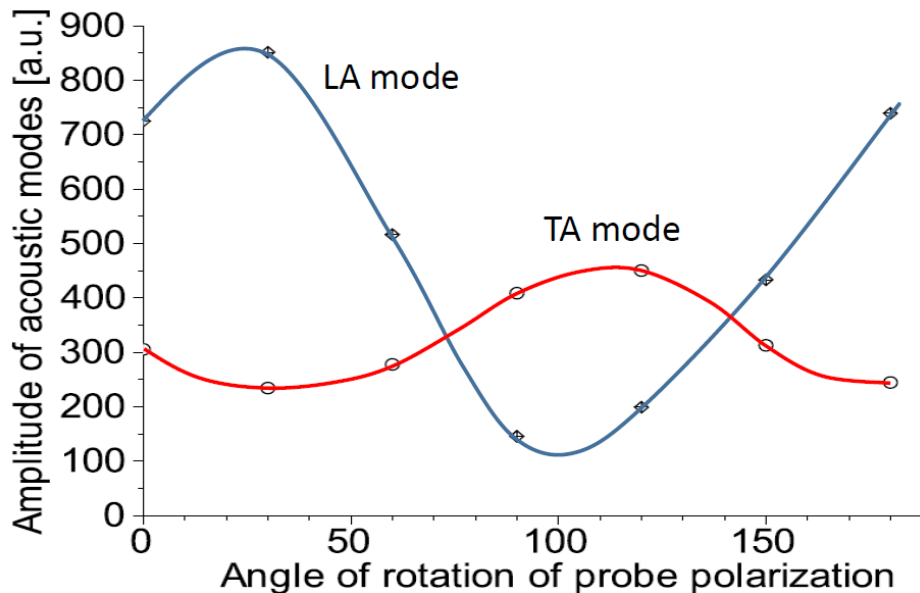


Fig. 3.39. Dependence of amplitude of LA and TA mode versus orientation of probe polarization.

On the plot there is a visible periodic dependence of amplitudes of both modes versus orientation of probe polarization. There can be distinguished ranges of probe polarization for which LA mode is detected with higher sensitivity than TA mode and vice versa. It shows that manipulation of probe polarization can enhance detection of desired acoustic mode. At that time, because the photoelastic tensor is unknown unfortunately, we can only say that the π periodic dependence is a consistent result with the crystal rotation.

The probe polarization dependence was also investigated for grain 2, that grain exhibiting a very large TA mode (see Figs. 3.26(a) and 3.26(b)). Accurate probe polarization measurements are shown in Figs. 3.40-3.42. Different effects are revealed. First of all, a shift of the detected Brillouin frequency for both TA and LA modes due to the optical

birefringence is observed (grain orientation of $\theta=24^\circ$). Comparison of signals obtained for variable selected probe polarizations reveals very subtle effect on the frequency of detected shear mode at shown in the FFT in Fig. 3.42.

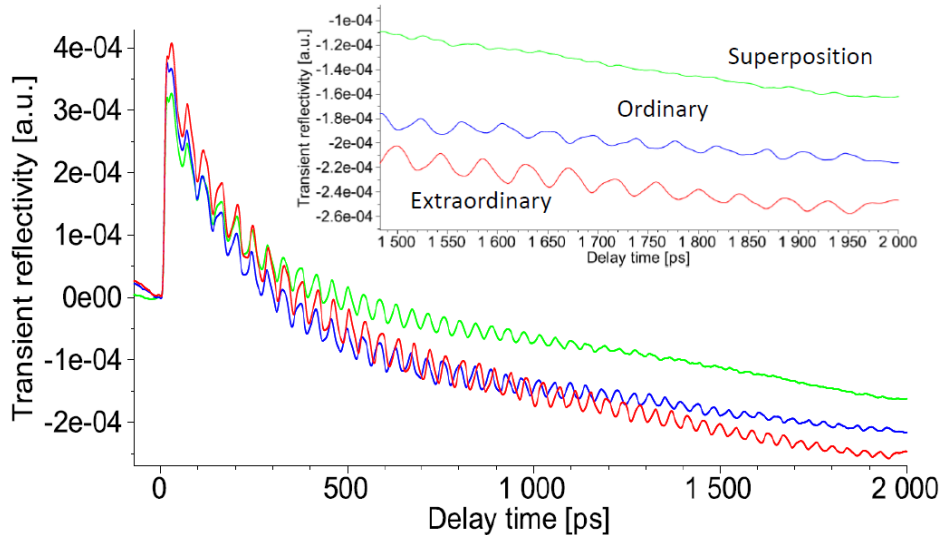


Fig. 3.40. Signals with strong detection of shear mode for different selected probe polarizations. Inset shows magnified Brillouin oscillation in the late times.

More importantly, all signals show a large TA mode that always dominates the transient optical reflectivity signal as indicated in Fig. 3.40, 3.41. Even if the TA mode dominates, it is possible to reveal the LA mode on the derivative signals with the expected Brillouin splitting revealed for mixed detection involving ordinary and extraordinary light (Fig. 3.42).

Signals marked by blue and red colours reveal small dephasing caused by slightly different frequency of oscillations (due to birefringence). On the zoom of the signal at long time scale (1500ps) phases of oscillations are opposite, leading to a vanishing signal (this is the expected nodal point that we observed for LA oscillation for grain 5 shown in Fig. 3.27).

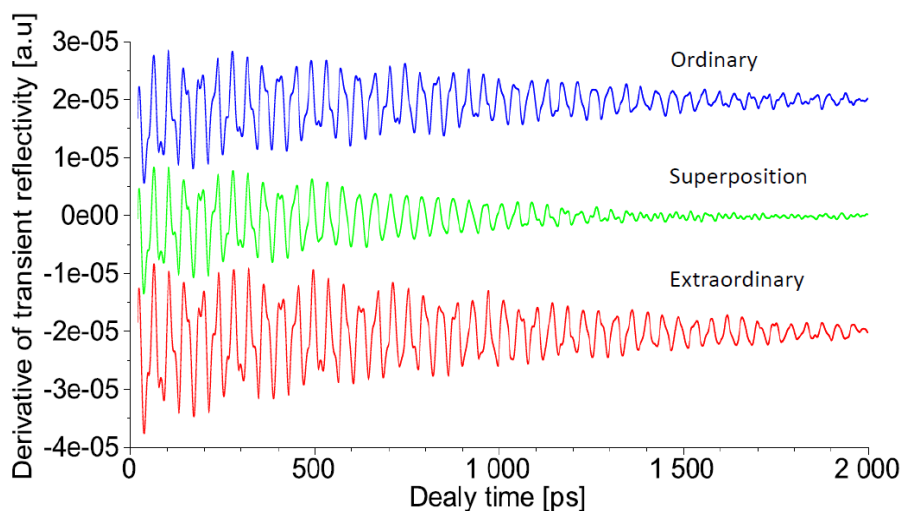


Fig. 3.41. Comparison of derivatives of signals with strong signature of shear mode.

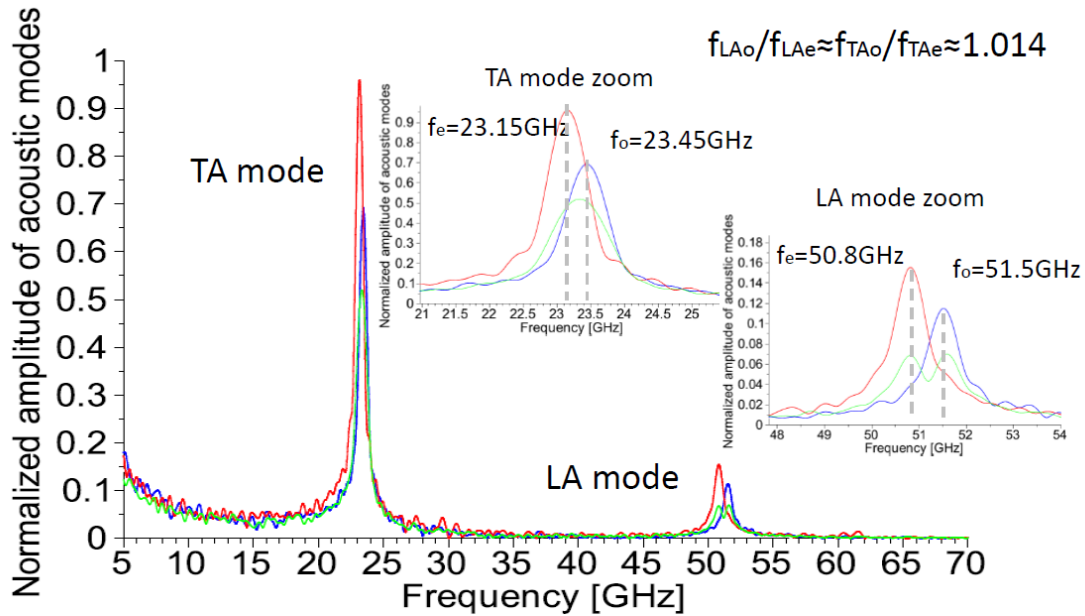


Fig. 3.42. FFTs of signals obtained by extraordinary probe (red), ordinary (blue) and superposition (green). In the insets there are magnified modes with read off values of frequencies. The ratio f_{LAo}/f_{LAe} is useful to extract the grain orientation (see appendix 2).

It is remarkable that even when the detection is achieved with either ordinary or extraordinary probe light, the detected TA mode has always a larger amplitude than that of the LA mode. Surprisingly, the ratio of these TA/LA amplitudes is nearly constant as a function of the probe polarization angle (Fig. 3.43).

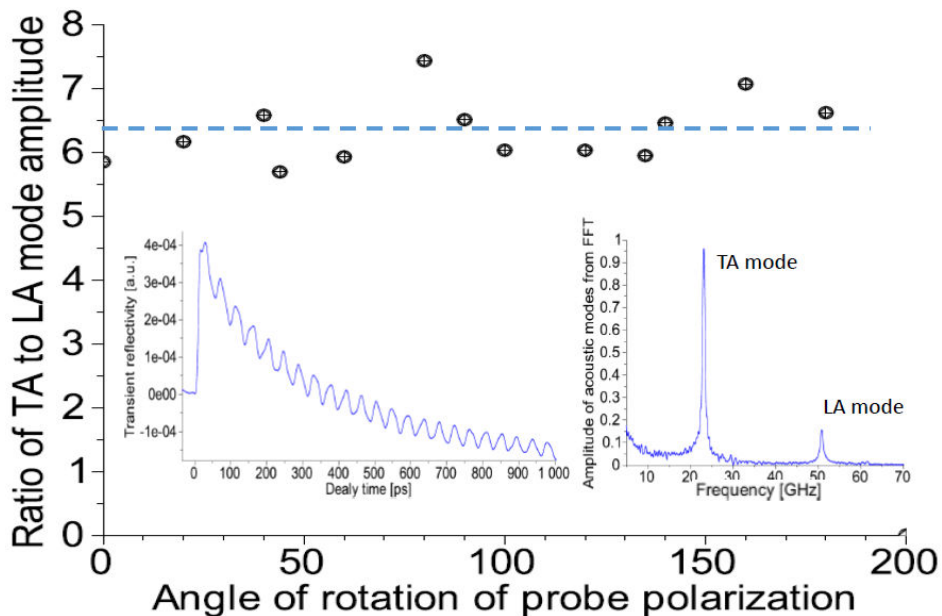


Fig. 3.43. Ratio of amplitude of TA mode to LA mode versus orientation of probe polarization (grain 2, $\theta \approx 24^\circ$). In the inset on the left typical signal for arbitrary probe polarization and on the right FFT of the signal (acoustic spectrum).

Our results obtained for a set of BFO grains with different orientations underlines that the probe polarization is a very important parameter in the detection process of both LA and TA modes in optically anisotropic media. It was revealed that different probe polarizations can either enhance or diminish detection of acoustic modes. Even if we can determine the orientation of nearly each grain we analysed, too many photoelastic parameters are unknown to establish, by now, some quantitative theory. Nevertheless, in the next chapter, and for a particular grain orientation (that of grain 5, $\theta \cong 90^\circ$, *i.e.* optical axis in plane of the irradiated surface), we can go deeper in the investigation about the photoelastic interaction in such highly birefringent ferroelectric material like BFO, and some comparisons with another ferroelectric material (LiNbO₃, LNO) will be given. Before that, in the next part, we establish a model to start a semi-quantitative discussion on the photogeneration processes of LA-TA modes in BFO.

3.3.2.3. Discussion

The study of GHz acoustic phonon generation dependence as a function of different parameters of the pump beam can give insight into ultrafast mechanisms of generation. Here our discussion is focused on the generation processes of coherent LA and TA modes in BFO based on our previous observations. We have shown that the detection effect and in particular the probe polarization dependence affects sometimes a lot the acoustic spectrum. Because we currently do not know the photoelastic tensor, the full separation of the detection and generation mechanisms is not directly possible. Nevertheless, we have shown that for some grains (grain 2, see Fig. 3.26), whatever the probe polarization, the TA mode was always much larger in amplitude than that of the LA mode. As already noticed, this situation is remarkable and has never been observed before (see Table 3.2). The absence of TA mode for a grain with the optical axis in plane (grain 5, Fig. 3.27) is also a particular case that provides rich informations. As we will show below, we believe that this peculiar property comes from a driving inverse-piezoelectric effect.

First of all, we did not observe a dependence of generated acoustic amplitude versus pump polarization dependence indicating that electrostriction mechanism can be ruled out as dominating process (Fig.3.30). Electrostriction is property of dielectrics that forces them to change their shapes under application of electric field (see part 2.3.4). This mechanism is caused by a slight displacement of ions in the crystal lattice upon light electric field (polarization). Secondly, acoustic phonons generation by thermal expansion (thermoelastic stress, see 2.3.1) upon laser excitation was also ruled out on the basis of a time resolved X-ray diffraction measurements (TRXRD) [54, 55] showing that the light-induced strain (expansion) was much bigger than the strain observed upon thermal expansion at thermodynamic equilibrium. It was also shown that for a pump wavelength of 3.1eV, and a BFO band gap of 2.8eV, the excess energy (0.3eV, typically 10%) leads only to a modest lattice heating coming from intraband relaxations processes [55]. Moreover the lifetime of photoexcited carriers is pretty long in BFO (ns), preventing interband relaxation process and, when it happens, it was also shown that radiative recombination dominates in case of BFO

reducing then the thermoelastic effect [49]. Deformation potential mechanism was also excluded for the generation of LA mode since the isotropic deformation potential parameter $\frac{\partial E_g}{\partial P_r}$ is negative [56] and should lead to light-induced contraction while clearly light-induced expansion of the unit cell was reported by TRXRD measurements [54,55].

Despite these arguments, it appears that finally the electronic origin (deformation potential) and the inverse-piezoelectric effect are two processes usually discussed [54,55]. It is then necessary to make an estimate of both processes to fix some orders.

As photoexcited carriers have much longer lifetime (order of 1ns) than time of acoustic generation (order of 1ps), it can be assumed that the deformation potential parameter is established by out-of-equilibrium carriers accumulated at the bottom and top of the conduction and valence band respectively. Therefore, averaged value of the photo-induced longitudinal deformation potential parameter is equal to direct band gap (E_g) derivative with respect to pressure (P_r) and estimated value is $\frac{\partial E_g}{\partial P_r} \sim -5 \times 10^{-11} eV Pa^{-1}$ as obtained from pressure dependence of direct band gap of BFO [56]. This value is twice smaller than that of typical semiconductor GaAs. Knowing concentration of photo-excited carriers ($N \sim 5 \times 10^{18} - 5 \times 10^{19} \text{ cm}^{-3}$) and using bulk modulus of BFO ($B \sim 80 \text{ GPa}$) [64], longitudinal deformation potential stress can be estimated $\sigma_{DP}^L = -N \frac{\partial E_g}{\partial P_r} B \sim 0.2 \times 10^7 - 2 \times 10^7 Pa$. This estimation can be compared with stress induced by inverse piezoelectric effect. For photo-excited carriers accelerated by internal electric field originated from spontaneous polarization, there is partial screening of polarization field by photo-induced charges. In the simplest case, capacitor model can be considered for which internal electric field is expressed by basic formula $E = eN_s / \epsilon \epsilon_0$, where N_s is the surface density of photo-excited carriers, e is the elementary electric charge, ϵ_0 is vacuum permittivity, and ϵ is bulk BFO dielectric constant ($\epsilon \sim 45$) [65]. Fluence of exciting pump pulse used in experiment was in range $10-100 \mu J cm^{-2}$. Based on this and assuming that every pump photon excites one electron over the band gap which after can move freely in the local electric field, induced change of surface density of charge can be estimated to $N_s = 2 \times 10^{13} - 2 \times 10^{14} \text{ cm}^{-2}$. This gives huge photo-induced electric field of the order $E \sim 100-1000 \text{ kV cm}^{-1}$ (up to 1 MV cm^{-1} !) and in consequence leads to an inverse piezoelectric stress. This stress can be estimated using averaged value of piezoelectric coefficient $\bar{e} \sim 3 \text{ Cm}^{-2}$ based on known values $e_{33} \sim 2-4 \text{ Cm}^{-2}$ [66] and $e_{31} \sim -2.8 \text{ Cm}^{-2}$ [67]. Inverse piezoelectric stress can be estimated as $\sigma_{PE} = \bar{e} E \sim 3 \times 10^7 - 3 \times 10^8 Pa$. First of all it can be noticed that at the same fluences the value of inverse piezoelectric stress is at least one order time higher than the value of stress originated from deformation potential. This shows that mechanism of acoustic generation by inverse piezoeffect is potentially dominating over deformation potential mechanism. What is more, similar absolute value of piezoelectric coefficient e_{31} as of coefficient e_{33} indicates that shear and longitudinal inverse piezoelectric stress should have the same order of magnitude ($\sigma_{PE}^T \approx \sigma_{PE}^L$). This is in contrast with deformation potential stress for which the shear deformation potential stress exists, for the rhombohedral symmetry, only for broken symmetry (since the volume deformation

potential tensor is diagonal with elements a_{xx} , a_{yy} , a_{zz}). For that the shear deformation potential stress is proportional to the difference $a_{xx}-a_{zz}$ [9, 61]. On the basis of these elements, we show that the generation of coherent acoustic phonons is likely to be driven by the photo-induced inverse piezoelectric effect. We admit that this is not a full demonstration but the following model provides additional support to our claims.

This model is based on a theoretical calculation of inverse-piezoelectric stress that takes into account different grain orientations. For that we make use of the inverse piezoelectric tensor (see Eq. 2.11).

Among the different grains we have investigated (see part 3.2), we have observed that the largest shear mode amplitude is observed for grains where only one TA amplitude is observed (i.e. grain 2, $\theta=24^\circ$, Figs. 3.26, 3.42). Based on symmetry reasons, the existence of only one TA mode indicates that coherent phonons propagate along direction lying into Oyz symmetry plane, so this plane must be perpendicular to the illuminated surface. We have selected this grain to discuss more quantitatively the experimental results as well as the grain 5 ($\theta=90^\circ$) as a limit case. For plane exhibiting the Oyz crystallographic plane perpendicular to the irradiated surface (Fig. 3.44), it is possible with use of tensorial calculations within 3m point group to obtain simple formulas with only one parameter which is θ . In particular we can obtain the angular dependence of generated shear and longitudinal stress originated from inverse piezoelectric effect.

The stress tensor describing the inverse piezoelectric effect, in the tensorial contracted form, allows to establish the expression for some selected grain orientation [17].

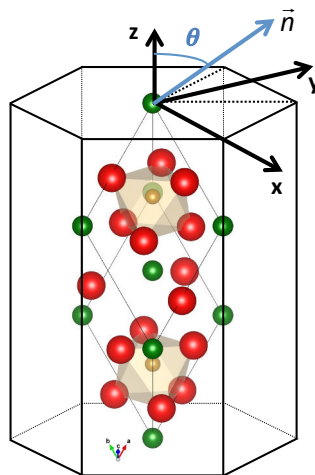


Figure 3.44: BFO crystallographic structure with the hexagonal frame adopted to perform the tensorial calculation of the inverse piezoelectric effect. The vector \mathbf{n} defines the orientation of the surface of the grain.

According to the coordinates frame (x,y,z) shown in Fig. 3.44, the internal ferroelectric polarization is along z axis, i.e. $\mathbf{E}=E_3 \mathbf{z}$. Then, the tensor in case of the 3m point group has the following matrix form:

$$\begin{bmatrix} 0 & 0 & 0 & 0 & e_{15} & -e_{22} \\ -e_{22} & e_{22} & 0 & e_{15} & 0 & 0 \\ e_{31} & e_{31} & e_{33} & 0 & 0 & 0 \end{bmatrix} \quad \text{Eq. 3.9}$$

So finally the inverse piezoelectric stress matrix becomes

$$M(\sigma) = \begin{bmatrix} \sigma_1 & \sigma_6 & \sigma_6 \\ \sigma_6 & \sigma_2 & \sigma_4 \\ \sigma_6 & \sigma_4 & \sigma_3 \end{bmatrix} = \begin{bmatrix} \varepsilon_{31}E_3 & 0 & 0 \\ 0 & \varepsilon_{31}E_3 & 0 \\ 0 & 0 & \varepsilon_{33}E_3 \end{bmatrix} \quad \text{Eq. 3.10}$$

Inverse piezo-electric stress for the grain 2 (ferroelectric polarization inclined relative to the surface of the grain)

In the case of grain 2 (Figs. 3.26, 3.42), acoustic phonons propagate within the Oyz plane. Even, if the grain 2 has an orientation estimated at $\theta=24^\circ$, we will establish the general calculation. The stress tensor in the matrix form $M(\sigma')$ in the new coordinates frame (x',y',z') is obtained by applying a rotation around the Ox axis using the classical basis change method ($M(\sigma')=T.\sigma.T^t$). T is the basis change matrix:

$$T = \begin{bmatrix} 1 & 0 & 0 \\ 0 & \cos(\theta) & -\sin(\theta) \\ 0 & \sin(\theta) & \cos(\theta) \end{bmatrix} \quad \text{Eq. 3.11}$$

Finally we obtain:

$$M(\sigma') = \begin{bmatrix} \varepsilon_{31}E_3 & 0 & 0 \\ 0 & (\varepsilon_{31}\cos^2(\theta) + \varepsilon_{33}\sin^2(\theta))E_3 & (\varepsilon_{31} - \varepsilon_{33})\sin(\theta)\cos(\theta)E_3 \\ 0 & (\varepsilon_{31} - \varepsilon_{33})\sin(\theta)\cos(\theta)E_3 & (\varepsilon_{31}\sin^2(\theta) + \varepsilon_{33}\cos^2(\theta))E_3 \end{bmatrix} \quad \text{Eq. 3.12}$$

In our experimental configuration, in the absence of sharp focusing of pump laser radiation, the gradients of the photo-induced stresses along the surface are negligible, so the transverse and the longitudinal acoustic waves are emitted because of the gradients of the stress along the z' direction defined as $\frac{\partial \sigma'_{iz'}}{\partial z'}$, where $i=y'$ for a quasi-shear acoustic wave and $i=z'$ for a dominant contribution into quasi-longitudinal acoustic wave. So from the above tensor, the final piezoelectric transverse and longitudinal stress components are given by:

$$\sigma_T = E_3(e_{31} - e_{33})\sin(\theta)\cos(\theta) \quad \text{Eq. 3.13}$$

$$\sigma_L = E_3(e_{31}\sin^2(\theta) + e_{33}\cos^2(\theta)) \quad \text{Eq. 3.14}$$

By simple analyze of equation 3.13 it can be observed first that as both piezoelectric coefficients have opposite signs [66, 67], their values add effectively, what can explain enhanced shear stress. On the opposite, one can observe a competition between the two components in Eq. 3.14 for the longitudinal stress. Consequently, the smaller LA amplitude could come from this effect. For the angle of $\theta=24^\circ$, the maximum value of σ_T/σ_L is found to be around 2 which is 3 times smaller than the value found experimentally (see Fig. 3.43). The role of the detection might be important too, if the proposed model is correct.

Inverse piezo-electric stress for the grain 5 (ferroelectric polarization parallel to the surface of the grain)

In the case of the grain 5 (Fig. 3.27, $\theta=90^\circ$), the stress tensor is obtained by the same method. As soon as the z axis (ferroelectric polarization) is parallel to the surface, and whatever the surface orientation, the stress tensor is always diagonal. For example, for a surface normal \mathbf{n} oriented along y axis, we have in the basis (x',y',z') (z' corresponds for example to the previous y axis) :

$$M(\sigma') = \begin{bmatrix} \varepsilon_{31}E_3 & 0 & 0 \\ 0 & \varepsilon_{33}E_3 & 0 \\ 0 & 0 & \varepsilon_{31}E_3 \end{bmatrix} \quad \text{Eq. 3.15}$$

If now, a rotation is done around y' , we obtain the general expression of the stress tensor for any plane parallel to z axis (parallel to the ferroelectric polarization direction). In that case the rotation matrix by an angle ψ around y' axis is:

$$T(\psi) = \begin{bmatrix} \cos(\psi) & 0 & -\sin(\psi) \\ 0 & 1 & 0 \\ \sin(\psi) & 0 & \cos(\psi) \end{bmatrix} \quad \text{Eq. 3.16}$$

The final tensor is unchanged with

$$M(\sigma'') = \begin{bmatrix} \varepsilon_{31}E_3 & 0 & 0 \\ 0 & \varepsilon_{33}E_3 & 0 \\ 0 & 0 & \varepsilon_{31}E_3 \end{bmatrix} \quad \text{Eq. 3.17}$$

For this family of planes, it is then shown that no off diagonal terms appear. This means that no shear component exists. Consequently, this indicates that the inverse piezoelectric effect cannot lead to the emission of TA mode for such family of grain as observed in Fig. 3.27 (i.e. grain 5). This is an additional indication of the relevance of the inverse piezoelectric effect as a driving mechanism of coherent source of shear waves.

Following the Eq. 3.13 and 3.14, it can be noticed that the highest amplitude of shear stress should be generated for grain with crystallographic z -axis oriented at 45° versus surface normal for this class of grain (Oyz plane perpendicular to the surface). Experimentally, we

did not find such a grain unfortunately according to our analysis. If good single crystals would be available in the future, it would be then interesting to test this expectation.

As a final point of analysis, we would like to discuss the distribution of photoexcited carriers. Even if the theoretical ratio of shear to longitudinal stress is independent on the internal electric field (Eq. 3.13 and 3.14), it is worth to come back to the estimate of this electric field. It should be taken into consideration that the previous estimates are based on the simplified capacitor model and on assumption that excited electrons can move freely through the entire excited volume. Moreover we have considered that these hot electrons and holes concentrate separately on two virtual electrodes (we currently do not know the domain structure in the BFO polycrystalline grain but we can assume that the domain size follows the Kittel law and, for most of grains, has a diameter of typically 1-3 μm [68]). This assumption leads to an estimation of very large electric field even for quite moderate pump fluence (1MV/cm). In the case of localized photoexcited carriers as suggested by transient photoabsorption and photocurrent measurements [50] and by TRXRD studies [55] it would be necessary to modify the model considering some possible trapping. For example a sequence of different capacitors in the region of skin depth with excited charges distribution following the absorption profile could be imagined (Fig. 3.45). This would lead to quasicontinuous sequence of capacitors with a smaller induced internal electric field which would additionally decrease exponentially with depth. Size of BFO unit cell is several angstroms, whereas absorption skin depth is several tens of nanometers (about 50-60 nm in the case of pump wavelength of 400nm, see part 3.3.2.1) so it is reasonable to assume that in the limit case, charges are localized in few unit cells. To give an order, if we consider that this trapping distance (“capacitor thickness”) is about 10 times shorter than skin depth d of absorption ($l \approx \frac{d}{10}$). We can show then that this decreases the “sheet” density of carriers on the virtual electrode. With a density of absorbed energy expressed by following formula $\rho_a(x) = \frac{I_0}{d} e^{-\frac{x}{d}}$, where I_0 is the initial intensity of pump pulse equivalent to fluence of pump light and d is skin depth of absorbed light, we show that the intensity of absorbed light in the first assumed region of charge localization close to surface is:

$$I_a \left(l = \frac{d}{10} \right) = \int_0^l \rho_a(x) dx = \frac{I_0}{d} \int_0^l e^{-\frac{x}{d}} dx \approx \frac{1}{10} I_0 \quad \text{Eq. 3.18}$$

Based on this estimation it can be noticed that in the first one tenth of skin depth distance adjacent to the surface, about one tenth of incident intensity of exciting light is absorbed. Therefore for this model based on localized charge, corresponding electric field and stress close to surface is about one order times smaller than for simple capacitor model based on free charge. So finally one order times smaller than previously estimated values of electric field close to sample surface seems to be more realistic. This simplistic model could explain lack of observation of saturation of strain (or saturation of LA/TA mode amplitudes, Fig. 3.30) at high pump fluence which is a phenomenon that is still not understood [54,55,60]. In

that case the photoinduced carriers sheet density becomes around 10 times smaller than that estimated at a domain wall (P/e). According to previous calculations at fluence about $3\text{mJ}\cdot\text{cm}^{-2}$, amount of light absorbed in region adjacent to surface should be enough to saturate totally and compensate surface density of charge originated from spontaneous polarization $N_S \sim P/e \sim 6 \times 10^{14} \text{cm}^{-2}$. Fluence leading to such effect should be expected as damage threshold leading to degradation of sample surface.

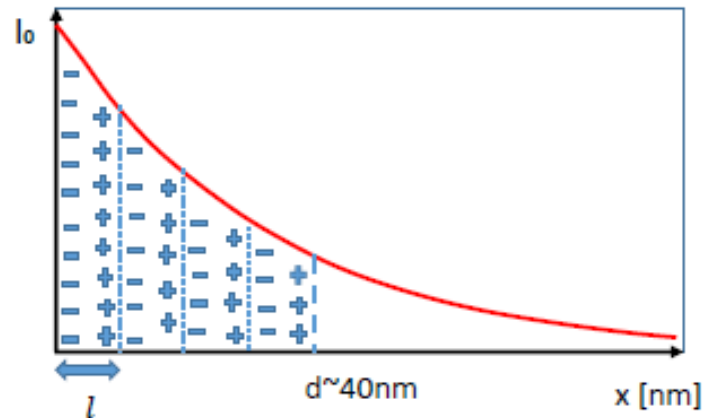


Fig. 3.45. Scheme of depth profile of absorbed exciting light with visualized four zones with localized charge in the range of skin depth.

3.4. Results: Role of magnetic ordering on the photogeneration and photodetection of coherent acoustic phonon in BFO (high temperature investigation)

We have previously evidenced original photoinduced shear strain, i.e. shear coherent acoustic phonons in BFO. We have assigned this peculiar property as a possible signature of the inverse-piezoelectric effect in this ferroelectric material. It would have been interesting to perform a study above the Curie temperature to see if these light-induced coherent phonons dynamics is deeply modified or not by the ferroelectric order. But we do not have the equipment for such high temperature, unfortunately. Moreover, as we will see latter on, the GHz coherent acoustic phonons would rapidly damp in this very high temperature range. Nevertheless, BFO also exhibits some magnetic ordering with a Néel temperature of around 650K (see part 2.4.3) that is accessible with our high temperature cell (Linkam). It is then worth to investigate this temperature range. Some anomalies have of course already been reported in the vicinity of Néel temperature as partially presented in part 2.4.3 (change of the activation energy in the DC electrical conductivity measurements, anomaly on the optical birefringence). In order to evaluate the impact of this magnetic ordering on the phononic properties we have then carried out pump-probe experiments from room temperature up to 873K (600°C) which is pretty rare in our community. We will show that some anomalies are reported on the lifetime of TA and LA phonons through the Néel temperature (spin-phonon coupling) but no special effect on the generation process *a priori*.

3.4.1. Experimental conditions and procedure

Experiment was done following the standard procedure, with fixed powers, wavelengths (photon energies) and polarizations of both pump and probe beams. BFO pellet was fixed to the heating oven, which was installed on support with possibility of movement in three perpendicular directions with micrometric accuracy. Therefore there was possibility to scan sample surface, adjust precisely grain position and distance from focal point of laser beams. Measurements with variable temperature on polycrystalline sample (grain size is comparable with size of laser beam in the focal point) were very difficult, mainly because of thermal expansion of the sample and sample holder. As size of the pellet is about 10mm, increase of temperature by 100°C could cause expansion of sample and shift of the grain by about 10µm, what is comparable with size of the grain. During the temperature growth, selected grain simply escaped from fixed laser field, therefore during this treatment slight adjustment of position of selected grain by micrometric screw was continuously necessary. There was following procedure: we first localized a grain with high signal to noise ratio and with a large TA signal, then we optimized the reflected light intensity by measuring the photodiode voltage. When we spanned the temperature, we optimized each time the photodiode voltage to be sure to pump and probe the grain at the same position. At high temperatures, there was high temperature gradient close to the sample surface, what caused convection and chaotic movement of adjacent air. In practice it caused local fluctuation of sample temperature close to the surface as well as refractive index of air. All this effects disturbed pump-probe measurements and made experiment very difficult and problematic in reasonable implementation. But we succeeded in. All the experiments were conducted in air. We checked the reproducibility of the signals several times.

3.4.2. Effect of temperature variation on generation and detection of acoustic phonons in ferroelectric BFO

The experiments were conducted with grain exhibiting a large TA signal compared to LA signal (i.e. typical grain 2, see Fig. 3.26, 3.42). Signals were collected for increasing (change by 50 degrees) and decreasing temperature (change by 100 degrees). First in order to see qualitatively the effect of temperature, a comparative plot of signals registered at 100°C, 300°C and 500°C is shown in Fig. 3.46.

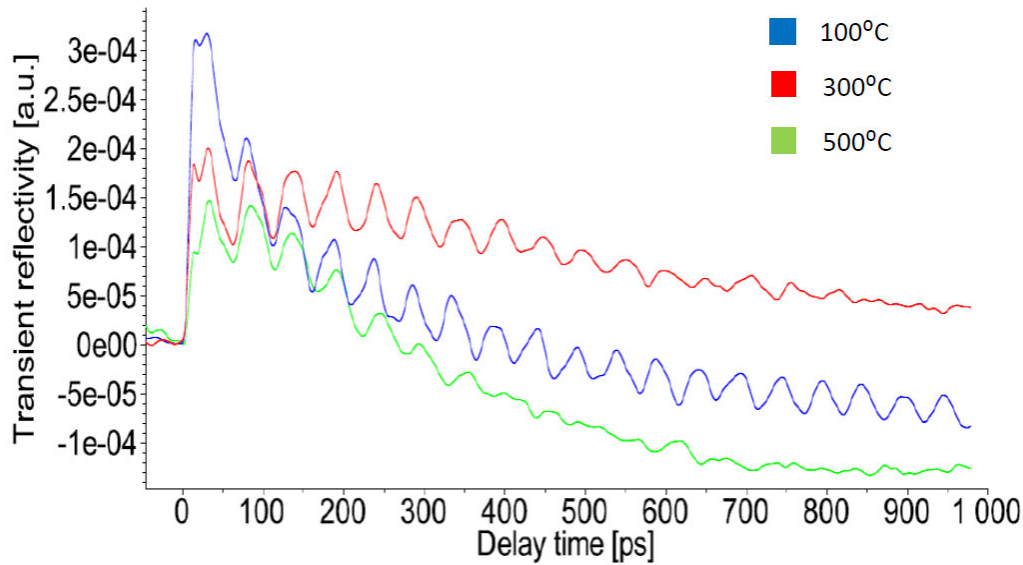


Fig. 3.46. Comparison of signals obtained on selected grain of polycrystalline BFO sample at different temperatures.

First of all, a decrease of the electronic peak magnitude with temperature can be noticed. This effect, consistent with previous observation [49], may have different origins. It could be due to a fast relaxation induced by the increase of phonons population. The temperature dependence of the BFO band gap, may also affect the generation as well as the detection process. However, we did not detect any significant change of the optical reflectivity (at the probe wavelength of 590nm) with temperature. The band gap change in this temperature range is not too large (see Fig. 2.14(b) [37]).

Concerning the acoustic part, the Brillouin oscillations characteristics exhibit a strong temperature dependence with a strong damping of the acoustic signal. To further see the influence of heating on the LA/TA acoustic spectrum, FFTs are shown in Fig. 3.47. It is directly visible that amplitude of both acoustic modes in Fourier spectra decreases with temperature as summarized in Fig. 3.48. As mentioned above, we do not believe this effect is due to an optical property effect (no change of diode voltage). The decays of amplitudes of both TA and LA mode are both linear with temperature without any anomaly. In the case of LA mode, the signal nearly vanishes to the background noise at the highest temperatures. Local fluctuations of amplitude are caused by fluctuation of pump and probe intensity within long times of signal acquisition, but also by slight grain shift caused by occasional mechanical relaxation of accumulated stress of sample. In all the temperature range, the amplitude of TA mode is significantly higher than amplitude of LA mode. This means that for such family grain, the very large TA mode is a robust property. The situation concerning the temperature dependence of the Brillouin frequencies also reveals rich information. Red shifts of Brillouin frequencies are reported for both LA and TA modes. The softening is much more pronounced for the TA mode with a relative change of around 10% (Fig. 3.49) while only a relative change of around 2.5% is observed for the LA mode (Fig. 3.50).

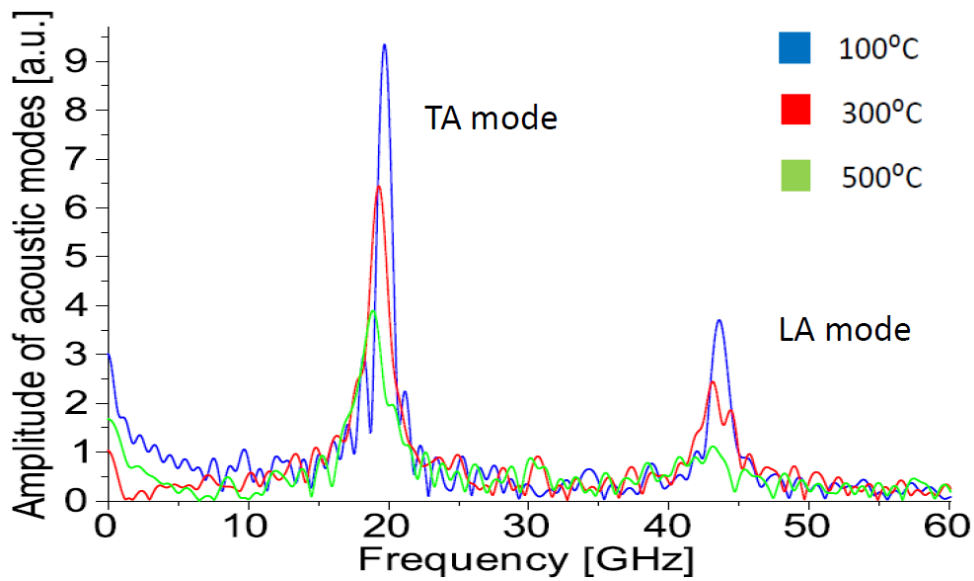


Fig. 3.47. Comparison of acoustic spectra at different temperatures.

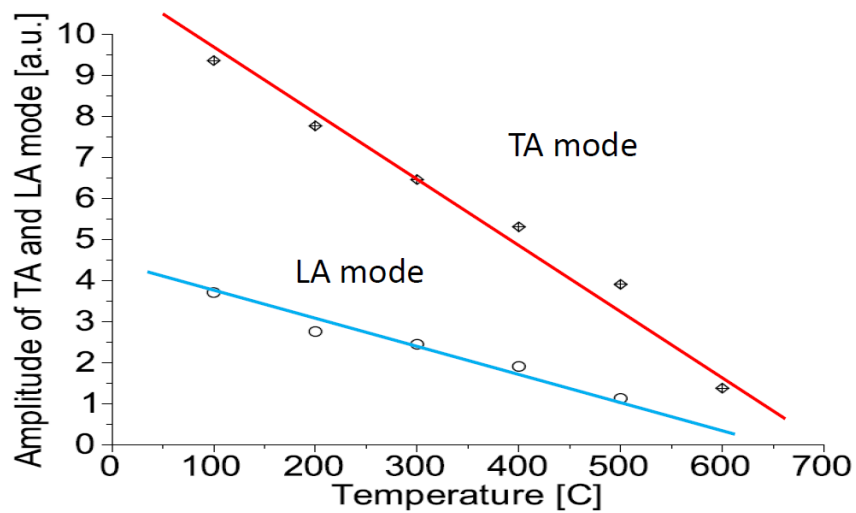


Fig. 3.48. Temperature dependence of amplitude of TA and LA modes for temperature decreasing from 600 degrees.

To see influence of heating on speed of propagation of acoustic modes, it was plotted independently Brillouin frequency of both LA and TA mode for increasing and decreasing temperature on single plot (Fig. 3.49 and 3.50). First of all, we can see the pretty good reproducibility versus temperature in the heating and cooling regime. Secondly, while the frequencies decrease linearly with temperature at low temperature, a clear departure from this regime is evidenced above the Néel temperature.

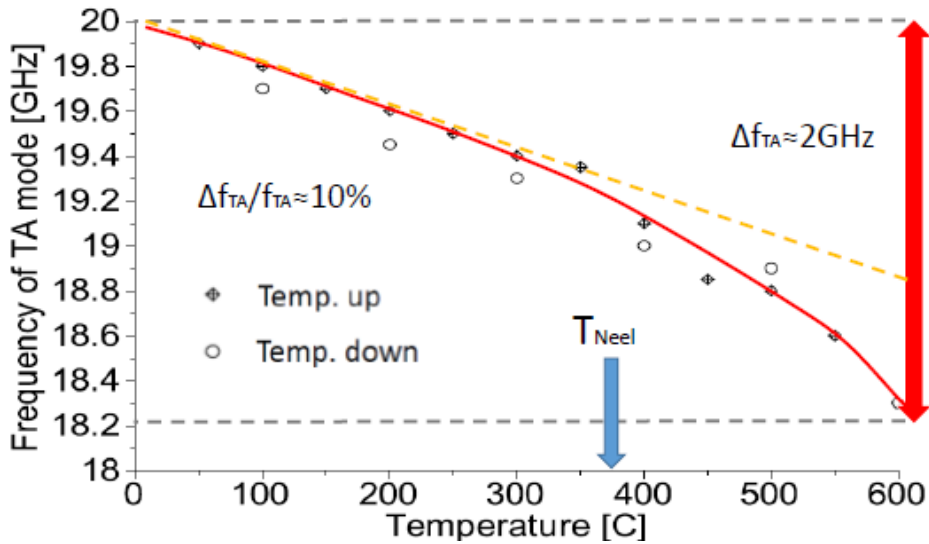


Fig. 3.49. Plot of TA mode frequency extracted from FFTs for increasing and decreasing temperatures.

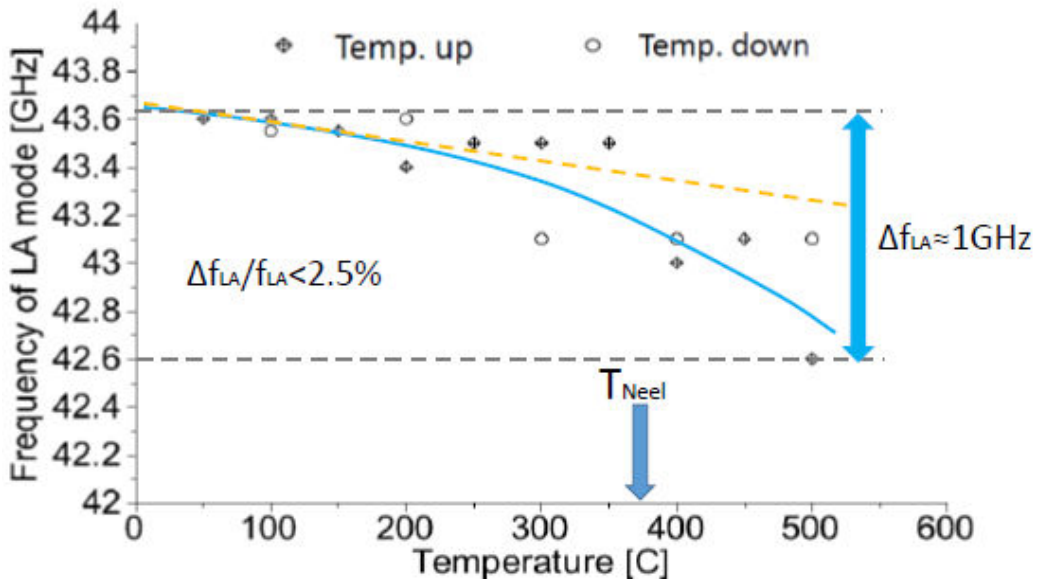


Fig. 3.50. Plot of LA mode frequency extracted from FFTs for increasing and decreasing temperatures.

The analysis of the decay of acoustic modes shown in Figs. 3.51-3.52, and 3.53 also reveals some anomalies, which are more clearly visible for the TA mode. It appears that the TA Brillouin peak width significantly increases above the Néel temperature while that of the LA mode exhibit a more smooth temperature variation. This anomaly appears within the same temperature range where an enhanced lattice anharmonicity (decrease of Brillouin frequencies) is observed as discussed before (Figs. 3.49 and 3.50).

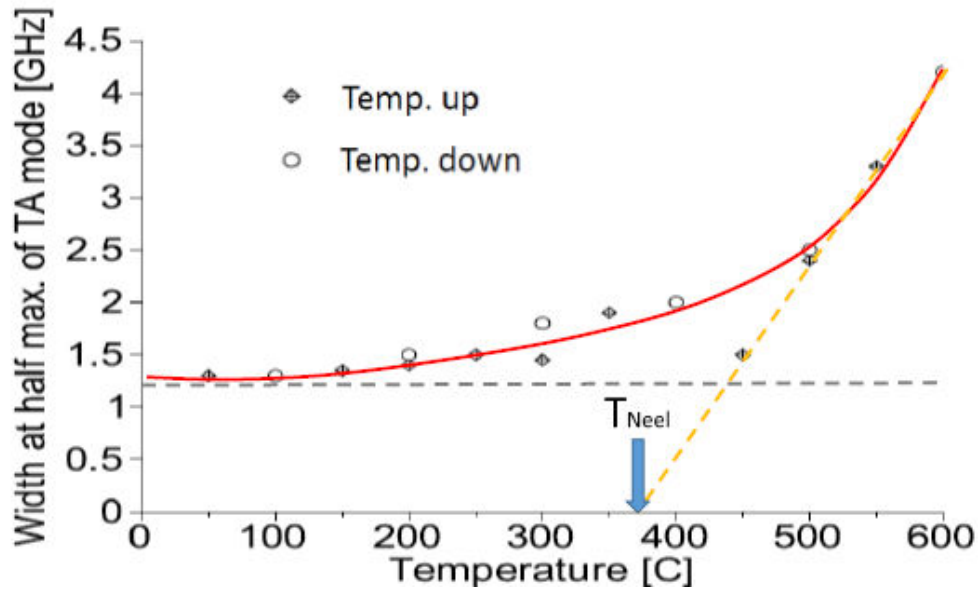


Fig. 3.51. Plot of full width at half maximum (FWHM) of TA mode versus temperature of BFO sample.

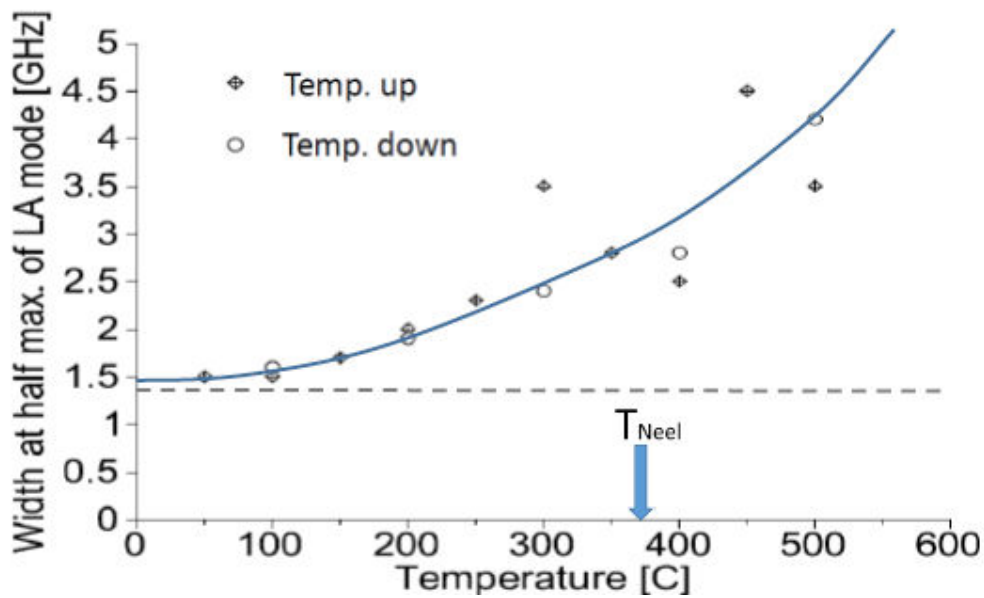


Fig. 3.52. Plot of full width at half maximum (FWHM) of LA mode versus temperature of BFO sample.

These results clearly show some anomalies in the vicinity of the Neel temperature. Since the Brillouin process is dependent on both the elastic properties (sound velocity) and the optical properties (refractive index), it is first necessary to discuss both possible contributions. In the following, we will show that the decrease of Brillouin mode frequency is mainly driven by an elastic effect (anharmonicity).

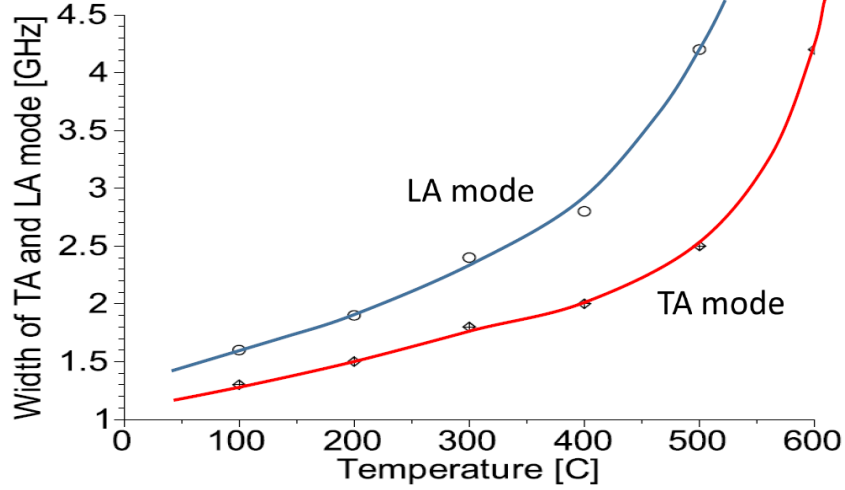


Fig. 3.53. Temperature dependence of FWHM of TA and LA modes for temperature decreasing from 600 degrees.

First of all, we have to keep in mind, that for a fixed probe geometry (wavelength, polarization), if the decrease of Brillouin frequency would have been mainly driven by a change of refractive index, then both acoustic modes should exhibit similar temperature dependence. It is clearly visible in Fig. 3.49 and 3.50 that the absolute change of frequency of LA mode is about twice smaller than that of TA mode, whereas it should be expected opposite trend as LA mode frequency is more than two times higher than frequency of TA mode. There is a slight change of the optical birefringence versus temperature that could also have a contribution but the variation remains small (see Fig. 2.14(b)). As a consequence, the origin of the “red-shift” of Brillouin frequencies comes mainly from the elastic properties. This can be formally demonstrated.

The Brillouin frequency shift can be written as a function of the relative changes of both the refractive index and the acoustic speed with:

$$\Delta f_B(n, v) = \frac{\partial f}{\partial n} \Delta n + \frac{\partial f}{\partial v} \Delta v = \frac{2}{\lambda} (v \Delta n + n \Delta v) \quad \text{Eq. 3.19}$$

If we assume that the detected change of frequencies of both modes is dominated by change of refractive index, change of speed of acoustic modes could be neglected:

$$\Delta v_{TA} = \Delta v_{LA} = \Delta v \approx 0 \quad \text{Eq. 3.20}$$

Then the change of frequencies of both modes could be expressed by simplified formula:

$$\Delta f_{B TA, LA}(n, v) = \frac{2}{\lambda} v_{TA, LA} \Delta n \quad \text{Eq. 3.21}$$

And therefore ratio of detected change of frequencies should be equal to the ratio of corresponding acoustic speeds, which is equal to the ratio of absolute frequencies:

$$\frac{\Delta f_{B TA}}{\Delta f_{B LA}} = \frac{v_{TA}}{v_{LA}} = \frac{f_{B TA}}{f_{B LA}} \quad \text{Eq. 3.22}$$

Based on experimentally obtained values of frequency change, this is of course not true as left side of previous equation is about 2 and right side is smaller than $\frac{1}{2}$.

$$2 \approx \frac{\Delta f_{BTA}}{\Delta f_{BLA}} \neq \frac{v_{TA}}{v_{LA}} = \frac{f_{BTA}}{f_{BLA}} < \frac{1}{2} \quad \text{Eq. 3.23}$$

Therefore, it can be concluded that effect of change of refractive index with temperature is minor and change of speed of propagation of acoustic modes dominates. In that case, the Brillouin shift can be written as:

$$\Delta f_{BTA,LA}(n, \nu) \cong \frac{2}{\lambda} \Delta v_{TA,LA} n \quad \text{Eq. 3.25}$$

And therefore ratio of changes of frequencies of modes should be equal to ratio of speed changes of modes what is equal to about 2:

$$\frac{\Delta f_{BTA}}{\Delta f_{BLA}} = \frac{\Delta v_{TA}}{\Delta v_{LA}} \approx 2 \quad \text{Eq. 3.26}$$

This means that change of TA mode speed is about two times greater than change for LA mode.

As a summary of this study, we can say that we do not detect some special anomaly in the generation of TA mode at the Néel temperature. This might indicate that the magnetic ordering is not a driving order that triggers the light-induced coherent acoustic phonons in BFO. On the other hand, we report clear evidence of some elastic anomalies versus the temperature. A clear softening of both the LA and TA modes is revealed with a more important softening for the TA mode. We can even say that this softening is pronounced above the Néel temperature for the TA mode. Because the LA signal is weaker, for this particular studied grain, it is not as easy to conclude for the LA mode. We also report a significant increase of the damping of the TA and LA waves above the Néel temperature as if the antiferromagnetic ordering “freezes” some scattering processes. Our results evidence a clear coupling between the magnetic ordering and the coherent acoustic phonons. These anomalies are consistent with those recently reported in the literature based on inelastic neutron scattering that also revealed some larger phonon anharmonicity above Néel temperature [69, 70]. The latter literature reports deal with thermal phonons, while we evidence the spin-phonon coupling with coherent acoustic phonons. The coupling between phonon and spin in BFO is still a matter of debate in the literature. No theory currently exists to explain this spin-phonon coupling in BFO. We confirm the existing anomalies but contrary to what has been reported one time in BFO films [71], we did not evidence some possible coherent magnon mode.

3.5 Conclusion

In this chapter we have dealt with photoinduced coherent acoustic phonons (LA and TA) in different grains of a polycrystalline BFO sample. The main conclusion of this chapter is that BFO is potentially a very efficient source of optically triggered high frequency acoustic phonons with both longitudinal and transverse polarizations. We show that polycrystalline BFO sample offers a tunable source of coherent acoustic phonons. Design of structures with variable crystallographic orientations may possibly offer sources of acoustic phonons with desired properties. The acoustic response under femtosecond optical stimulation is very linear in this material (amplitude of strain, or acoustic pulse is proportional to fluence of excitation), what is desired from application point of view.

The photoinduced strain mechanism was discussed. Our conclusions indicate that the inverse-piezoelectric effect is likely to drive the emission of coherent acoustic phonon. However the lack of saturation of the amplitude of the coherent acoustic phonon, as a possible indication of the saturation of the internal polarization by photoexcited carriers, could indicate that the photo-induced strain process is more complex than what we currently describe. A model based on a sequence of capacitors was proposed at least.

Besides the generation mechanism, it is necessary to take into account that optical detection of acoustic phonons in BFO also plays important role and can considerably affect on the detected amplitudes of acoustic phonons. Even if the discussion was based on well-defined crystallographic orientation, the absence of well-tabulated elasto-optic coefficients requires some new investigations with maybe BFO single crystal of high quality and perfectly orientated.

Finally, it can be concluded that temperature dependence and in particular the antiferromagnetic ordering, does not have significant influence on the generation of acoustic phonons. It means that useful properties of BFO, especially in optical generation of strain and acoustic phonons by optical excitation, can be exploited in broad temperature range, so in quite extreme conditions. However, we have analyzed the temperature dependence of the Brillouin frequencies (LA, TA) and the peak width (lifetime), and an enhanced lattice anharmonicity is observed above the Néel temperature which reveals a clear spin-phonon coupling in this system. A more detailed model is required now to understand at the microscopic level this spin-phonon interaction.

Chapter 4: Ultrafast mode conversion of light induced by coherent phonons in birefringent media

4.1. Introduction

In the previous chapter we have revealed in the time-resolved Brillouin experiments that some the Brillouin spectra could have complex components due to the birefringence of BFO. The discussion we develop in the following is based on experimental results obtained with a simple grain orientation where the optical axis is parallel to the surface. We remind that this orientation is the best one to reveal the largest birefringence. It is worth to remind too, that the photoelastic tensor of BFO is unknown. As a matter of fact we will compare our observations with better characterized birefringent samples such as ferroelectric LiNbO₃ (LNO) and calcite (CaCO₃) in order to get a deeper understanding of the physical origin of the photoelastic process. Beyond the Brillouin modes splitting (Brillouin mode detected with ordinary and extraordinary probe light) we used to probe the crystallographic orientation of the grain during a pump-probe experiment (Chapter 3 and Appendix 2), we show in this chapter 4 that more complex photon-phonon scattering processes can take place with, for example, light mode conversion. These original findings was never reported in picosecond interferometry before, up to our best knowledge. Before the presentation of the results, we remind the Brillouin scattering theory in an optically anisotropic medium.

4.2. Theory

For a birefringent medium like BFO a complex photon-phonon scattering process is expected. The existence of two different refractive indices in the case of uniaxial medium like BFO, ordinary and extraordinary, leads to two different states of light propagating through such medium. State of light depends on the polarization of light with respect to the direction of optical axis. Ordinary light beam, propagating at the speed c/n_o , has its polarization perpendicular to the optical axis, whereas purely extraordinary light beam (c/n_e) has its polarization oriented along the optical axis. The basic properties of light are reminded below:

$$v = \frac{c}{n} \quad \text{Eq. 4.1}$$

$$\lambda = \frac{\lambda_0}{n} \quad \text{Eq. 4.2}$$

$$p = \frac{h}{\lambda} = \frac{hn}{\lambda_0} \quad \text{Eq. 4.3}$$

where: v – speed of light in the medium

c – speed of light in vacuum

n – refractive index of medium

λ – wavelength of light in the medium

λ_0 – wavelength of light in vacuum

p – momentum of photon in the medium
 h - Planck constant

Because different momenta of photons can exist in the birefringent solid, this leads to distinctive interactions of photons with phonons [72]. The different scattering processes are shown in Fig. 4.1. In particular, in the case to two different momenta of incident photons, there can be distinguished in consequence four scattering processes which are combinations of incident and scattered state of light. When ordinary state of light is marked as (o) and extraordinary state is marked as (e) we have the following four scattering processes: (o)-(o), (e)-(e), (o)-(e), (e)-(o). There can be a situation where light is scattered to the same state of polarization, for example ordinary to ordinary, but also in principle can exist mixed processes in which light is scattered to another polarization state (mode conversion process) as for example ordinary to extraordinary.

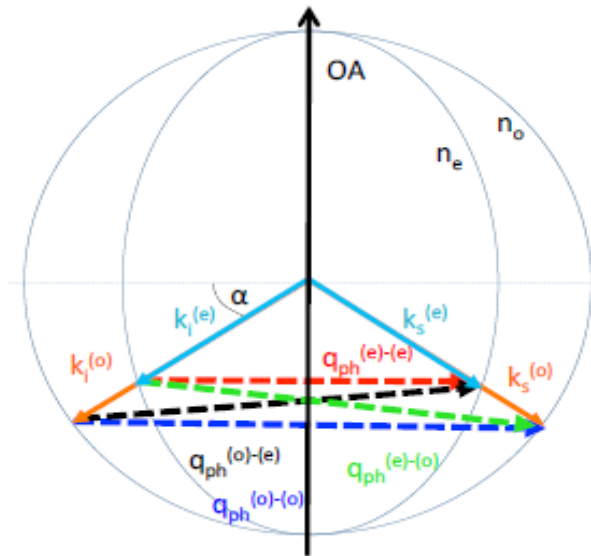


Fig. 4.1. Brillouin scattering processes in uniaxial crystal with negative birefringence ($n_e < n_o$). OA means the optical axis. Four different scattering processes can give detection of four Brillouin frequencies corresponding to four momenta of phonons scattering photons. k_i – momentum of incident photon (before scattering process), k_s – momentum of scattered photon, q_{ph} – momentum of acoustic phonon

In the case of this so-called Brillouin scattering, the acoustic frequency ω_a is much smaller than optical frequencies of incident and scattered light (energy of photons is much higher than energy of phonons), so the scattering could be considered as quasi-elastic, *i.e.* the change in frequency of the scattered light can be neglected. The momentum conservation law is:

$$\vec{k}_s = \vec{k}_i + \vec{k}_a \quad \text{Eq. 4.4}$$

where: \vec{k}_s – wavevector of scattered photon

\vec{k}_i – wavevector of incident photon

\vec{k}_a – wavevector of scattering acoustic phonon

This formula states simply that momentum of incident photon plus momentum of scattering phonon results in new momentum of scattered photon.

In case of Brillouin scattering experiments realized at normal incidence, only backscattered light with direction of scattered wavevector of photon opposite to incident one is collected. In this case, momentum conservation law can be written in simplified scalar version:

$$k_a = k_i + k_s \quad \text{Eq. 4.5}$$

where: k_a – wavenumber of acoustic phonon

k_i – wavenumber of incident photon

k_s – wavenumber of scattered photon

This formula states that value of momentum transferred to backscattered photon by phonon is equal to sum of incident and scattered momenta of photons. In Eq. 4.6, it can be reformulated by expressing acoustic wavenumber by acoustic speed and frequency on the left side and by representing wavenumbers of light by corresponding wavelengths:

$$\frac{\omega_B}{v_a} = 2\pi \left(\frac{1}{\lambda_i} + \frac{1}{\lambda_s} \right) = \frac{2\pi}{\lambda_o} (n_i + n_s) \quad \text{Eq. 4.6}$$

where: ω_B – acoustic pulsation equal to Brillouin pulsation

v_a – speed of propagation of acoustic phonons scattering light

λ_i, λ_s – wavelengths of incident and scattered light respectively

n_i, n_s – refractive indices corresponding to incident and scattered state of light

It can be finally rearranged to get the more general formula for detected Brillouin frequency:

$$f_B = \frac{(n_i + n_s) \times v_a}{\lambda_o} \quad \text{Eq. 4.7}$$

We remind in the following why time-resolved Brillouin scattering detects Brillouin frequencies which are frequencies of propagating acoustic phonons. Laser probe light reflected from sample surface is proportional to incident light (to the reflection coefficient) and especially it can be assumed that it is in phase:

$$E_r \sim E_i \sim \sin \omega_L t \quad \text{Eq. 4.8}$$

where: E_r, E_i – electric field of reflected and incident light respectively

ω_L – cyclic frequency (pulsation) of laser probe light

Whereas the light backscattered into air will be delayed in phase because of the additional propagation of distance $x(t)$ through the medium to and from acoustic phonons:

$$E_s' \sim \sin(\omega_L t - k_i x(t) - k_s x(t)) \quad \text{Eq. 4.9}$$

where: E'_s - electric field of scattered light

k_i, k_s – optical wavenumber of incident and scattered probe light in the medium respectively

The signal at photo detector is proportional to light intensity, i.e. to $(E_r + E'_s)^2$. The only low frequency signal coming from this term which could be time-resolved by the photo detector is $\sim E_r E'_s \sim \sin(\omega_L t) \sin(\omega_L t - k_i x(t) - k_s x(t))$ and from this product only slowly varying part $\sim \cos(k_i x(t) + k_s x(t))$ is playing a role.

So the expected oscillation frequency from detection is in formula:

$$\sim \cos(k_i x(t) + k_s x(t)) \sim \cos(k_i v_a t + k_s v_a t) \sim \cos[(k_i v_a + k_s v_a)t] \quad \text{Eq. 4.10}$$

And it can be extracted as:

$$\omega_B = k_i v_a + k_s v_a \quad \text{Eq. 4.11}$$

This can be reformulated as follows to evidence more directly the frequency of detected acoustic phonons:

$$\frac{\omega_B}{v_a} = k_i + k_s = k_a \quad \text{Eq. 4.12}$$

Coming back to equation for detected Brillouin frequency (Eq. 4.7), we show that from a physical point of view there could be detected (if scattering with mode conversion is possible) up to 3 Brillouin frequencies scattered by this propagating acoustic mode (for normal incidence). The model shows that this works for both LA and TA modes.

Therefore corresponding detected Brillouin frequencies are:

$$f_B^{(o)} = \frac{2n_o \times v_a}{\lambda_o} \quad \text{Eq. 4.13}$$

$$f_B^{(m)} = \frac{(n_o + n_e) \times v_a}{\lambda_o} \quad \text{Eq. 4.14}$$

$$f_B^{(e)} = \frac{2n_e \times v_a}{\lambda_o} \quad \text{Eq. 4.15}$$

When incident ordinary light is back scattered to extraordinary one or vice versa, both situations leads to detection of the same frequency. Moreover, this frequency (e-o) should be centered exactly between frequencies detected from scattering without conversion of light polarization, as formula for mixed process is average of two other formulas. According to our best knowledge the mode-conversion was reported only rarely in Brillouin spectroscopy [72, 73, 74, 75] but never reported in the time-domain Brillouin spectroscopy. The birefringent effect, with only the (o)-(o) and (e)-(e) processes, was reported one time in time-resolved Brillouin scattering [76] in TeO₂ crystals. This mode-conversion phenomenon is at the core of this chapter since. We will compare this photoelastic process in BFO with that of another ferroelectric material (lithium niobate LiNbO₃, LNO) and that of the canonical birefringent material CaCO₃ (calcite). We give below a table summarizing some of the birefringence in various materials.

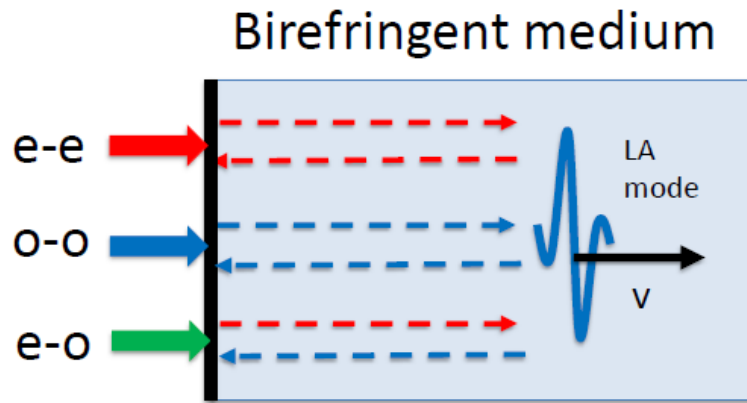


Fig. 4.2. Picture showing different possible scattering processes by LA mode leading to detection different Brillouin frequencies in optically anisotropic medium.

Material	Lattice symmetry	n_o	n_e	Δn
CaCO ₃ (@590nm)	Rhombohedral/Trigonal	1.658	1.486	-0.172
LiNbO ₃ (@590nm)	Rhombohedral/Trigonal	2.272	2.187	-0.085
Quartz SiO ₂	Rhombohedral/Trigonal	1.544	1.553	+0.009
Rutile TiO ₂	Tetragonal	2.619	2.903	+0.287
BiFeO ₃ (@800nm)	Rhombohedral/Trigonal	2.85	2.65	-0.2
Barium borate BaB ₂ O ₄	Rhombohedral/Trigonal	1.677	1.553	-0.124

Table 4.1: some birefringent materials.

A zoom on the dispersion of the refractive index of BFO is given in Fig. 4.3. The value of ordinary refractive index is always higher than that of extraordinary one which in this case shows that BFO is a negative birefringent solid. Values of refractive indices taken for selected photon energies (wavelengths of light) are following: for 800nm value of extraordinary refractive index is about 2.65 and of ordinary is 2.85, for 590nm corresponding values are about 2.80 and 3.05 respectively [41]. Ratio of refractive indices (indicating level of birefringence) for 800nm is about 1.075, whereas for 590nm it is close to 1.089. Therefore it can be concluded that the absolute level of birefringence is larger (birefringence is stronger) for short wavelengths.

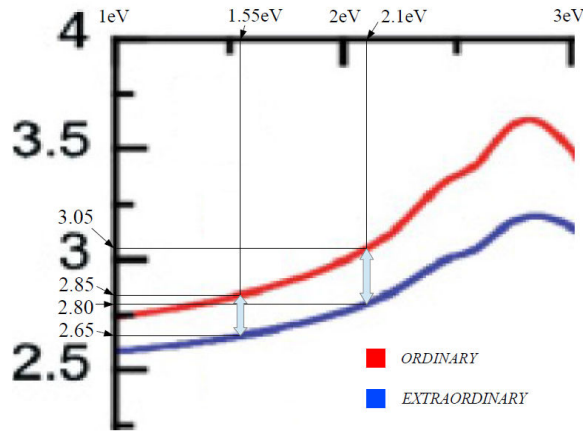


Fig. 4.3. Zoom on the figure 2.14(a). Dispersion of ordinary (n_o) and extraordinary (n_e) refractive index versus energy of photons for bismuth ferrite (BFO). There are indicated values of refractive indices for photon energies 1.55eV (800nm) and 2.1eV (590nm). Different levels of birefringence (indicated by vertical arrows) for different photon energies are noticeable [41].

4.3. Ultrafast mode conversion of light induced by coherent phonons in ferroelectric BFO

In the previous chapter, we have reported a large birefringent effect for the grain 5 (Fig. 3.27), i.e. the crystal having the optical axis parallel to the irradiated surface. This geometry is that exhibiting the largest birefringent effect as expected from the theory. In the following, we will detail the process of Brillouin light-scattering for this particular case. For this particular grain, only the LA mode was detected (Fig. 3.27). In Fig. 3.27, the signal was recorded with a circular polarization, therefore all the details of the detection process were not revealed while with a linear probe polarization, we will show we can discuss all the scattering processes. Probe polarization was simply rotated by a proper half plate to observe the effect on the detection and especially to obtain polarization oriented along or normal to the optical axis as sketched in Fig. 4.4.

It should be mentioned that according to convention, angle θ is measured between probe polarization and direction of optical axis (see Fig. 4.4). Therefore angle 0° corresponds for probe polarization oriented along optical axis (extraordinary) and angle 90° for polarization normal to the axis (ordinary). Polarization oriented between 0° and 90° is a superposition of ordinary and extraordinary light. Results of acoustic detection in BFO presented in this chapter are obtained with probe light at wavelength 590nm. In Fig. 4.5 are reported some transient optical reflectivity signals obtained for variable probe polarizations. It is to be noticed that for purely ordinary or extraordinary probe polarization a single frequency is detected as expected, whereas for intermediate polarization some beatings appear revealing the existence of many components.

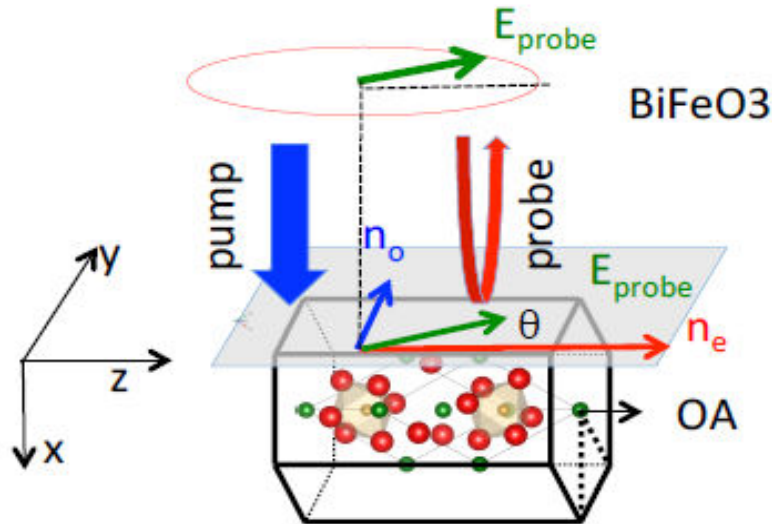


Fig. 4.4. Sketch of the pump-probe experiment carried out on BiFeO_3 grain with optical axis along the z axis (in surface plane, normal to probe beam). Polarization of probe was rotated to obtain specific orientations of electric field of light along (n_e) and normal (n_o) to optical axis as well as superposition of both states.

In order to get a better view of the oscillatory parts, a numerical derivative of the transient signals are shown in Fig. 4.6. Interestingly, the FFT reveal the existence of complex Brillouin spectrum when the probe polarization is in an intermediate configuration. In that latter case, three Brillouin modes are revealed including the (o)-(o) and (e)-(e) processes and additionally the (e)-(o)/(o)-(e) process whose Brillouin frequency exactly lies in the middle of the two side modes as expected from the theory.

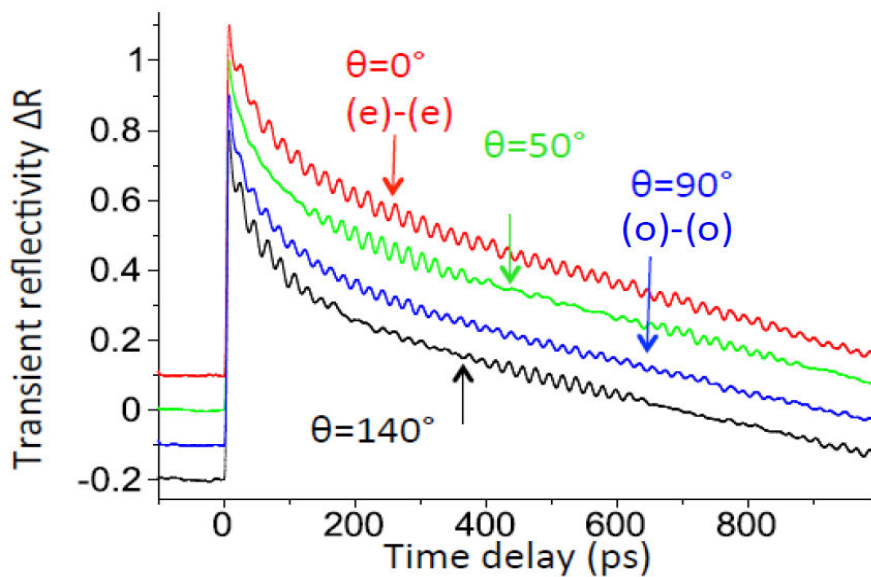


Fig. 4.5. Comparison of transient reflectivity signals collected by four different orientations of probe polarization at wavelength 590nm.

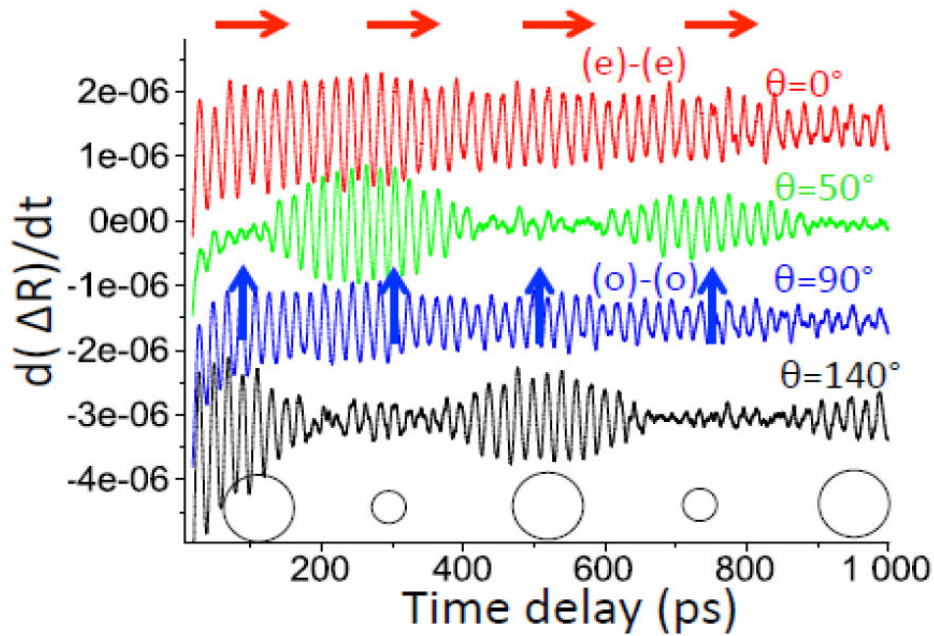


Fig. 4.6. Comparison of signal derivatives obtained by different probe polarizations. We have indicated with arrows or with circles the state of the light polarization versus time.

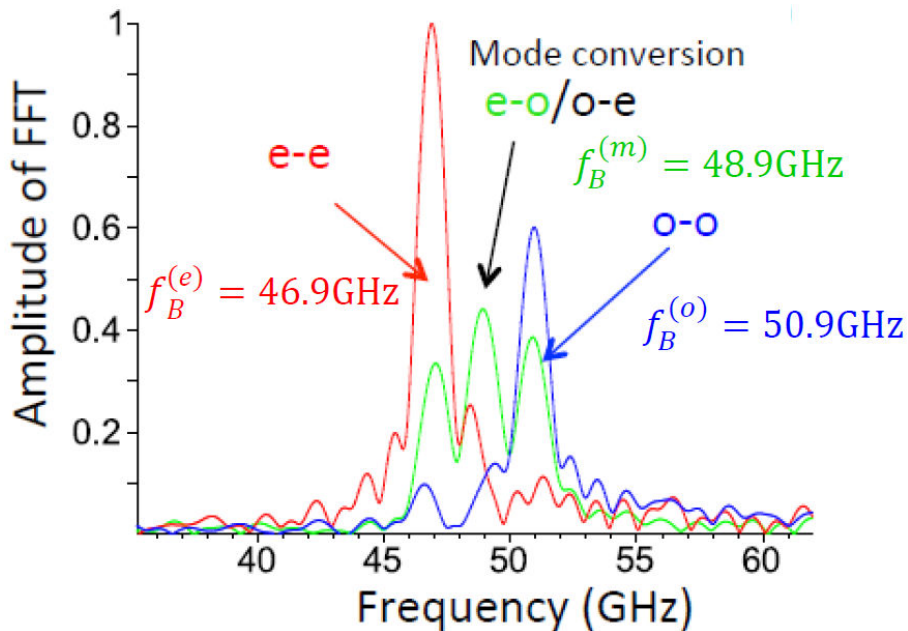


Fig. 4.7. Fast Fourier Transforms (FFT) of the signals revealing the (o)-(o), and (e)-(e) processes but also the mode-conversion process (e-o, o-e). The frequencies corresponding to o-o and e-e process are in full agreement with the expected values and the Brillouin frequency corresponding to the e-o/o-e process is exactly centered between the Brillouin frequencies (o)-(o) and (e)-(e) as predicted by the theory.

In the frequency spectrum it can be directly observed indeed that extraordinary probe polarization detects single frequency at 46.9GHz and ordinary one at 50.9GHz. When detection is realized by superposition of both polarization states, the Brillouin frequency is 48.9GHz, which exactly is the average of the side frequencies as predicted by mode conversion considerations (Eq. 4.14). The amplitude of this peak suggests that mode conversion leading to detection of this frequency is efficient process in BFO at least when light is scattered on LA mode. It has to be stressed that two different signals obtained by two different superpositions of probe light ($\theta=50$ and 140°) have the same spectrum but a π dephasing appears in the time-domain (Figs. 4.5 and 4.6). The full angle dependence of magnitude of each Brillouin components are given in Fig. 4.8 and 4.9 where clear π periodic behavior is found for the (o)-(o) and (e)-(e) processes while a $\pi/2$ periodic dependence is observed for the mode conversion Brillouin mode. It can be observed that for maximum of amplitude from normal scattering of extraordinary polarization there is minimum corresponding to ordinary polarization and vice versa. These properties will be well explained by the model presented in part 3.5 through Eqs. 4.25-4.37.

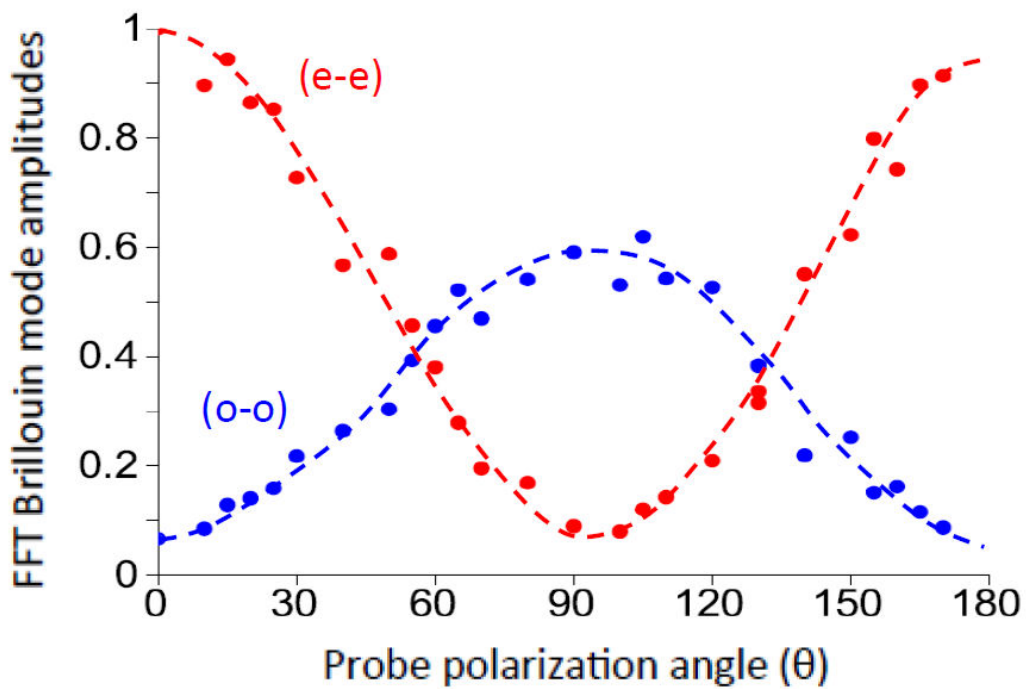


Fig. 4.8. Angle dependence (θ) of amplitudes obtained from FFT of detected Brillouin modes corresponding to normal scattering processes (o-o) and (e-e).

It is worth to note that the Brillouin amplitude of the (e)-(e) process is nearly twice higher than from scattering of ordinary one ((o)-(o)). It can suggest that scattering of extraordinary wave is more efficient than that of the ordinary one. This asymmetry could be also result of more efficient mode conversion of ordinary polarization.

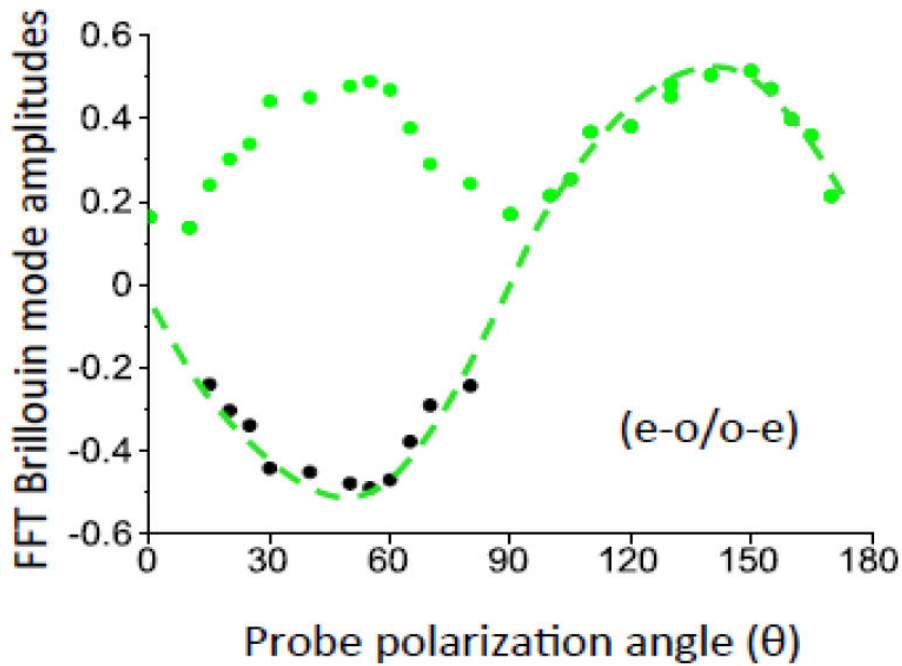


Fig. 4.9. Angle dependence (θ) of amplitude obtained from FFT of detected Brillouin modes corresponding to mode conversion scattering processes (o-e) and (e-o) (green curve). The black curve indicates a change of phase of the signal.

It can be noticed that amplitude of Brillouin frequency from mode conversion vanishes every time the amplitude of one of side peak goes to 0, *i.e.* if the (o)-(o) or (e)-(e) process vanishes. Consequently, if the incident probe is purely ordinary or extraordinary, the mode conversion is not evidenced.

It should be mentioned that in similar way it was studied another grain (not shown) showing strong level of birefringence (big splitting in acoustic spectrum) therefore with optical axis oriented also nearly parallel to the surface. This grain exhibits slightly smaller birefringent splitting than presented one what suggested small inclination of optical axis out of plane (by about 10° compared to nearly 0° for the properties discussed above). In that case, the mode conversion is less pronounced as amplitude of central peak was clearly smaller when compared to already analyzed grain. It suggests that effect of mode conversion is less effective for inclined grain.

The mode conversion of the light at short time scale by coherent acoustic phonons is reported here for the first time and, we believe, is a very interesting property with potential applications related to photoelastic modulator technologies at least. In order to understand better interaction of light with acoustic phonons in birefringent media we have investigated two other birefringent materials, one is ferroelectric (lithium niobate crystal (LNO) and the second is the calcite (CaCO_3). The results are presented below.

4.4. Ultrafast mode conversion of light induced by coherent phonons in ferroelectric lithium niobate (LNO)

As LNO is transparent crystal in the visible range [77, 78], to efficiently excite GHz coherent acoustic phonons in this material it is necessary to use a photo-transducer (thermoelastic process) like a thin metallic film or to work in the UV range by achieving third harmonic generation in a non-linear crystal to get a pump energy higher than the LNO band gap. We have chosen to deposit a thin metallic layer on the top of a LNO wafer. For this purpose surface of LNO crystal was covered by 20nm thin film of chromium (M. Edely, IMMM). Thickness of transducer was selected to efficiently generate GHz acoustic phonons and in the same time to be enough transparent for the detection process. There were used three different cuts of LNO crystal with three main crystallographic orientations for the experiment. It was X-cut, Y-cut and Z-cut of LNO. Capital letter in the name of sample indicates the axis normal to the irradiated surface of crystal, therefore Z-cut of LNO has optical axis (z axis) normal to surface, whereas X-cut and Y-cut have optical axis parallel to surface. The sample quality was carefully checked (X and Z-cut samples) by G. Nataf from LIST (LIST-Luxembourg).

Results obtained on Z-cut of LNO

As optical axis of Z-cut of LNO is normal to sample surface, the probe beam is then aligned along with the optical axis in this geometry. Consequently, the probe polarization always lies perpendicularly to the optical axis, whatever the direction of probe polarization is. Therefore in such geometry, only ordinary light propagates within the LNO crystal.

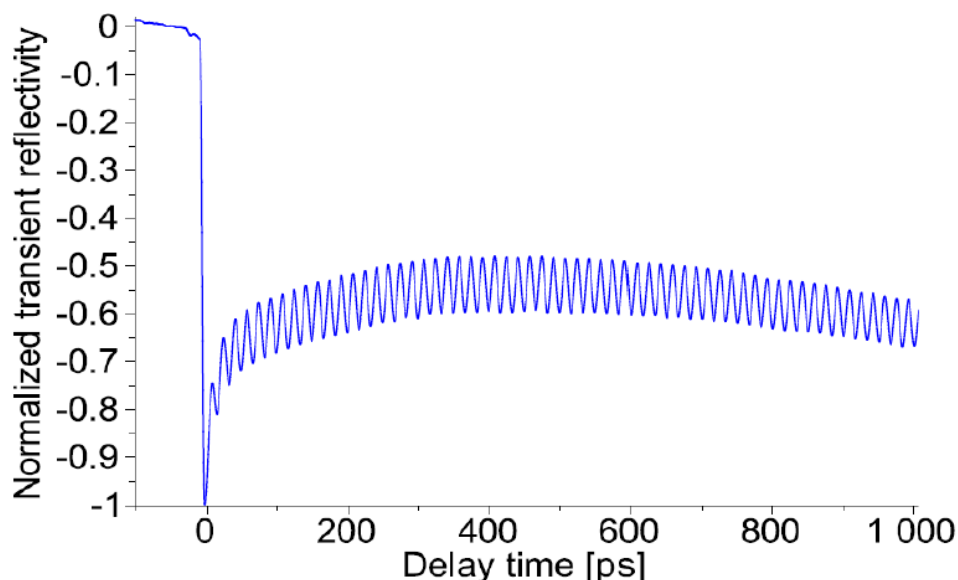


Fig. 4.10. Typical signal detected on Z-cut of LNO sample probed from back side by arbitrary polarization of light.

Same oscillatory component was registered for different orientations of probe light polarization, therefore confirming no effect of polarization rotation on the detected signal. An example of the transient optical reflectivity is given in Fig. 4.10 with the associated Fast Fourier Transform (FFT) in Fig. 4.11. It should be noted that for clarity of the plot there is presented only signal in 1ns range of delay time, whereas it was registered over a range twice longer and it could be registered in principle even in several nanoseconds delay time.

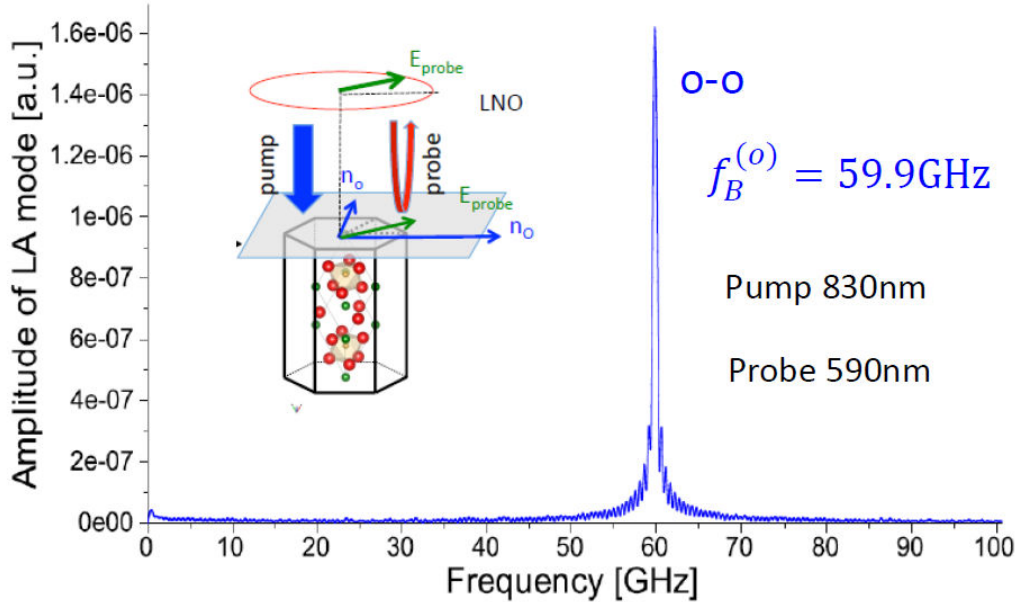


Fig. 4.11. FFT of signal detected on Z-cut of LNO sample. Single well defined frequency is revealed.

FFT transform confirms very good quality of signal obtained on Z-cut of LNO. It shows a very clear spectrum (nearly no background) with pure, well-defined Brillouin frequency 59.9GHz at high resolution. This result confirms only one o-o scattering process in such geometry as expected. When Brillouin frequency is measured and ordinary refractive index is known at wavelength 590nm, then speed of propagation of LA mode can be calculated and compared with speed (v_a) of propagation of sound in this crystallographic direction. We have:

$$v_a = \frac{f_B^{(o)} \lambda_o}{2n_o}$$

Value of ordinary refractive index at wavelength 590nm is about 2.3 [79]. This lead to

$$v_a = \frac{59.9\text{GHz} \times 590\text{nm}}{2 \times 2.3} \approx 7683\text{m/s} \approx 7700\text{m/s} \quad \text{Eq. 4.16}$$

That speed of acoustic propagation can also be estimated thanks to tabulated mechanical properties of LNO from formula:

$$v_a = \sqrt{\frac{c_{33}}{\rho}} \quad \text{Eq. 4.17}$$

where: c_{33} – elastic stiffness coefficient in z-direction with piezoelectric effect correction
 ρ – mass density of LNO

Elastic stiffness coefficient is modified by piezoelectric effect (electro-acoustic wave), as longitudinal components of elastic waves create corresponding longitudinal electric fields in the material which contributes to additional stiffness terms [80, 81]. This property of the electro-acoustic wave has already been evaluated in the literature and the corresponding elastic stiffness required in Eq. 4.17 is $2.45 \times 10^{11} \text{Nm}^{-2}$ [82]. With a mass density of about $4.63 \times 10^3 \text{kgm}^{-3}$ [76] the speed of longitudinal acoustic wave becomes

$$v_a = \sqrt{\frac{2.45 \times 10^{11}}{4.63 \times 10^3}} \approx 7274 \text{m/s} \approx 7300 \text{m/s} \quad \text{Eq. 4.18}$$

This value is in agreement with our estimate within an accuracy of 5%. The discrepancy can be mainly the result of uncertainty of elastic stiffness coefficient measurement that can be influenced by piezoelectric effect which can be different depending on the structure on the ferroelectric domains.

To study effect of birefringence of LNO on detection of acoustic phonons two cuts (X-cut and Y-cut) with optical axis in surface plane have been examined.

Results obtained on X-cut of LNO

Because of a technical problem on the setup used for testing the Z and Y cut LNO (dead diode of the Chamel on Laser), we performed the investigations of X cut on a slightly different configuration that does not alter the analysis and the interpretation. The mode-conversion investigation was carried out on another setup (coll with I. Chaban, PhD student, IMMM) with a chromium coated LNO wafer and the pump and probe wavelength were fixed at 800nm and 400 nm respectively (contrary to 830nm and 590nm for Z-cut LNO crystal). The probe beam was slightly oblique with an angle of about 30° versus normal to the surface. Because of a large refractive index of LNO this leads only to a slight oblique incidence of light within the crystal (around 10°). Probing at angle leads in general to two geometric configurations when optical axis of crystal is in surface plane. In this case optical axis can be either normal to plane of incidence of probe light or it can be in plane of incidence. In consequence for the first configuration probe polarization can be pointed fully along optical axis (and also normal to it) when rotated, and for second configuration polarization of probe along optical axis is not possible (it can be only fully normal to axis for specific polarization orientation and only component of polarization can be pointed along optical axis for other orientation). This different possible geometry of probe beam in respect to orientation of optical axis leads to difference in scattering process and especially in the appearance of mode conversion effect. At a probe wavelength of 400nm, the ordinary and extraordinary refractive index is 2.44 and 2.33 respectively [83]. The dispersion of the refractive index is shown in Fig. 4.12 [78].

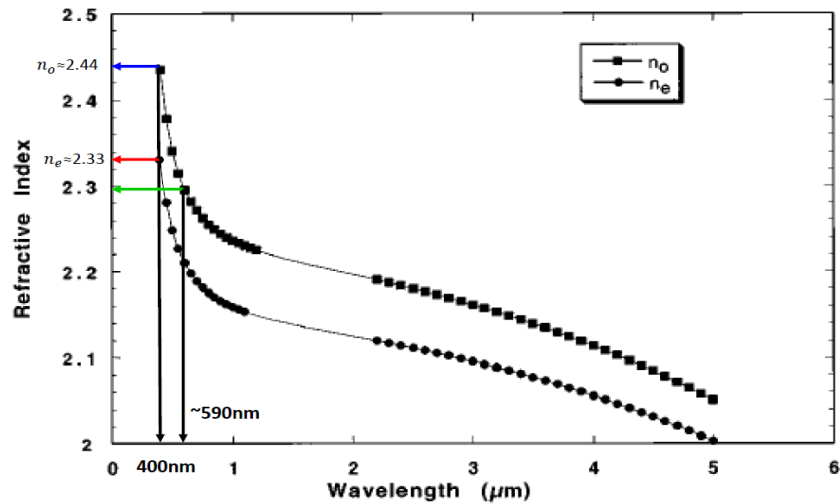


Fig. 4.12. Refractive indices of undoped congruently grown LiNbO_3 as a function of wavelength. The solid curves represent the three-oscillator Sellmeier fit to the data [81].

Probe polarization was rotated to find pure ordinary and extraordinary Brillouin frequency component as well as possible mode conversion effect at superposition of probe polarization.

- Results for the case of optical axis in the incidence plane of the probe light.

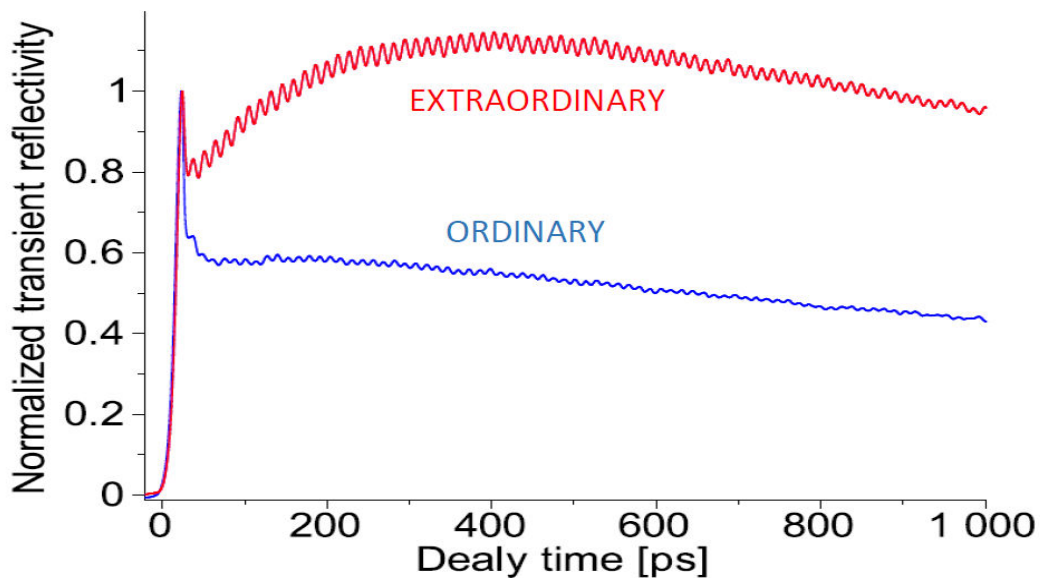


Fig. 4.13. Signals detected for ordinary and extraordinary state of probe polarization.

Amplitudes of both signals registered for two orthogonal probe polarizations were normalized in respect to electronic peak. In direct signals of transient reflectivity it can be observed that not only oscillatory part changes (amplitude and frequency), but also detected background. Origin of change of background is not clear as it can be caused by simultaneous change of optical conditions in experiment during rotation of probe light. Nevertheless, change of parameters of Brillouin oscillation is clear and can be analyzed. For this purpose FFTs of signals were prepared, to compare directly influence of probe polarization on detected frequency and amplitude of Brillouin oscillation.

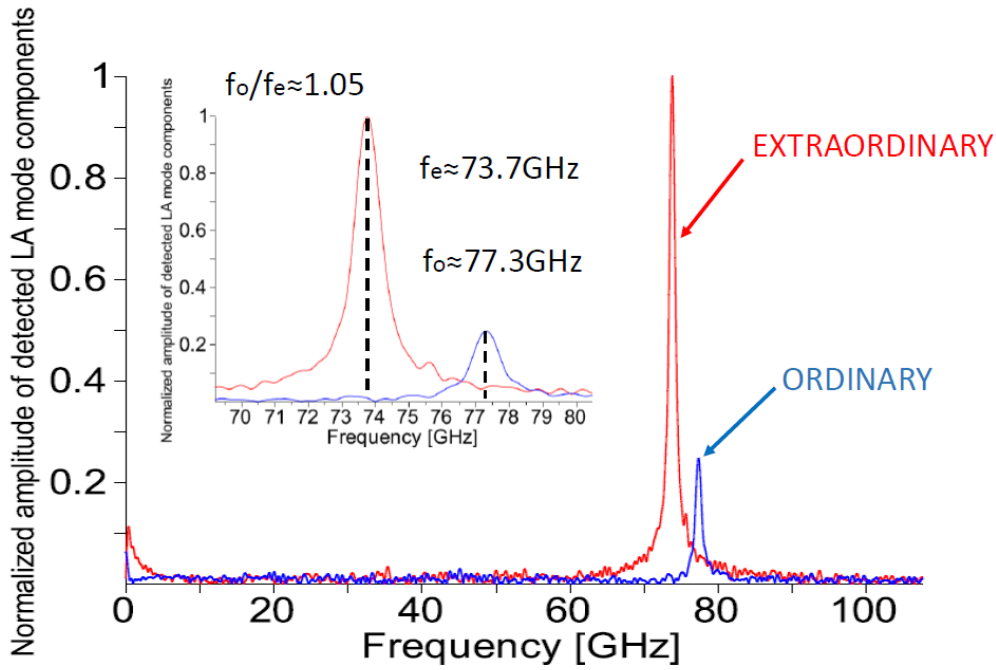


Fig. 4.14. Comparison of LA mode frequencies detected by ordinary and extraordinary probe polarization.

Detection of pure frequency components can be observed when sample is probed by carefully selected polarization orientation. According to values of ordinary and extraordinary refractive indices of LNO (ordinary refractive index is higher than extraordinary one), single mode with smaller frequency can be attributed to the Brillouin mode detected with the extraordinary polarization state, whereas higher frequency can be attributed to detection by ordinary probe polarization. High asymmetry in the detected amplitudes can be observed directly. It suggests that extraordinary polarization is scattered much more efficiently by LA phonons in LNO (at least in discussed geometric configuration) than ordinary one. Therefore it can be concluded that extraordinary polarization state is much more suitable for the detection of acoustic phonons in LNO by picosecond acoustics experiment. Additionally there were taken carefully quite accurate values of detected frequencies and read off values are 73.7GHz and 77.3GHz respectively for extraordinary and ordinary frequency component. This gives ratio of frequencies about 1.049 which is very close to ratio of refractive indexes for wavelength at 400nm taken from literature ($n_o/n_e=2.44/2.33\approx 1.047$). It should be noted that because of detection at angle (probe beam inclined in respect to normal at about 30°), formula for detected Brillouin frequency should be slightly modified by angle of incidence. Formula for Brillouin frequency detected by probe beam at angle α to normal and generalized to two possible refractive indices is following:

$$f_B^{(o,e)} = \frac{2v_a \times \sqrt{n_{o,e}^2 - \sin^2 \alpha}}{\lambda_o} \quad \text{Eq. 4.19}$$

Where subscript o or e depends on which refractive index is valid for given polarization state what gives corresponding value of frequency.

Therefore according to this formula ratio of detected Brillouin frequencies corresponding to ordinary and extraordinary refractive index is:

$$\frac{f_B^{(o)}}{f_B^{(e)}} = \frac{\sqrt{n_o^2 - \sin^2 \alpha}}{\sqrt{n_e^2 - \sin^2 \alpha}} \quad \text{Eq. 4.20}$$

This in the case of incident angle 30° gives values of $\sin \alpha$ equal to 0.5 and leads to ratio:

$$\frac{f_B^{(o)}}{f_B^{(e)}} = \frac{\sqrt{2.44^2 - 0.5^2}}{\sqrt{2.33^2 - 0.5^2}} \approx 1.049 \quad \text{Eq. 4.21}$$

Calculated ratio based on values of refractive indices and angle of incidence of probe beam is in perfect agreement with measured values of Brillouin frequencies up to the third decimal place. Very similar values of both ratios confirm birefringent nature of detection in LNO as well as reported in literature values of refractive indices at least for wavelength 400nm.

To study possibility of mode conversion process in X-cut of LNO different superpositions of probe polarizations were also applied in the acoustic detection. Example of signals obtained by two different superpositions of probe polarization is presented below:

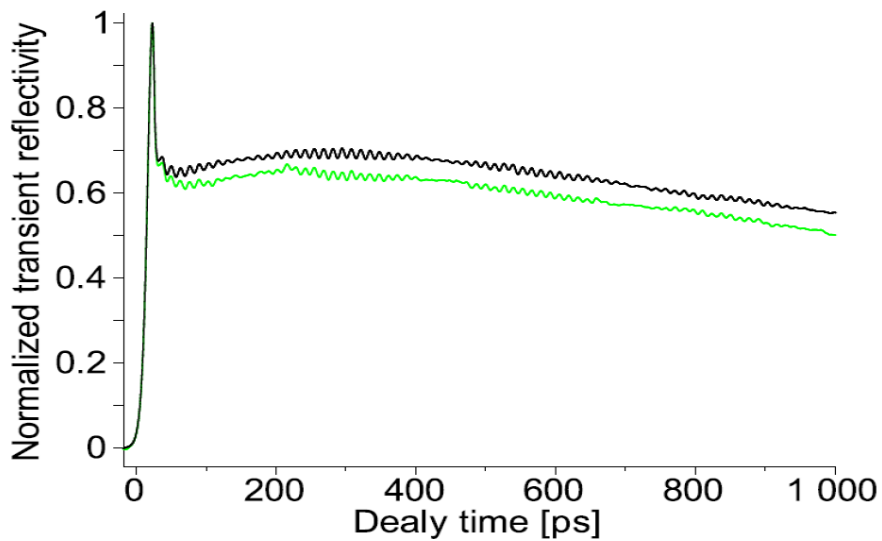


Fig. 4.15. Comparison of two signals with beating of oscillations obtained by two different superpositions of probe polarization.

Derivatives of signals were also prepared to expose better Brillouin oscillations.

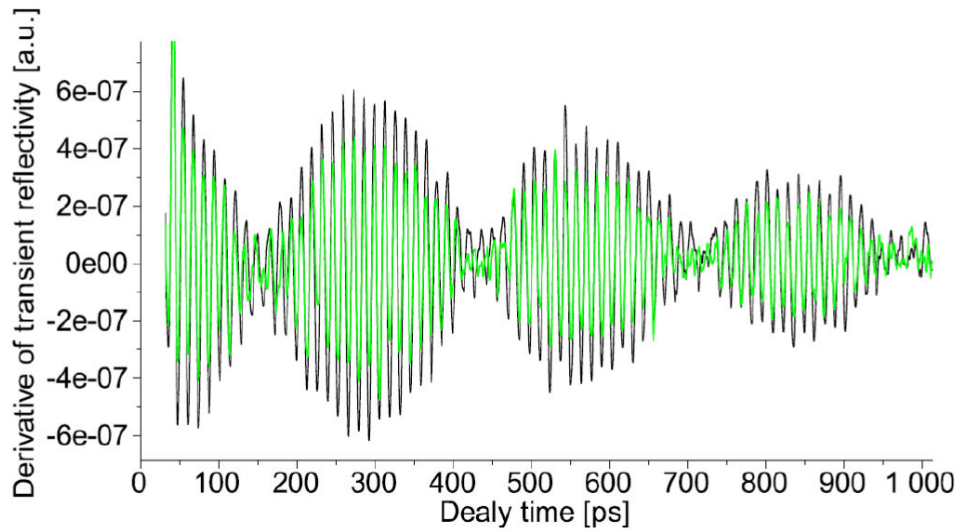


Fig. 4.16. Comparison of two derivatives of signals with beating of oscillations obtained by two different superpositions of probe polarization.

It can be observed pronounced beating of Brillouin oscillations indicating existence of two close frequencies with similar peak amplitudes. It is visible that both signals obtained by different superpositions of probe polarization (initial polarization of probe light rotated by about 90° and 150° , therefore with relative orientation about 60°) are very similar. Only slightly different amplitude distinguishes both signals. It was prepared also a comparison of FFT to directly see the spectrum of both signals.

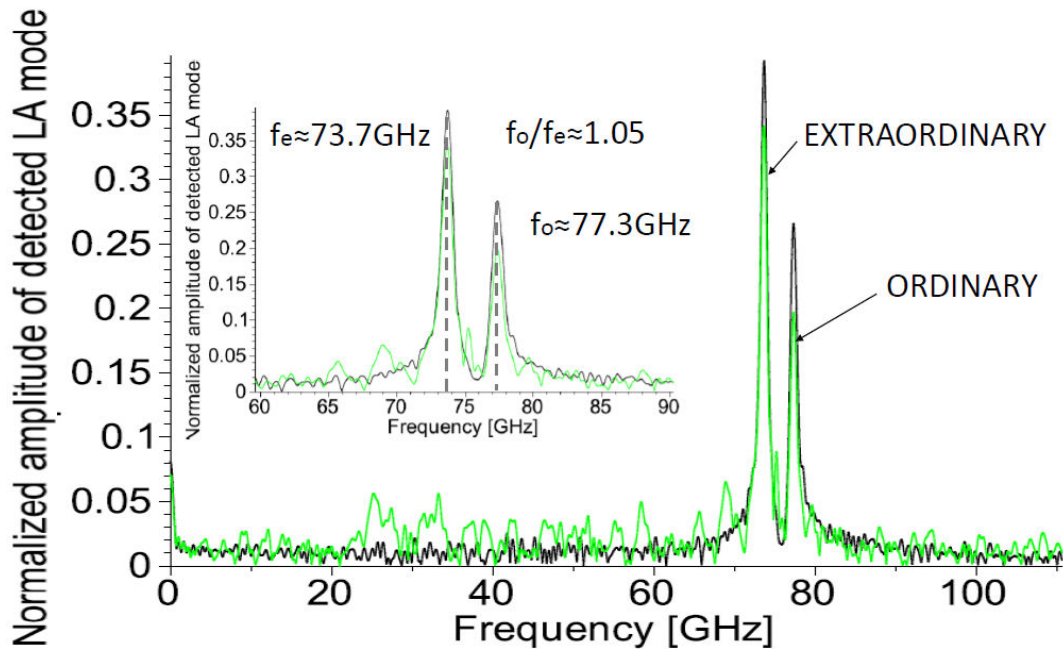


Fig. 4.17. Comparison of splitting in detection of LA mode by two different superpositions of probe light polarization.

In the obtained frequency spectra from FFT there is not any visible peak in the center indicating mode conversion process. Therefore it can be concluded that for this geometry,

i.e. for optical axis oriented in plane of probe beam incidence (probe beam at angle to optical axis) there is no pronounced mode conversion effect.

Finally to study behavior of detected components of Brillouin amplitudes and to confirm fully lack of mode conversion in this case, variable probe polarization was applied and signals were registered for different probe polarization. Amplitudes of both detected components were extracted and plotted versus angle of probe polarization rotation (in respect to initial polarization orientation).

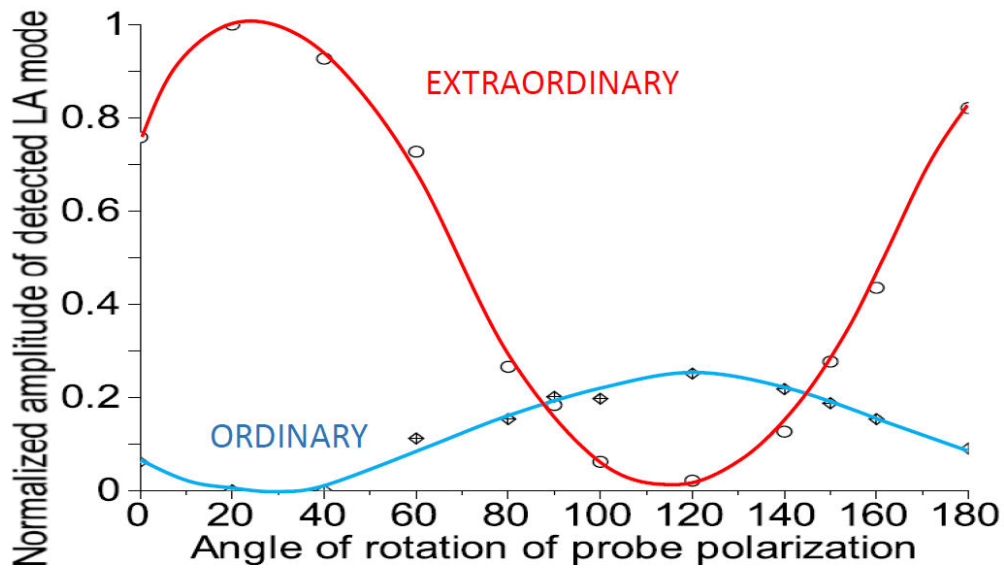


Fig. 4.18. Dependence of amplitudes of detected LA mode components (ordinary and extraordinary) versus orientation of probe polarization.

There is directly visible π periodicity of amplitudes of detected frequency components exactly as in the case of grain of BFO with optical axis in surface plane (see Fig. 4.8). But lack in this case component corresponding to mode conversion process. It can be noticed significant dominance of amplitude corresponding to extraordinary component of probe polarization. Only in narrow range of probe polarization orientations ordinary component exceeds extraordinary one. It can be also observed that for two polarization orientations (superpositions) detected amplitudes of both components are similar and this was presented in comparison of signals obtained by superposition of probe polarization.

- Results for the case of optical axis normal to plane of incidence of probe light (also normal to incident probe beam)

A comparison of two examples of such signals obtained by superposition of probe polarization is presented below.

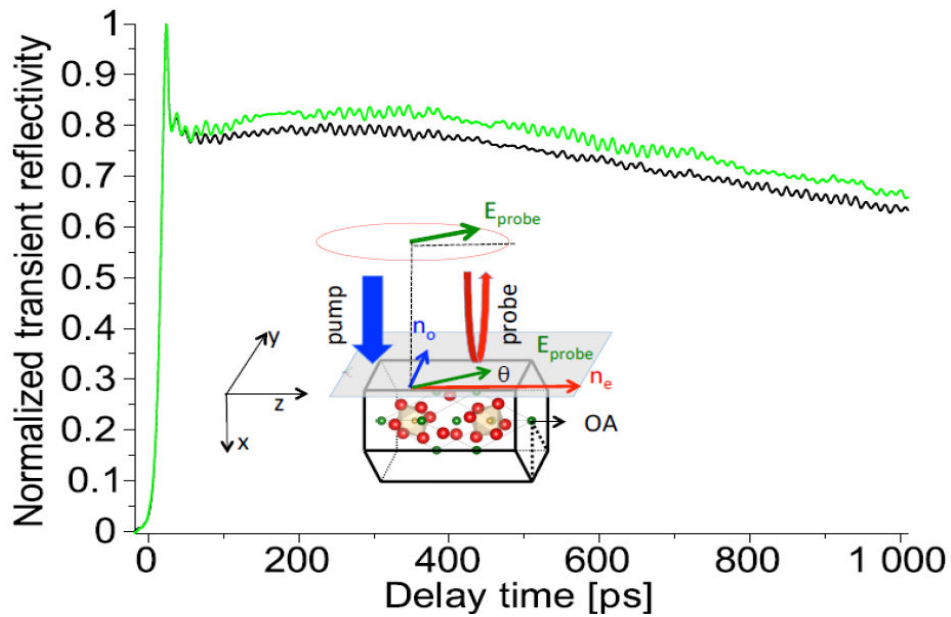


Fig. 4.19. Comparison of signals obtained by two different superpositions of probe polarization.

By comparing both signals it can be noticed that they are quite different. On the beginning Brillouin oscillations seems to be similar but in later times discrepancy between both signals arises and there can be observed inverted trend in amplitude of oscillations. To analyze signals and their content a comparison of FFTs was prepared (Fig. 4.20).

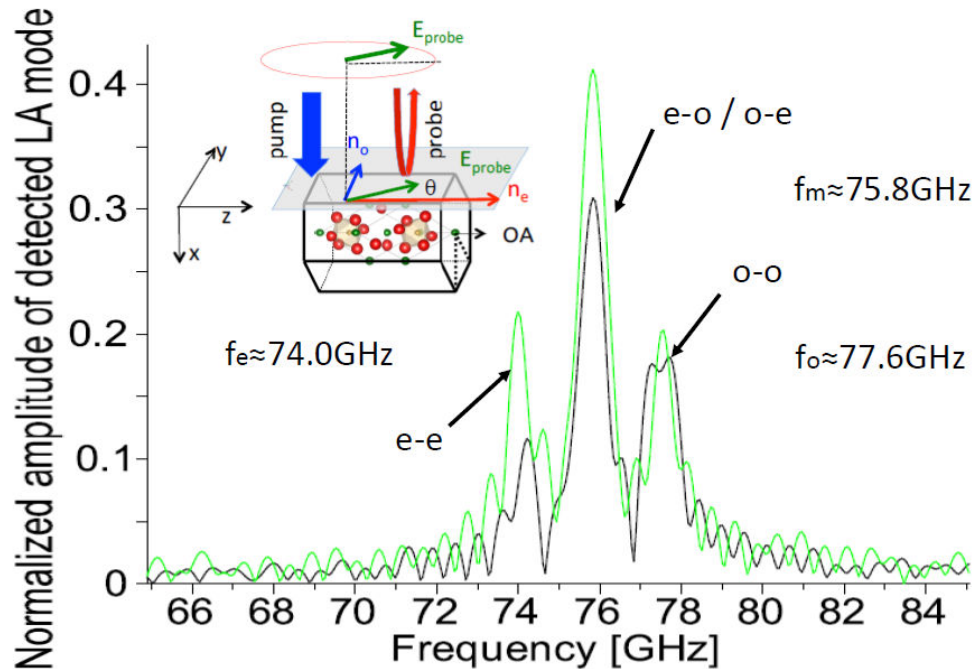


Fig. 4.20. Comparison of LA mode detection by two different superpositions of probe polarization with efficient conversion process.

In the case of probe polarization containing both ordinary and extraordinary components, mode conversion was clearly illustrated through the appearance of the central mode in Fig. 4.20. By comparing amplitudes corresponding to normal scattering processes (o-o and e-e)

with the amplitude corresponding to mode conversion scattering processes (o-e and e-o) it can be stated that scattering with mode conversion is very efficient for LNO. It can be noticed that detected frequencies are slightly higher than in previous case of sample with optical axis oriented in plane of probe incidence. This can be result of probing at different position of sample (after rotation of it with optical axis by 90°) with slightly higher speed of acoustic propagation as both side frequencies corresponding to ordinary and extraordinary refractive index are shifted. Nevertheless frequency revealing mode conversion process is exactly in the center between side frequencies as expected. Moreover ratio of detected values of side frequencies as in previous case is in very good agreement with value of frequency ratio based on the known values of refractive indices and incident probe angle ($f_o/f_e=77.6/74.0\approx 1.049$).

To compare efficiency of mode conversion process with normal scattering process, it was prepared plot comparing highest detected amplitudes for ordinary and extraordinary frequency component with spectrum revealing conversion of probe polarization

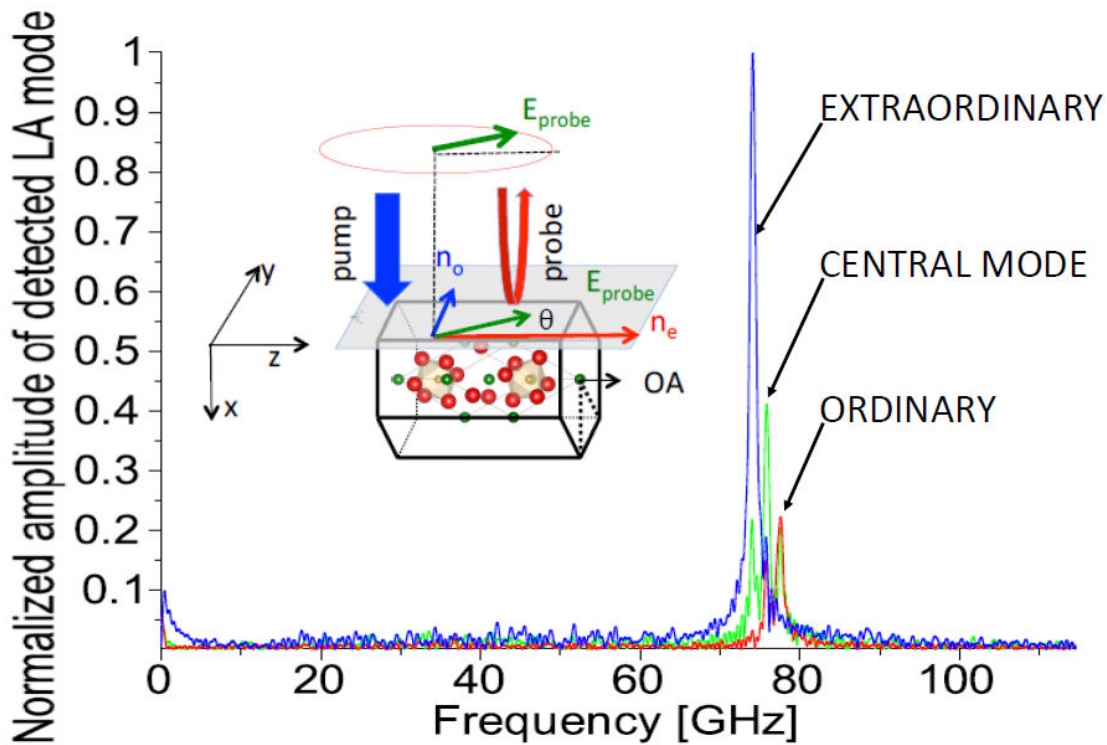


Fig. 4.21. Plot of FFTs comparing detected amplitudes from normal scattering process (extraordinary and ordinary) with amplitude from mode conversion process (central mode).

It can be observed that peak corresponding to mode conversion is clearly higher than maximal detected peak from scattering of ordinary polarization state, but still it is much smaller than amplitude from maximal scattering of extraordinary light. Therefore it can be stated that scattering with mode conversion is relatively efficient, more efficient than o-o but less efficient than e-e scattering processes.

To observe influence of probe polarization orientation on detection of amplitudes from different scattering processes it was prepared dependence of detected amplitudes in function of angle of rotation of probe polarization

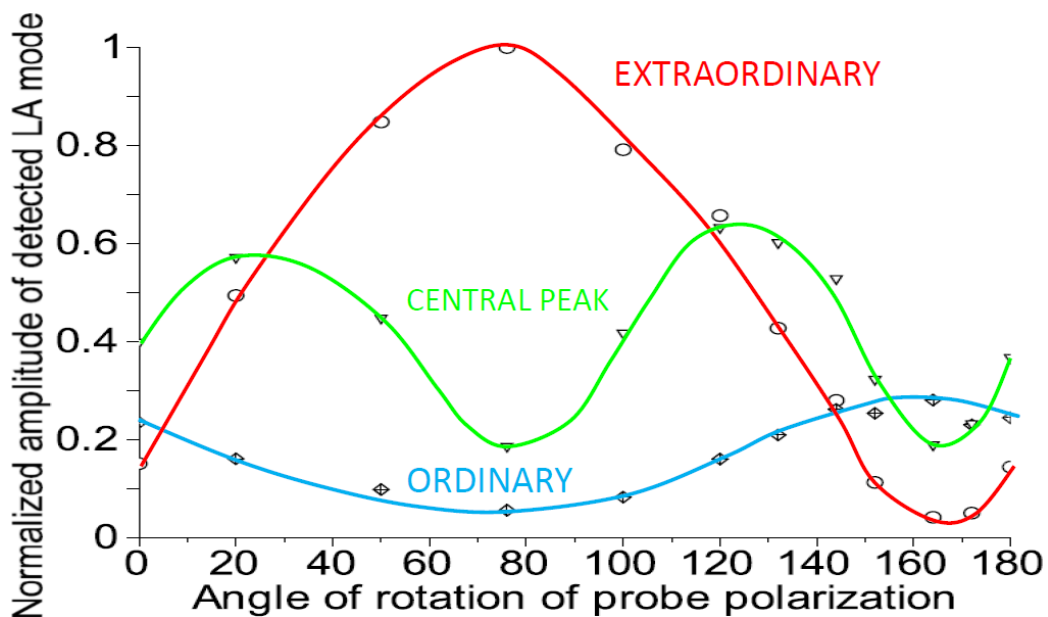


Fig. 4.22. Comparison of normalized amplitude dependence of central peak (from mode conversion process) with side peaks (from normal scattering processes of ordinary and extraordinary component of probe polarization) versus angle of rotation of probe polarization.

A π periodicity of the amplitudes is observed for normal scattering processes ((o)-(o) and (e)-(e)) while the amplitude of central peak from mode conversion has double periodicity ($\pi/2$). We can then say that there is a strong similarity between responses of LNO (Fig. 4.22) and BFO (Figs. 4.8 and 4.9). Besides it can be observed that amplitude of central peak never vanishes totally. When one of the side amplitudes nearly vanishes there is still observed small amplitude corresponding to mode conversion. It can be also observed that detection of mode conversion process is minimal when there is detection by nearly pure ordinary or extraordinary polarization state (when one normal scattering process dominates over another). On the other side maximal detection of polarization conversion happens for relatively strong simultaneous detection of both amplitudes from normal scattering and it can achieve more than half of amplitude from maximal scattering of extraordinary polarization.

Finally to observe directly the effect of sample orientation (OA axis parallel or perpendicular to the incidence plane of the probe beam) we have superimposed the FFTs of two typical signals. There is a striking difference between these both signals based on existence or not of frequency corresponding to mode conversion process.

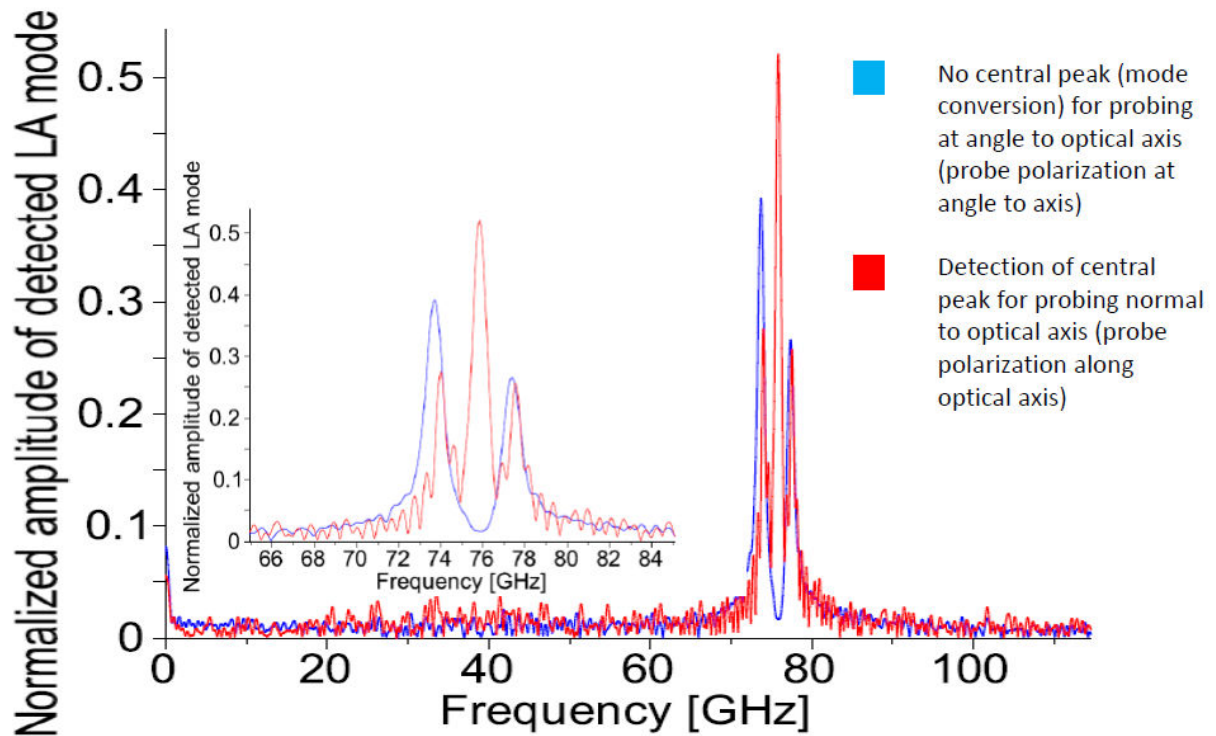


Fig. 4.23. Comparison of signals detected by superposition of probe light for two different orientation of optical axis in plane of LNO X-cut in respect to incident probe beam.

Such comparison shows that orientation of optical axis in respect to direction of probe beam and especially in respect to possible polarization orientations of this beam is a crucial parameter for the occurrence (efficient enough to detect) of mode conversion process. To compare these results with another cut of LNO with optical axis in surface plane picosecond acoustics experiment with variable linear probe polarization was realized on Y-cut of LNO

Results obtained on Y-cut of LNO

Y-cut was also studied in two geometrical configurations when probe beam at wavelength 400nm was applied at angle (30°) with optical axis in plane or normal to the incidence plane of the probe beam. Contrary to X-cut LNO, both detection configurations did not reveal any mode conversion processes since no central mode was detected (Brillouin peak between the (o)-(o) and (e)-(e) Brillouin peak). Brillouin frequencies corresponding to normal scattering of ordinary and extraordinary polarizations state were the only observed components whatever the probe polarization as shown in Fig. 4.24.

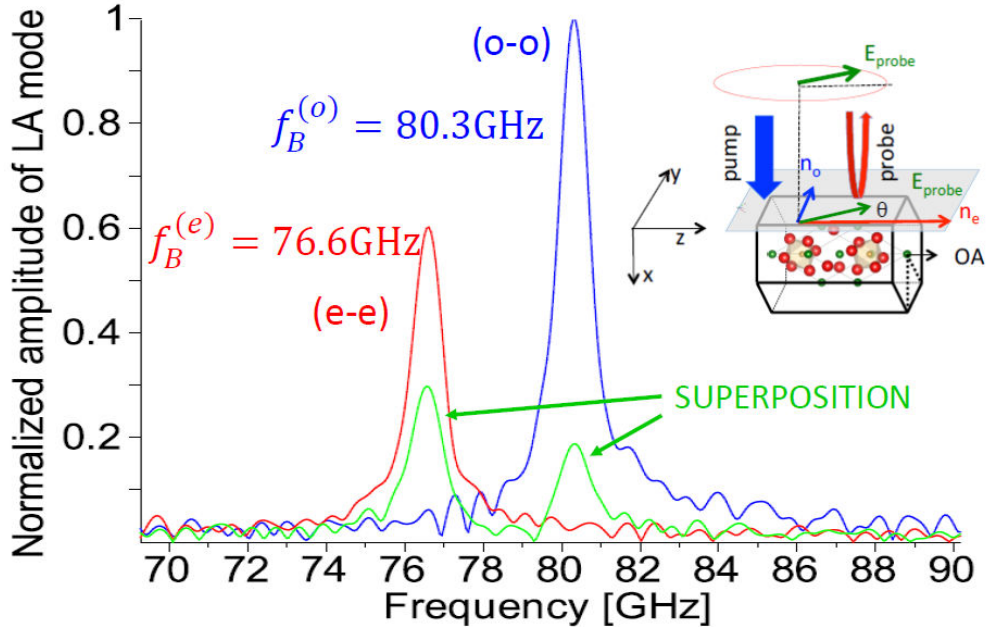


Fig. 4.24. Brillouin frequencies detected in Y-cut of LNO by ordinary and extraordinary probe polarization as well as by superposition of probe polarization.

Two other distinctive features in presented comparison can be discussed which differ them from results obtained for X-cut. First of all there are measured different relative amplitudes for ordinary and extraordinary frequency components. For detection in Y-cut, amplitude corresponding to ordinary component exceeds this for extraordinary one, so it suggests that normal scattering of ordinary polarization is more efficient than of extraordinary one in this case, what is in opposite to observation for X-cut. Moreover, another differences are values of detected frequencies. Both are clearly higher by several GHz than that detected for the case of X-cut of LNO. As probe wavelength applied in both experiment is exactly the same (400nm) as well as couple of refractive indices for axis parallel to surface plane, it can be concluded that shift of detected frequencies is caused by another speed of propagation of LA phonons along X and Y axis. For about 5% higher detected Brillouin frequencies in Y-cut than in X-cut, it means that speed of acoustic propagation along Y-axis is higher by this factor than speed along X-axis, what can be verified by calculations of acoustic propagation speed in different crystallographic directions based on elastic properties of LNO. Finally, even if shifted, ratio of detected frequencies is still in very good agreement with prediction of this ratio based on known values of refractive indices at wavelength 400nm.

$$\frac{f_B^{(o)}}{f_B^{(e)}} = \frac{80.3\text{GHz}}{76.6\text{GHz}} \approx 1.048$$

Eq. 4.22

4.4. Detection of LA phonons in birefringent crystal of calcite (CaCO_3)

Calcite is a very common birefringent (doubly refractive) material. It is transparent mineral with formula CaCO_3 . This material exhibits very high level of birefringence (uniaxial optical anisotropy) (see Table 4.1), one of the highest among all known birefringent materials. Classical Brillouin scattering experiments done on this crystal showed scattering of both ordinary and extraordinary light by thermal phonons with potential possibility of mode conversion [72,84]. Such experiments were mainly done to obtain photoelastic tensor elements for this material as well as elastic constants. (*Remark : there are very interesting theoretical and experimental reports exploiting birefringent nature of calcite to design and to obtain for example invisibility cloaking which can potentially hide small objects [85, 86]. Therefore birefringence of calcite can have potentially interesting and spectacular applications.*)

This birefringence is easily evidenced with large single crystal as shown in Fig. 4.25.

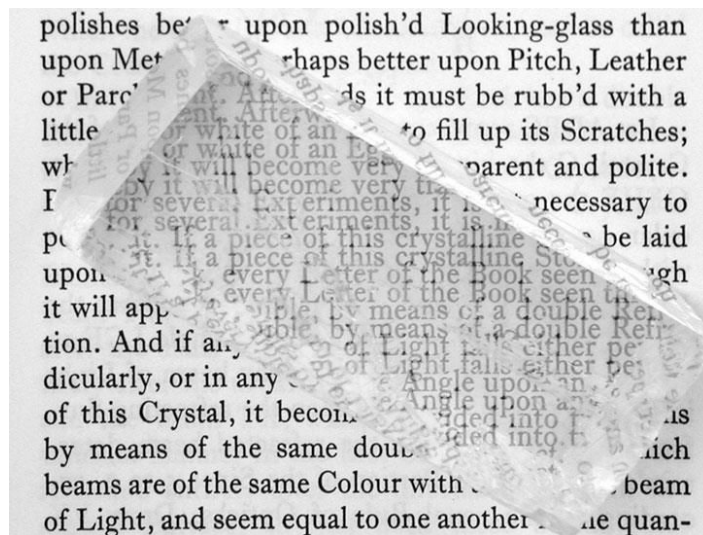


Fig. 4.25. Double refraction through a piece of calcite.

Plot of dispersion relation of both ordinary and extraordinary refractive indices of calcite for broad range of wavelengths from ultraviolet to infrared region is given below.

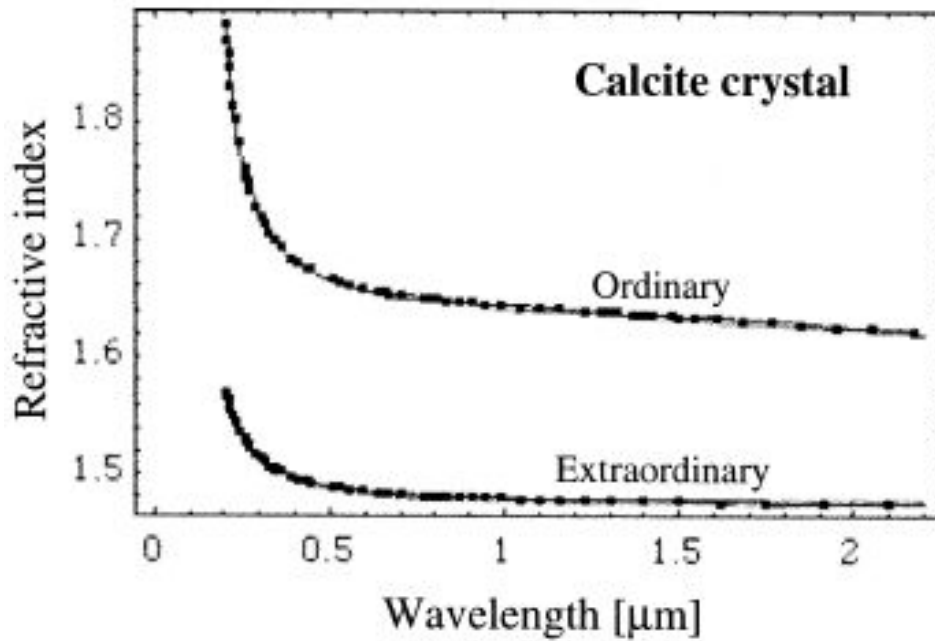


Fig. 4.26. The experimental and computed values of refractive index for calcite crystal: points-experimental data, solid curves-computed values [87].

At a wavelength of 590 nm, which is the probe wavelength we worked with, calcite has an ordinary and extraordinary refractive indices of 1.658 and 1.486 respectively [85, 88] (see Table 4.1).

Studied sample

To demonstrate effect of birefringence of calcite on detected Brillouin frequency in picosecond acoustic experiment, a small piece of this crystal with natural orientation of optical axis at about 45° relatively to surface plane was chosen (natural cut of calcite, i.e. cleaved surface). Only crystal with such orientation of optical axis was accessible for now to experiment with sufficiently high quality of surface. Because it is transparent in all visible range like LNO, it was also covered by thin film of chromium acting as transducer in similar way as in the case of LNO sample. It was done to efficiently excite desired spectrum of GHz LA phonons. Transducer was excited by wavelength at 830nm and sample was probed by wavelength at 590nm at normal incidence. We have tried to prepare a Cr coated sample with the optical axis (OA) parallel to the surface but we did not get enough high quality of the surface.

Case of optical axis inclined in respect to surface

When optical axis is at $\sim 45^\circ$ versus surface then direction of probe light propagating perpendicularly to surface is also all time at around 45° versus optical axis. For such configuration light never can be totally polarized along optical axis, for certain orientations polarization can be only fully normal to the optical axis. In such case we have to use the effective extraordinary refractive index ($n_{eff} \cong 1.56$) rather than the pure extraordinary one as explained in Appendix 2. For a crystal orientation defined by an angle of 45° (Fig.

4.27) the expected ratio of Brillouin frequencies detected by ordinary and extraordinary light is close to 1.06.

$$\frac{f_{Bo}}{f_{Be}} \cong \frac{n_o}{n_{eff}} \approx 1.06 \quad \text{Eq. 4.23}$$

A probe polarization dependence of the transient optical reflectivity has been studied according to the geometry sketched in Fig. 4.27. Some typical time-domain signals are shown in Fig. 4.28.

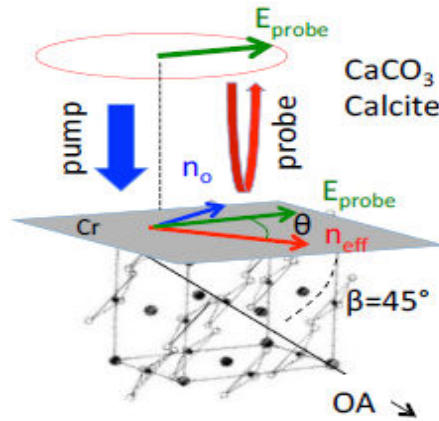


Fig. 4.27. Picture showing scheme of pump-probe experiment carried on calcite sample. OA marks optical axis of crystal of calcite which is oriented at angle of 45° in respect to the surface.

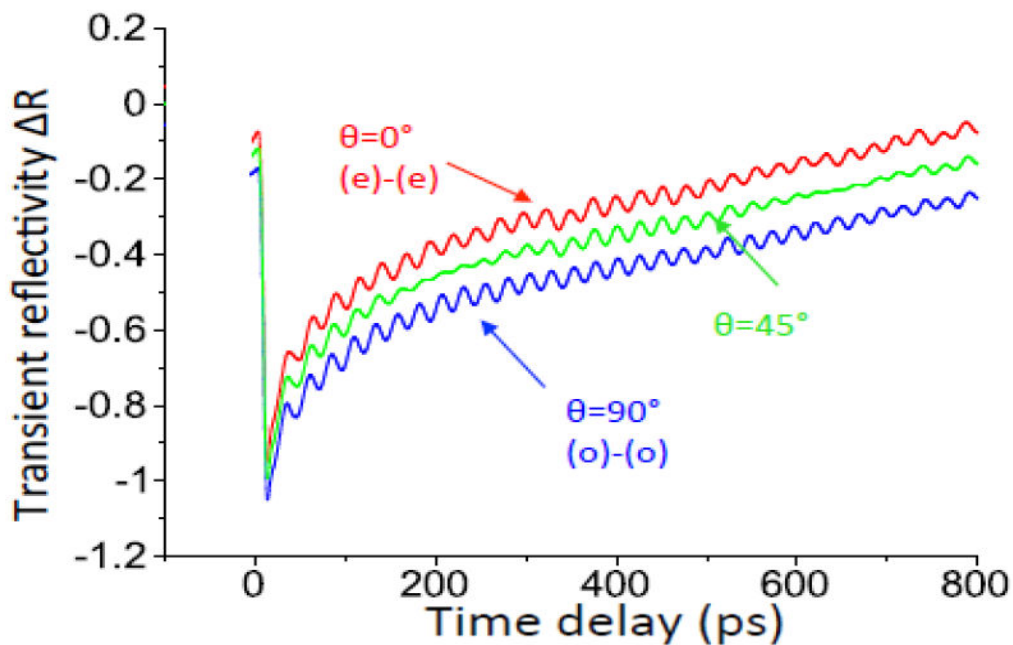


Fig. 4.28. Comparison of signals detected by ordinary and extraordinary probe polarization with the signal detected by superposition of probe polarization.

Similar amplitude of oscillations for every applied probe polarization can be observed. As expected with a pure ordinary or extraordinary light, only one Brillouin component is

revealed as well evidenced in the time-derivative signals and on the FFT shown in Figs. 4.29 and 4.30 respectively. The most interesting signal is registered by superposition of probe polarization, what means polarization oriented at angle about 45° in respect to projection of optical axis (OA) onto the plane surface. We have a clear beating of the signal which reveals the presence of two components (Figs. 4.29 and 4.30).

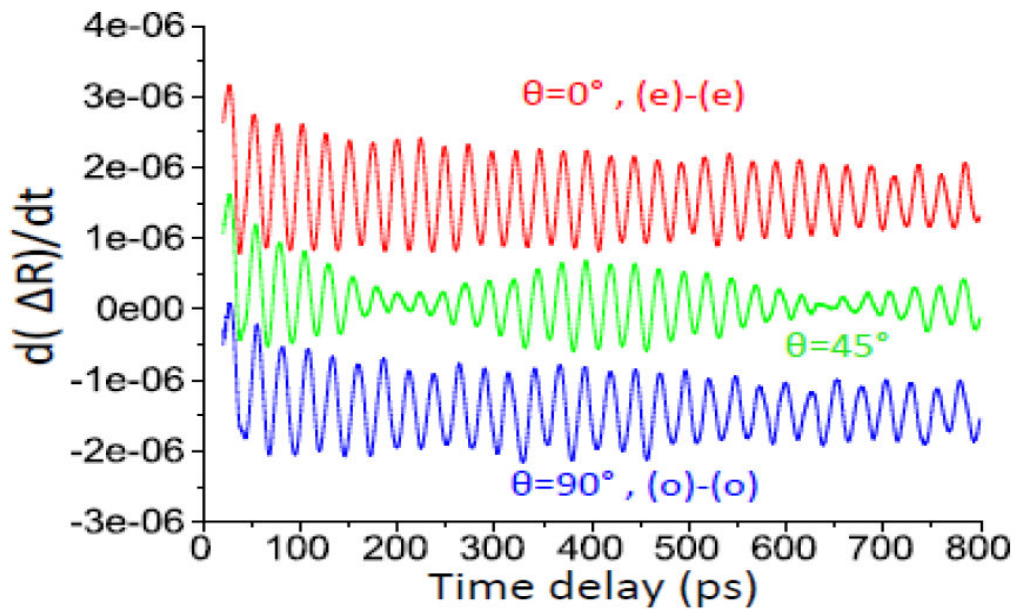


Fig. 4.29. Comparison of derivatives of signal obtained by different probe polarizations.

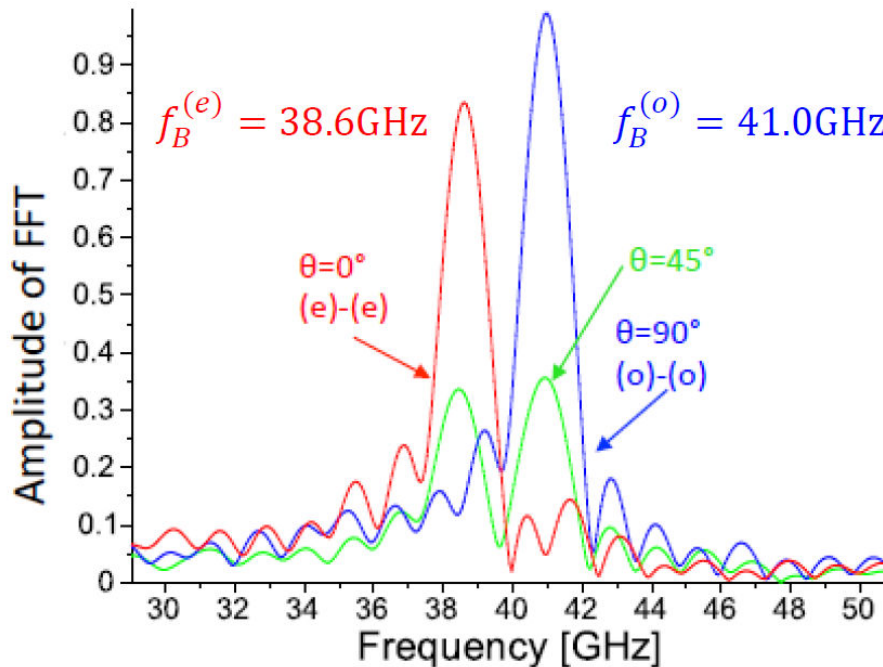


Fig. 4.30. Frequencies of LA phonons detected by different orientations of probe polarization.

The most important fact is that, whatever the probe polarization, there is no mode conversion effect in the detected frequencies. Total lack of central frequency means that mode conversion process does not take place or it is so weak to be detected in this crystal orientation. The only detected Brillouin frequencies ((e)-(e) and (o)-(o) processes) are about

38.6 GHz and 41GHz for probe with extraordinary and ordinary polarization respectively. This gives value of Brillouin frequencies ratio about 1.062, which is very close to expected ratio (Eq. 4.23) obtained with tabulated refractive indices (~1.06).

4.5. Calculations of detected light intensity changes by different scattering processes in simple geometries

We have revealed for the first time some original photoelastic coupling in the time-resolved Brillouin process. In particular, the effect of light mode conversion is a physical mechanism that seems to exist in the two ferroelectric materials (BFO and LNO) while in calcite, this effect does not seem to exist. We cannot directly link this original property to the ferroelectrics yet, but the following calculations, indicate that there is a necessary property concerning the photoelastic coefficient that both BFO and LNO must have while calcite does not have.

To reproduce behavior of detected amplitudes from different scattering processes in function of applied probe polarization orientation (θ) and especially existence or not of mode conversion effect, classical electrodynamics was applied to calculate the light intensity (I) collected on the photodetector. It was done for simple geometry with optical axis in surface plane and for probe at normal incidence.

By definition, intensity of light is the square modulus of the light electric field E which is composed of the summation of a reflected electric field ($r\vec{E}_i$) and of a scattered electric field ($d\vec{E}_s$), therefore $I \sim (r\vec{E}_i + d\vec{E}_s)^2$, where \vec{E}_i -incident electric field, r -reflection coefficient, $d\vec{E}_s$ -electric field scattered by acoustic phonons. The only low frequency signal coming from this term which could be time resolved by photo detector and which corresponds to the light modulation in form of so-called Brillouin oscillations is proportional to $dI \sim r\vec{E}_i \cdot d\vec{E}_s$. When optical axis is parallel to surface and probe is at normal incidence, incident light (electric field) can be decomposed into ordinary (polarization normal to the optical axis) and extraordinary (with polarization along the axis) part and written in scalar notation. Incident ordinary component of electromagnetic wave is:

$$E_i^{(o)} = E_i \sin(\theta) \quad \text{Eq. 4.24}$$

And extraordinary is:

$$E_i^{(e)} = E_i \cos(\theta) \quad \text{Eq. 4.25}$$

for θ – angle between orientation of polarization of probe light and optical axis

Then component reflected from the surface polarized perpendicularly to z-axis will be:

$$E_r^{(o)} = r_o E_i^{(o)} = \frac{1-n_o}{1+n_o} E_i^{(o)} = \frac{1-n_o}{1+n_o} E_i \sin(\theta) \quad \text{Eq. 4.26}$$

And respectively component reflected from the surface polarized along with z-axis will be:

$$E_r^{(e)} = r_e E_i^{(e)} = \frac{1-n_e}{1+n_e} E_i^{(e)} = \frac{1-n_e}{1+n_e} E_i \cos(\theta) \quad \text{Eq. 4.27}$$

where: $r_i = \frac{1-n_i}{1+n_i}$ – reflection coefficient for given polarization state

So as it is visible, birefringence makes reflection of light more complex even for one of the simplest geometry (the simplest one is with optical axis normal to surface, when light sense only ordinary refractive index). Situation for reflection would be much more complex for inclined optical axis or incident probe beam.

Also description of electric field of backscattered light in this configuration becomes even more complex. It is because light participating is scattering process, first is transmitted to medium with given transmission coefficient, then is scattered by acoustic phonons what is governed by photoelastic coefficient and finally it is retransmitted from the medium to the detector to interfere with reflected light.

The transmission coefficient is:

$$t = 1 + r \quad \text{Eq. 4.28}$$

So transmitted to the birefringent medium polarization components will be:

$$E_t^{(o)} = t_o E_i^{(o)} = \frac{2}{1+n_o} E_i \sin(\theta) \quad \text{Eq. 4.29}$$

$$E_t^{(e)} = t_e E_i^{(e)} = \frac{2}{1+n_e} E_i \cos(\theta) \quad \text{Eq. 4.30}$$

This transmitted wave if subsequently scattered on LA phonons. Brillouin scattering is governed by an acoustically induced changes in dielectric tensor ε_{ij} , which are controlled by acousto-optic effect. Magnitude of scattering is determined by the elasto-optic tensor p_{ijkl} by relation:

$$\Delta\varepsilon_{ij} = p_{ijkl} \eta_{kl} \quad \text{Eq. 4.31}$$

where: p_{ijkl} – elasto-optic tensor

η_{kl} – strain field

This elasto-optic tensor for -3m point group of BFO and LNO has in contracted version form:

$$p_{ij} = \begin{bmatrix} p_{11} & p_{12} & p_{13} & p_{14} & 0 & 0 \\ p_{12} & p_{11} & p_{13} & -p_{14} & 0 & 0 \\ p_{31} & p_{31} & p_{33} & 0 & 0 & 0 \\ p_{41} & -p_{41} & 0 & p_{44} & 0 & 0 \\ 0 & 0 & 0 & 0 & p_{44} & p_{11} \\ 0 & 0 & 0 & 0 & P_{11} & p_{66} \end{bmatrix} \quad \text{Eq. 4.32}$$

It should be mentioned that this tensor is not symmetric. Besides it has totally 8 independent parameters and some null components.

To remind, in the geometry in which optical axis (z-axis) is in plane and x-axis is normal to plane (case of x-cut of crystal) extraordinary polarization of light is along z-axis and ordinary

polarization is along y-axis of crystal. In this geometry different scattering process are governed by following elements of dielectric tensor (which are in the end expressed in contracted notation):

- Normal (o)→(o) scattering is described by $\Delta\varepsilon_{yy} = \Delta\varepsilon_{22} = \Delta\varepsilon_2$,
- Normal (e)→(e) scattering is described by $\Delta\varepsilon_{zz} = \Delta\varepsilon_{33} = \Delta\varepsilon_3$,
- Mode conversion (o)→(e), or (e)→(o) is described by $\Delta\varepsilon_{yz} = \Delta\varepsilon_{zy} = \Delta\varepsilon_4$.

In considered geometry the photo generated QLA (quasi-longitudinal) wave could contain only longitudinal component of strain $\eta_1 = \frac{\partial u_x}{\partial x}$ and shear component of strain $\eta_6 = \frac{\partial u_y}{\partial x}$. Therefore possible changes of dielectric coefficients are:

$$\Delta\varepsilon_{yy} = \Delta\varepsilon_2 = p_{21} \frac{\partial u_x}{\partial x} + p_{26} \frac{\partial u_y}{\partial x} = p_{12} \frac{\partial u_x}{\partial x}, \text{ as } p_{26} = 0 \quad \text{Eq. 4.33a}$$

$$\Delta\varepsilon_{zz} = \Delta\varepsilon_3 = p_{31} \frac{\partial u_x}{\partial x} + p_{36} \frac{\partial u_y}{\partial x} = p_{31} \frac{\partial u_x}{\partial x}, \text{ as } p_{36} = 0 \quad \text{Eq. 4.33b}$$

$$\Delta\varepsilon_{yz} = \Delta\varepsilon_{zy} = \Delta\varepsilon_4 = p_{41} \frac{\partial u_x}{\partial x} + p_{46} \frac{\partial u_y}{\partial x} = p_{41} \frac{\partial u_x}{\partial x}, \text{ as } p_{46} = 0 \quad \text{Eq. 4.33c}$$

These calculations demonstrate that in this particular geometry Brillouin scattering with mode conversion can takes place due to $p_{41} \neq 0$ in BFO and LNO. What is more this scattering is due to longitudinal component of QLA mode only (shear does not contribute in this case).

It can be assumed that scattered light in particular scattering process is proportional to change of corresponding dielectric coefficients induced by LA strain, detected change of intensity of light can be written for independent scattering processes. We detail the calculation for the four Brillouin processes for this geometry (X-cut). Detected change of intensity for ordinary light scattered to ordinary (o)→(o) is proportional to:

$$dI_o \sim (t_{01}^{(o)} E_y p_{21} t_{10}^{(o)}) r_o E_y \quad \text{Eq. 4.34}$$

where: $t_{01}^{(o)} = 1 + r_o$ – transmission coefficient (from air to medium) for ordinary component

$t_{10}^{(o)} = 1 - r_o$ – retransmission coefficient (from medium to air) for ordinary component

r_o – reflection coefficient for ordinary component

To remind, electric field in y direction is in this geometry ordinary component of incident electric field of probe light so it can be written as: $E_y = E_i^{(o)} = E_i \sin(\theta)$. Therefore change of intensity in o-o process can be written in final form as:

$$dI_o \sim (1 - r_o^2) r_o p_{21} E_i^2 \sin^2 \theta \sim p_{21} I \sin^2 \theta \quad \text{Eq. 4.35}$$

Similarly, the change of intensity for e-e process is proportional to:

$$dI_e \sim (t_{01}^{(e)} E_z p_{31} t_{10}^{(e)}) r_e E_z \sim (1 - r_e^2) r_e p_{31} E_i^2 \cos^2 \theta \sim p_{31} I \cos^2 \theta \quad \text{Eq. 4.36}$$

Both formulas properly predict π periodicity of detected amplitudes for detected ordinary and extraordinary components. Both have also one 0 and one maximum position in period. Moreover they are shifted by $\pi/2$ relative to each other. Therefore obtained formulas reproduce well the observed dependences of detected amplitudes from normal scattering processes for variable probe polarizations (see Figs. 4.8, 4.9 and 4.22). What is more detected amplitudes are proportional to proper elasto-optic coefficients so their values can give additional confirmation of obtained results, at least qualitative.

Finally change of intensity corresponding to mode conversion processes o-e and e-o is proportional to:

$$dI \sim \left(t_{01}^{(o)} E_y p_{41} t_{10}^{(e)} \right) r_e E_z + \left(t_{01}^{(e)} E_z p_{41} t_{10}^{(o)} \right) r_o E_y \sim p_{41} [t_{01}^{(o)} t_{10}^{(e)} r_e + t_{01}^{(e)} t_{10}^{(o)} r_o] E_i^2 \sin \theta \cos \theta \sim p_{41} [(1+r_o)(1-r_e)r_e + (1+r_e)(1-r_o)r_o] E_i^2 \sin(2\theta) \sim p_{41} I \sin(2\theta) \quad \text{Eq. 4.37}$$

First of all, this formula is based on the following processes: ordinary component is transmitted to medium, then it can be converted to extraordinary component which is then retransmitted and finally interfere with extraordinary component of reflected light. The same explanation is valid by analogy for the incident extraordinary light component. The angle (θ) dependence of the amplitude of mode conversion Brillouin mode is also π periodic. However, it has 2 zeros in one period and can be both positive as negative, what means change of phase of detected oscillations which was clearly observed. When it comes to absolute value of amplitude change it becomes function with period $\pi/2$ what can be also noticed on plot of absolute value of amplitude from mode conversion process.

To compare observed amplitudes of Brillouin oscillations from different scattering processes with corresponding elasto-optic coefficients it is presented table with reported values for LNO.

MATÉRIAUX	p_{11}	p_{12}	p_{21}	p_{22}	p_{13}	p_{31}	p_{33}	p_{23}	p_{32}	p_{14}	p_{41}	p_{44}	p_{45}	p_{55}	p_{16}	p_{61}	p_{66}	RÉF.
Silice (isotrope)	0,121	0,270	p_{12}	p_{11}	p_{12}	p_{12}	p_{11}	p_{12}	p_{12}	0	0	[-0,075]	0	p_{44}	0	0	p_{44}	[5]
α -HIO ₃ (222) ..	0,406	0,277	0,279	0,343	0,304	0,503	0,334	0,305	0,310	0	0	—	0	—	0	0	0,092	[6]
PbMoO ₄ (4/m) .	0,24	0,24	p_{12}	p_{11}	0,255	0,175	0,300	p_{13}	p_{31}	0	0	0,067	-0,01	p_{44}	0,017	0,013	0,05	[14] chap.4 [7]
TiO ₂ (4/mmm) ..	0,011	0,172	p_{12}	p_{11}	0,168	0,096	0,058	p_{13}	p_{31}	0	0	—	0	p_{44}	0	0	—	[7]
TeO ₂ (422)	0,007	0,187	p_{12}	p_{11}	0,340	0,090	0,240	p_{13}	p_{31}	0	0	-0,17	0	p_{44}	0	0	-0,046	[8]
LiNbO ₃ (3m) ..	0,036	0,072	p_{12}	p_{11}	0,092	0,178	0,088	p_{13}	p_{31}	0,07(*)	0,155	—	0	p_{44}	0	0	[-0,018]	[7]
LiTaO ₃ (3m) ..	0,080	0,080	p_{12}	p_{11}	0,094	0,086	0,150	p_{13}	p_{31}	0,031	0,024	0,022	0	p_{44}	0	0	[0,00]	[7]
Quartz α (32) ..	0,138	0,250	p_{12}	p_{11}	0,259	0,258	0,098	p_{13}	p_{31}	-0,029	-0,042	-0,068	0	p_{44}	0	0	[-0,056]	[9]

(*) Valeur déterminée par J. REINTJES and M. B. SCHULZ. — *J. Appl. Phys.*, 39, 5254 (1968).
 Les valeurs entre crochets sont égales à $\frac{p_{11} - p_{12}}{2}$.

Table 4.2. : some tabulated photoelastic coefficients.

It is worth to notice that the p_{31} of LNO is nearly 3 times larger than the p_{21} . This indicates that the Brillouin scattering must be 3 times larger for the (e)-(e) process (Eq. 4.36) than for

the (o)-(o) process. This value is significantly smaller than the experimental observation since we got a ratio of around 5 (comparison of blue and red curves in Fig. 4.21). Moreover, the values given in the above table, shows that the mode-conversion process is also efficient since p_{41} is similar to p_{31} .

As a final discussion of this theoretical approach, a similar calculation can be performed for the Y-cut geometry. In that case the relevant photoelastic coefficient is the p_{51} involved in the relevant disturbed dielectric constant $\Delta\epsilon_{yz}$. In the case of BFO and LNO, for symmetry reasons, this $p_{51} = 0$ which confirms the observations. For the case of calcite, because the crystal is inclined, the general calculation (shown in appendix 3) is more complex but we can show that the mode conversion is expected to be negligible because the p_{41} photoelastic coefficient is about 10 times smaller than that of LNO [72] and probably than that of BFO.

4.6 Conclusion

Optical detection of light back-scattered on acoustic phonons in particularly oriented birefringent ferroelectrics (BFO, LNO) revealed very efficient conversion of polarization state of scattered light (ordinary to extraordinary or the inverse). Observation of this process was obtained by detection up to 3 Brillouin frequencies in time-resolved picosecond interferometry technique, as never reported up to now. In calcite, which is classical birefringent material, there was no detection of optical mode conversion. The mode conversion is very sensitive to crystallographic orientation of studied material, since it exists only for X cut for LNO while no effect was observed for the Y and Z-cut (for the normal or nearly normal incidence of probe beam). A model of photoelastic detection was developed for the particular detection geometry (but could be generalized in the future). This model underlines that a large elasto-optic coefficient p_{41} is required to see this mode-conversion process. The absence of such mode conversion for calcite is most likely connected to smallness of coefficient p_{41} for this material compared to that of LNO. Our findings indicate then that BFO could have elasto-optic coefficient as large as those of LNO. This information is all the more important than the elasto-optic (photoelastic) coefficient of BFO are currently unknown.

As potential applications, the process of mode conversion could be very important for ultrafast manipulation of light polarization by coherent acoustic phonons. Moreover ultrafast experiments revealed favorable conditions for emergence of this phenomenon, what can simplify applied realizations of this interesting process at the interface of phononic and photonic disciplines.

Chapter 5. General Conclusion and perspectives

Studies by pump-probe spectroscopy, and in particular by picosecond acoustics technique, revealed that BFO is very interesting material both from generation and detection point of view. Prominent ferroelectricity and anisotropy of this material together make it special and unique for generation and detection of optically induced coherent acoustic phonons.

Just to summarize and to generalize, proper crystallographic orientations of BFO with axis of crystal inclined with respect to surface normal leads to efficient generation of shear acoustic phonons by optical excitation: a theoretical model indicates that 45° should be the best one. We only studied crystal with orientation around 30° . This unique property comes from a broken symmetry of crystallites which, according to our analysis, is related to the internal polarization of ferroelectric BFO which leads to an efficient inverse piezoelectric mechanism. Moreover, by selecting some crystallographic orientation (selection of some grains in a polycrystalline sample) it is possible to manipulate acoustic spectrum of emitted phonons. Such capabilities make BFO as a good candidate for optically triggered versatile GHz coherent acoustic phonons sources. These results have been published in 2014 in *Nature Communications* [60].

Furthermore, optical birefringence of BFO with unique elasto-optic properties lead to optical mode conversion of probe light scattered on longitudinal acoustic phonons, *i.e.* conversion of ordinary polarization state of probe light into extraordinary and vice versa. This mode-conversion was known in classical Brillouin spectroscopy but was never reported in time-domain spectroscopy so far. This effect was confirmed for another ferroelectric material LiNbO_3 (LNO), which is widely applied in laser physics and photonics as optical modulator for example. Our findings suggest another application of LNO and possibly BFO in ultrafast light modulation by coherent phonons. Effect of mode conversion is relatively efficient for both materials, but still it is possible to enhance it. One perspective is for example to match frequency spectrum of generated acoustic phonons by sequence of exciting pulses, to enhance scattering process with mode conversion.

It is worth to mention that a lot of tensorial parameters of BFO like piezoelectric coefficients, or elasto-optic constants are not fully well known. As a matter of fact, there is a need now to measure these values in good quality sample and with higher precision in order to further evaluate quantitatively these rich properties discussed in this manuscript.

To study more mechanisms of generation it is possible to conduct experiments on thin films of BFO with applied electric fields. This would allow the deep understanding of the dynamics of photoexcited electrons, and evaluate better the role of ferroelectric domains and light induced piezoelectric mechanism of acoustic generation. Moreover it would be worth to realize broadband detection of acoustic spectrum emitted from different crystallographic orientations (grains) of polycrystalline BFO sample, as for now it was only obtained narrowband detection by measurements of Brillouin oscillations. To do that, it would be necessary to probe BFO by weakly penetrating blue light, or to cover it by thin film of material in which it would be possible to detect profile of acoustic strain emitted from BFO. In principle it would be also possible to study strain generated in different BFO grains by

TRXRD experiment, with a special focus, if possible, on the shear strain. It could show directly lattice motion induced by light excitation from different crystallographic orientations.

Finally results obtained on both BFO and LNO show that there is great potential in optically anisotropic ferroelectrics. Ferroelectricity makes dynamics of electrons and their coupling with lattice much richer and stronger than in another materials like metals, or semiconductors. On the other side anisotropy leads to more complex interactions with light, and subsequent coupling of electrons with lattice. Consequently, this provides a diversity and richness of physical phenomena, interactions and running processes. Therefore it is really worth to explore interaction of pulsed laser light, induced electron dynamics and generation of high frequency phonons in another materials, or structures with both ferroelectric and anisotropic properties.

Appendix 1: Pump-probe setup characteristics

In this subpart, we give some details about the setup used during these researches and for which results will be presented in Chapter 3 and 4.

In the Fig. App1.1 the scheme of the complete optical setup is given. Beam from aperture of femtosecond laser is first divided by polarizing beam splitter (BS) into two beams. Separation with desired intensities can be accomplished thanks to selection of polarization of light by half-plate. Red beam directed to EOM (electro-optic modulator) is called pump beam. Beam directed to OPO (optical parametric oscillator) and presented as green is called probe beam. Pump beam after modulation goes through barium borate (BBO) crystal for second harmonic generation (SHG). Light is focused in crystal by proper lens for better efficiency of conversion and after it is defocused. It gives light with doubled frequency, so also with doubled energy of photons necessary to efficiently excite studied sample. For the purpose of experiment light with wavelength 800nm or 830nm (depending on experimental configuration) was converted to 400nm, or 415nm, what corresponds to photon energies about 3.1eV and 3.0eV, respectively.

Pump pulse excites sample and in this way changes its optical properties such as reflectivity. Probe pulse is reflected from the sample and experiences change of reflectivity caused by pump pulse. Then it is detected by photodiode and compared with reference signal. Time of coming of probe pulses is changed continuously relative to pump pulse by delay line.

The beam coming out from OPO at higher frequency is called signal and in experiment it was used as probe beam. The main advantage of such source is its tunability. OPO used in experiment was able to generate efficiently probe beam wavelengths from 550nm to 650nm which corresponds to probe photon energies in the range 1.91eV-2.26eV. To choose desirable wavelength it was necessary to slightly change cavity settings and select temperature of crystal at which nonlinear process was most efficient and stable.

Beam generated by OPO (green in scheme) was separated by beam splitter into two beams. One was directed to photodiode and served as reference beam. Second was focused on sample surface and after reflection returned by similar way and finally was directed to second photodiode. Beam incident on photodiodes were converted into electrical signals, which were balanced and compared. Signal resultant from photodiode was sent to lock-in amplifier where it was demodulated and analyzed.

Pump beam was first directed to electro-optical modulator (EOM). It was modulating amplitude of pump beam with frequency given by lock-in amplifier (during experiment it was 80 kHz). Modulation of pump is necessary to efficiently recover final signal from probe. As excitation given by pump pulse influence on probe reflection, modulation of it is also imprinted in probe signal. Modulation frequency is given to pump beam by lock-in amplifier

and then is used in demodulation of signal given by probe beam. Therefore it is possible to notice that in detection process is applied some kind of loop with feedback. All procedure is mathematically quite complicated and belongs to electric signal processing. Everything is realized by lock-in amplifier – advanced electronic device.

Very important part of pump-probe experiment is delay line. It is simply mirror whose position can be controlled with high precision. In this way optical path of one beam can be elongated, or shortened. Movement of delay line is controlled by computer. Idea is to make probe pulse retarded relative to pump pulse. Thanks to this it can be registered time evolution of probe reflectivity during and after excitation by pump pulse. Typically delay line is located on the way of probe beam. But in this experiment optical path is strongly elongated by OPO cavity so the delay line is positioned on the way of pump beam. In this case, when optical path of pump beam is shortened by delay line the probe pulse is effectively retarded relative to pump pulse. Selecting range of delay line movement it can be chosen range of delay times in which sample is probed after excitation. The delay time is simply time that light takes to travel round trip through reflection from moved mirror.

Very significant question is overlapping of pump and probe beams incident onto the sample surface. In conducted experiment sample was pumped and probed mainly at front side in perpendicular configuration. What is more, after reflection probe beam had to follow back in the same direction. Pump and probe beams were joined together at final stage before focusing on sample surface. It was realized by dichroic mirror, or polarizing beam splitter. In point where both beams came together from perpendicular directions, pump beam was transmitted and probe was reflected perpendicular. Therefore after that both beams were overlapped and propagated in the same direction to be directed on sample surface. Both beams had to be overlapped as well as possible to get all probe beam influenced by pump. Moreover cross section of probe incident on sample surface should be smaller than cross section of pump beam. So finally both beams had to be centered on sample surface with proper sizes.

Final case is to remove pump beam from detection after reflection from sample, as desired information gives only probe beam modulated by pump and to lead reflected probe beam only to second photodiode. This is realized by different optical methods such as perpendicular polarization of pump and probe beam, use of half and quarter plate to have proper transmission or reflection on beam splitters. Eventually to be sure that only probe signal is detected, there are applied two filters before photodiodes to cut off all unwanted and harmful light.

Some parameters of pulsed laser light

To get some idea and notion about pulsed laser radiation let us calculate some values of parameters of pulsed light. There will be shown calculations for femtosecond laser used in pump-probe experiments whose results are presented in this manuscript. In most of realized experiments it was used femtosecond Ti:sapphire laser named Chameleon, which can generate pulsed light at wavelengths between 700nm and 830nm. Main parameters of this

laser are following: averaged power (P_{av}) is about 3200mW, duration of generated pulse (τ_p) is 200fs (2×10^{-13} s) and pulse repetition rate (f_r) is 80MHz (what means that it generates 80 million pulses per second). These values allows to calculate other very important parameter of laser pulses. As power 3200mW means energy 3200mJ of 80 million pulses per second, so energy of single pulse can be calculated simply:

$$E_p = \frac{P_{av}}{f_r} = \frac{3200mW}{80MHz} = \frac{3200 \cdot 10^{-3}W}{80 \cdot 10^6Hz} = 40 \cdot 10^{-9}J = 40nJ$$

Obtained value of energy of single pulse directly from laser may seem very small, but when pulse is very short such energy is significant for interaction with matter. More relevant parameter is power of single pulse, which means at which rate energy of light is deposited into excited matter:

$$P_p = \frac{E_p}{\tau_p} = \frac{40nJ}{200fs} = \frac{40 \cdot 10^{-9}J}{200 \cdot 10^{-15}s} = 2 \cdot 10^5W = 200kW$$

Even for such laser with relatively low average power for which energy of pulse is very small, power of single pulse is quite high (much higher than for example total power of typical household). It is only because of extremely short duration of laser pulse. Another important parameter is intensity of laser pulse. According to definition, intensity of light is power per irradiated area. To calculate it, value of area of irradiation is necessary. Typically in experiment laser light was focused on sample surface to the diameter about $10\mu m$. So roughly area on which energy of light is deposited is about $100 \mu m^2$ ($10^{-10}m^2$). This allows to calculate approximately intensity given by single pulse when it is focused:

$$I = \frac{P_p}{A} \cong \frac{200kW}{100\mu m^2} = \frac{2 \cdot 10^5W}{10^{-10}m^2} = 2 \cdot 10^{15} \frac{W}{m^2}$$

So it is enormous when energy of single pulse is focused on tiny surface. Even the more important parameter is fluence of laser pulse, which tells how much energy is deposited per area by single pulse of light:

$$F_p = \frac{E_p}{A} = \frac{40nJ}{100\mu m^2} = \frac{40 \cdot 10^{-9}J}{10^{-10}m^2} = 400 \frac{J}{m^2} = 40 \frac{mJ}{cm^2}$$

It is converted in the end to (mJ/cm^2), which is more traditional unit of fluence used in pump-probe technic. It is necessary to remember that these values are valid for laser pulses emitted directly from laser aperture (for maximum output of laser). Both intensity and fluence depend on how strong finally light was focused on the sample surface. Typical power of exciting light (which was directly measured in front of sample during experiment by power meter) applied in experiments directly on samples was of the order of 1mW (especially blue second harmonic), so several thousand times smaller than initial power of laser. All the calculated parameters of light scales by the same factor as power, therefore energy, power, intensity and fluence of pulse were typically several thousand times smaller, what corresponds to energy of pulse of the order of pJ, power tens of watts, and fluence about $10\mu J/cm^2$. Such difference in values of parameters of pulse directly from laser and incident on sample is because light was first divided into two parts and then in most of the situations one part was converted by second harmonic generation (SHG) and another by optical

parametric process to other wavelengths (energies of photons). As efficiency of both processes is not very high, only portion of incident energy was converted into desired light.

Duration of pulse	200fs
Operating wavelength	775nm
Averaged power	3200mW
Pulse repetition rate	80MHz
Energy of single pulse	40nJ
Power of single pulse	200kW

Table App1.1 : Basic parameters of femtosecond laser used in experiment.

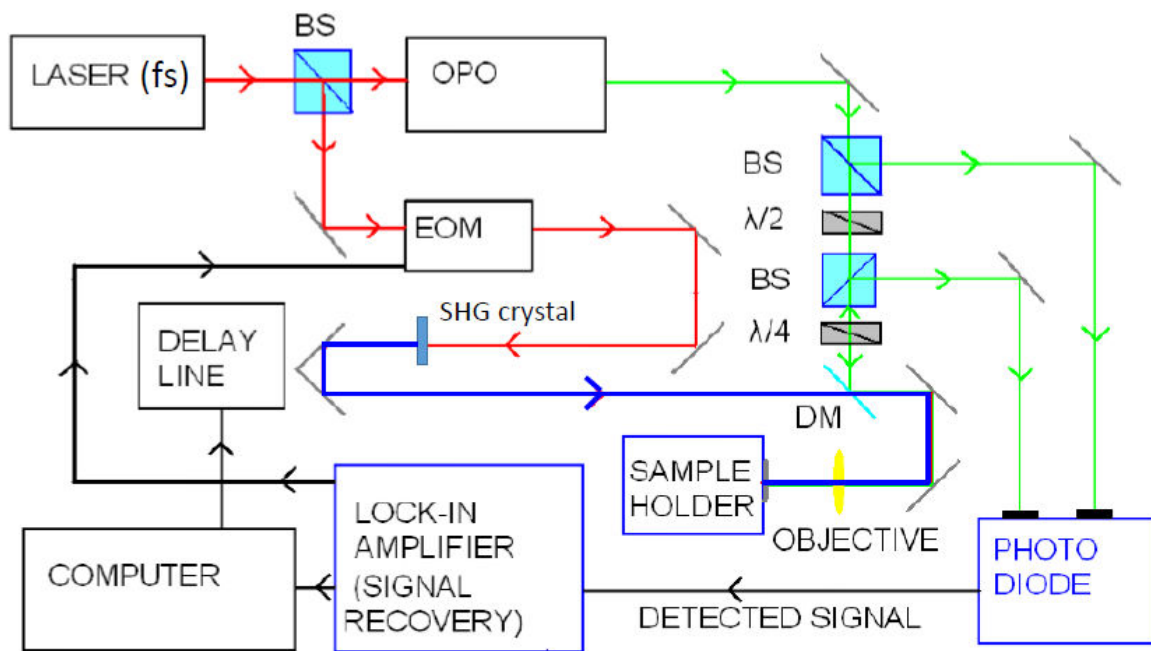


Fig. App1.1: scheme of the two-color pump-probe setup used at IMMM (Le Mans).

Appendix 2: Grain orientation probed by optical birefringence

In this appendix, we show how it is possible to probe locally (with a probe beam) the crystallographic orientation of a grain in a polycrystalline sample by analysing the effect of the optical birefringence on the time-resolved Brillouin signal.

We remind that BFO is an uniaxial medium (see part 2.4.3) and have two refractive indexes, ordinary (n_o) and extraordinary (n_e), equal to about 2.85 and 2.65 respectively at wavelength 800nm [41]. Ordinary refractive index is valid for polarization of light perpendicular to optical axis, and extraordinary for polarization along optical axis (optical axis along the [111] direction in the rhombohedral symmetry). When the probe light is composed of two components (ordinary and extraordinary), it leads to a split Brillouin peak with two components (there is also the detection of the mode conversion discussed in chapter 4 but not useful to extract the grain orientation)

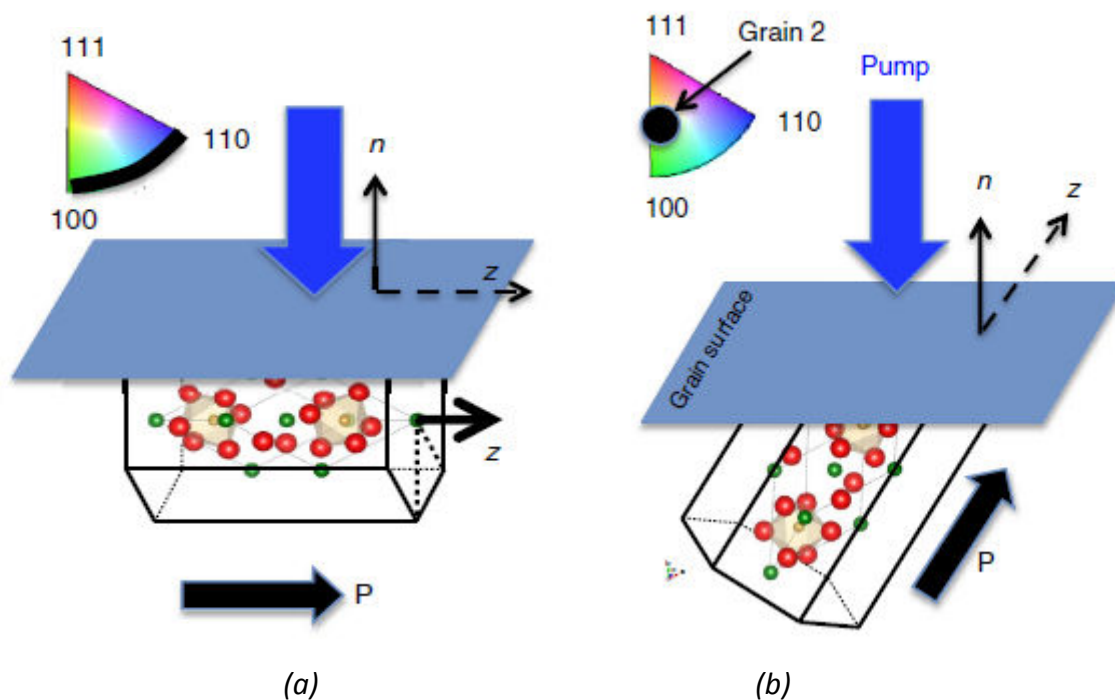


Fig. app2.1 : (a) Picture of grain with crystallographic axis, optical axis and ferroelectric polarization in surface plane (all these features have the same orientation, perpendicular to incident probe beam) revealing strongest effect of optical birefringence. (b) Picture of grain with arbitrary direction of axis with respect to normal to surface plane.

In case of arbitrarily oriented grain (random crystallographic orientation) birefringent medium can be optically characterised by effective extraordinary refractive index, which can be calculated by the following formula [35]:

$$n_{eff}^2(\theta) = \frac{n_o^2 n_e^2}{n_o^2 \sin^2\theta + n_e^2 \cos^2\theta} \quad \text{Eq. app2.1.}$$

where: θ – angle between optical axis and direction of propagation of light (normal to surface)

It can be realized that this formula gives in the limits either ordinary refractive index for the light propagating along the optical axis ($\theta=0^\circ$), or extraordinary refractive index for the light propagating perpendicularly to the optical axis ($\theta=90^\circ$). Therefore it can be concluded that value of effective extraordinary refractive index is between ordinary and extraordinary one. This formula can be reformulated into formula for angle of inclination of optical axis when ratio of ordinary refractive index to extraordinary one and ordinary to effective extraordinary refractive index are known simultaneously.

$$\sin \theta = \sqrt{\frac{\left(\frac{n_o}{n_{eff}}\right)^2 - 1}{\left(\frac{n_o}{n_e}\right)^2 - 1}} \quad \text{Eq. app2.2}$$

As values of ordinary and extraordinary refractive indices are quite close, ratio of both is quite close to unity. Therefore such formula can be simplified:

$$\sin \theta = \sqrt{\frac{\left(\frac{n_o}{n_{eff}}+1\right)\left(\frac{n_o}{n_{eff}}-1\right)}{\left(\frac{n_o}{n_e}+1\right)\left(\frac{n_o}{n_e}-1\right)}} \cong \sqrt{\frac{\left(\frac{n_o}{n_{eff}}-1\right)}{\left(\frac{n_o}{n_e}-1\right)}} \quad \text{Eq. app2.3}$$

Component of Brillouin frequency corresponding to the effective extraordinary refractive index can be expressed by formula:

$$f_{B\ eff} = \frac{2n_{eff}v}{\lambda} \quad \text{Eq. app2.4}$$

Therefore ratio of effective extraordinary refractive index to ordinary one is simply equal to the ratio of detected frequencies.

$$\frac{n_o}{n_{eff}} = \frac{f_{Bo}}{f_{B\ eff}} \quad \text{Eq. app2.5}$$

So finally it can be concluded that measurement of Brillouin frequency split components allows evaluation of the inclination of optical axis of studied grain 6 (Fig. app2.2). From presented results, frequencies of LA mode components are 49.7GHz and 50.6GHz, respectively for extraordinary and ordinary components. Therefore ratio of ordinary to effective ordinary refractive index is about $n_o/n_{eff} \approx 1.018$. Assuming that ratio of ordinary to extraordinary refractive index is about 1.08 (which indicates level of birefringence of BFO) based on previous results, it is possible to calculate angle of orientation of optical axis versus normal to surface.

$$\sin \theta = \sqrt{\frac{\left(\frac{n_o}{n_{eff}}-1\right)}{\left(\frac{n_o}{n_e}-1\right)}} \cong \sqrt{\frac{(1.018-1)}{(1.08-1)}} = \sqrt{\frac{0.018}{0.08}} \cong \sqrt{0.225} \cong 0.47 \quad \text{Eq. app2.6}$$

This gives value of angle between optical axis and normal to surface about 28° (Fig. 3.29). It means that for such inclination of optical axis there are crystallographic orientations with also strong and efficient generation of shear mode when compared with longitudinal one. This effect is consistent with the results obtained for grain 2 having an angle of around 24° . It is to be note that when angle approaches small values, the Brillouin splitting becomes small and sometimes the resolution of FFT obtained from direct signal is not enough to distinguish two components.

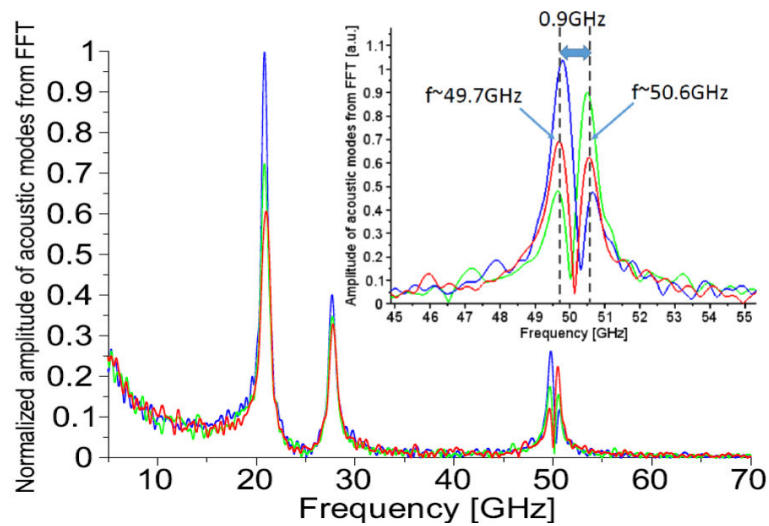


Fig. app2.2. Comparison of spectra with the highest resolution taken from long scans of signals obtained by linear probe polarization rotated relatively only by 5 degrees (grain number 6). In the inset there is clearly visible splitting of LA mode with different amplitude of components for rotated probe polarization.

Appendix 3: Mode conversion in calcite axis oriented at 45 degrees versus surface (rotation of photo-elastic tensor by 45 degrees)

When optical axis is in plane and acoustic propagation along x-axis (propagation and detection normal to the surface) mode conversion of light incident along x-axis can be caused by nonzero $\Delta\varepsilon_{yz}=\Delta\varepsilon_{zy}$. We assume the plane acoustic waves propagating along x therefore $\frac{\partial}{\partial z} = \frac{\partial}{\partial y} = 0$ and in principle we have only 3 possible displacement gradients $\frac{\partial u_x}{\partial x}$, $\frac{\partial u_y}{\partial x}$, $\frac{\partial u_z}{\partial x}$ contributing to the strain. Then

$$\Delta\varepsilon_{yz} = P_{41} \frac{\partial u_x}{\partial x} + P_{45} \frac{\partial u_z}{\partial x} + P_{46} \frac{\partial u_y}{\partial x}$$

Where: P_{41} , P_{45} and P_{46} – components of the photo-elastic tensor in the experimental coordination frame.

When optical axis of the crystal is in surface plane coefficients P_{45} and P_{46} for crystallographic structure of BFO and calcite are equal to 0. So in this case it is predicted only single possibility of mode conversion by $\frac{\partial u_x}{\partial x}$. When polarization is precisely in plane of the surface, only pure longitudinal (LA) mode is excited and $\frac{\partial u_x}{\partial x}$ is present only in this mode, so only LA mode can cause mode conversion.

$$\Delta\varepsilon_{yz} = P_{41} \frac{\partial u_x}{\partial x}$$

For rotation of optical axis by 45 degrees relative to y axis equation describing mode conversion takes form:

$$\Delta\varepsilon_{yz} = \frac{P_{41} - P_{14}}{2\sqrt{2}} \frac{\partial u_x}{\partial x} + \frac{P_{14}}{2\sqrt{2}} \frac{\partial u_z}{\partial x} - \frac{1}{2} \left[P_{44} - \frac{P_{11} - P_{12}}{2} \right] \frac{\partial u_y}{\partial x}$$

In this case rotation of light polarization is possible by all 3 displacements gradients. In particular, if we still assume that one of quasi shear modes is not generated by symmetry principles ($u_y=0$ and $\frac{\partial u_y}{\partial x}=0$), there will be still potential possibility to rotate polarization by both components of both QLA and QTA waves. So if mode conversion is not observed in calcite by QLA wave, this could be because coefficient $\frac{P_{41}-P_{14}}{2\sqrt{2}}$ and transverse component of QLA wave are small. Coefficients P_{41} and P_{14} for calcite are more than 10 times smaller than

other photo elastic coefficients [72], so absence of mode conversion detection is most probably caused by smallness of these coefficients.

Calculation of photo elastic coefficients in rotated system.

General formula for elements of photo elastic matrix:

$$P'_{HK} = M_{HI}M_{KJ}P_{IJ}$$

Where matrix M is a matrix of rotation at given direction and at given angle

Therefore formula for element P'_{41} will be:

$$P'_{41} = M_{4i}M_{1j}P_{ij}$$

$$P'_{41} = M_{41}M_{1j}P_{1j} + M_{42}M_{1j}P_{1j} + M_{43}M_{1j}P_{1j} + M_{44}M_{1j}P_{1j} + M_{45}M_{1j}P_{1j} + M_{46}M_{1j}P_{1j}$$

Matrix of photo elastic coefficients for BFO and calcite has the form:

$$p_{ij} = \begin{bmatrix} p_{11} & p_{12} & p_{13} & p_{14} & 0 & 0 \\ p_{12} & p_{11} & p_{13} & -p_{14} & 0 & 0 \\ p_{31} & p_{31} & p_{33} & 0 & 0 & 0 \\ p_{41} & -p_{41} & 0 & p_{44} & 0 & 0 \\ 0 & 0 & 0 & 0 & p_{44} & p_{11} \\ 0 & 0 & 0 & 0 & P_{11} & p_{66} \end{bmatrix}$$

Matrix of rotation of the system around axis y has the form:

$$M = \begin{bmatrix} \cos^2\eta & 0 & \sin^2\eta & 0 & -\sin 2\eta & 0 \\ 0 & 1 & 0 & 0 & 0 & 0 \\ \sin^2\eta & 0 & \cos^2\eta & 0 & \sin 2\eta & 0 \\ 0 & 0 & 0 & \cos\eta & 0 & \sin\eta \\ \frac{\sin 2\eta}{2} & 0 & -\frac{\sin 2\eta}{2} & 0 & \cos 2\eta & 0 \\ 0 & 0 & 0 & -\sin\eta & 0 & \cos\eta \end{bmatrix}$$

Therefore for rotation angle equal to 45° it will takes values:

$$M = \begin{bmatrix} 1/2 & 0 & 1/2 & 0 & -1/2 & 0 \\ 0 & 1 & 0 & 0 & 0 & 0 \\ 1/2 & 0 & 1/2 & 0 & 1/2 & 0 \\ 0 & 0 & 0 & 1/\sqrt{2} & 0 & 1/\sqrt{2} \\ 1/2 & 0 & -1/2 & 0 & 0 & 0 \\ 0 & 0 & 0 & -1/\sqrt{2} & 0 & 1/\sqrt{2} \end{bmatrix}$$

As it can be noticed coefficients: M_{41} , M_{42} , M_{43} , M_{45} are equal to 0 so equation for photo elastic coefficient P'_{41} in new frame simplifies to:

$$\begin{aligned} P'_{41} &= M_{44}M_{1j}P_{4j} + M_{46}M_{1j}P_{6j} = \\ &= M_{44}[M_{11}P_{41} + M_{12}P_{42} + M_{13}P_{43} + M_{14}P_{44} + M_{15}P_{45} + M_{16}P_{46}] \\ &+ M_{46}[M_{11}P_{61} + M_{12}P_{62} + M_{13}P_{63} + M_{14}P_{64} + M_{15}P_{65} + M_{16}P_{66}] \end{aligned}$$

After taking into account zero coefficients of matrix M and P equation for desired coefficient simplifies to:

$$P'_{41} = \frac{1}{2\sqrt{2}}[P_{41} - P_{14}]$$

Similarly with new coefficient P_{45} :

$$P'_{45} = M_{4I}M_{5J}P_{IJ} = M_{44}M_{5J}P_{4J} + M_{46}M_{5J}P_{6J} = \frac{1}{2\sqrt{2}}P_{41}$$

And new coefficient P_{46} :

$$P'_{46} = M_{4I}M_{6J}P_{IJ} = M_{44}M_{6J}P_{4J} + M_{46}M_{6J}P_{6J} = \frac{1}{2}[-P_{44} + \frac{P_{11} - P_{12}}{2}]$$

Bibliography

- ¹ Aschroft and Mermin, *Solid State Physics*, Saunders College.
- ² R. Merlin, *Generating coherent THz phonons with light pulses*, *Solid State Comm.* **102**, 207 (1997)
- ³ T. Dekorsy, G. Cho, W. Kutt, and H. Kurz, *Light Scattering in Solids VIII*, edited by M. Cardona and G. Gruntherodt (Springer, Berlin, 2000), Vol. 76.
- ⁴ C. Thomsen, H. T. Grahn, H. J. Maris, and J. Tauc, *Surface generation and detection of phonons by picosecond light pulses*, *Phys. Rev. B* **34**, 6 (1986)
- ⁵ V. E. Gusev and A. A. Karabutov, *Laser optoacoustics*, AIP Press, New York (1993)
- ⁶ P. Ruello, and V. E. Gusev, *Physical mechanisms of coherent acoustic phonons generation by ultrafast laser action*, *Ultrasonics* **56**, 21-36 (2015)
- ⁷ T. Saito, O. Matsuda, O. B. Wright, *Picosecond acoustic phonon pulse generation in nickel and chromium*, *PRB* **67**, 205421 (2003)
- ⁸ T. Pezeril, P. Ruello, S. Gougeon, N. Chigarev, D. Mounier, J.-M. Breteau, P. Picart, V. Gusev, *Generation and detection of plane coherent shear picosecond acoustic pulses by lasers: experiment and theory*, *PRB* **75**, 174307 (2007)
- ⁹ O. Matsuda, O. B. Wright, D. H. Hurley, V. E. Gusev and K. Shimizu, *Coherent shear phonon generation and detection with ultrashort optical pulses*, *PRL* **93**, 095501 (2004)
- ¹⁰ T. Pezeril, C. Klieber, S. Andrieu, K.A. Nelson, *Optical generation of gigahertz frequency shear acoustic waves in liquid glycerol*, *PRL* **102**, 107402 (2009)
- ¹¹ D. H. Hurley, O. B. Wright O. Matsuda, V. E. Gusev, O. V. Kolosov, *Laser picosecond acoustics in isotropic and anisotropic materials*, *Ultrasonics* **38**, 470–474 (2000)
- ¹² G. Tas and H. J. Maris, *Electron diffusion in metals studied by picosecond ultrasonics*, *PRB* **49**, 21 (1994)
- ¹³ M. Lejman, V. Shalagatskyi, O. Kovalenko, T. Pezeril, V. Temnov, and P. Ruello, *Ultrafast optical detection of coherent acoustic phonons emission driven by superdiffusive hot electrons*, *J. Opt. Soc. Am. B* **31**, 2 (2014)
- ¹⁴ O. B. Wright, V. E. Gusev, *Ultrafast generation of acoustic waves in copper*, *IEEE Transactions on ultrasonics, ferroelectrics, and frequency control* **42**, 3 (1995)

-
- ¹⁵ M. Perner, S. Gresillon, J. März, G. von Plessen, J. Feldmann, J. Porstendorfer, K.-J. Berg, and G. Berg, *Observation of hot-electron pressure in the vibration dynamics of metal nanoparticles*, PRL **85**, 792 (2000)
- ¹⁶ O. B. Wright and V. E. Gusev, *Acoustic generation in crystalline silicon with femtosecond optical pulses*, APL **66**, 1190 (1995)
- ¹⁷ J.F. Nye, *Physical Properties of Crystals: Their Representation by Tensors and Matrices*, (Oxford University Press, 1957)
- ¹⁸ G. Vaudel, T. Pezeril, A. Lomonosov, M. Lejman, P. Ruello, and V. Gusev, *Laser generation of hypersound by a terahertz photo-Dember electric field in a piezoelectric GaAs semiconductor*, PRB **90**, 014302 (2014)
- ¹⁹ K.-H. Lin, C.-T. Yu, Y.-C. Wen, C.-K. Sun, *Generation of picosecond acoustic pulses using a p–n junction with piezoelectric effects*, APL **86**, 093110 (2005)
- ²⁰ P. Babilotte, P. Ruello, G. Vaudel, T. Pezeril, D. Mounier, J.-M. Breteau, and V. Gusev, *Picosecond acoustics in p-doped piezoelectric semiconductors*, APL **97**, 174103 (2010)
- ²¹ P. Babilotte, P. Ruello, T. Pezeril, G. Vaudel, D. Mounier, J.-M. Breteau, and V. Gusev, *Transition from piezoelectrical generation of hypersound to its generation by deformation potential mechanism with increasing fluence of ultrafast laser action on GaAs*, J. Appl. Phys. **109**, 064909 (2011)
- ²² C.-K. Sun, J.-C. Liang, X.-Y. Yu, *Coherent acoustic phonon oscillations in semiconductor multiple quantum wells with piezoelectric fields*, PRL **84**, 179 (2000)
- ²³ C.S. Kim, J.H. Kim, H. Jeong, Y.D. Jho, H.K. Kwon, H.S. Lee, J.S. Park, K. Song, S.H. Kim, Y.J. Kim, D. Lee, K.J. Yee, *Control of coherent acoustic phonon generation with external bias in InGaN/GaN multiple quantum wells*, APL **100**, 101105 (2012)
- ²⁴ Y.-X. Yan, E. B. Gamble, K. A. Nelson, *Impulsive stimulated scattering: General importance in femtosecond laser pulse interactions with matter and spectroscopic applications*, J. Chem. Phys. **83**, 5392 (1985)
- ²⁵ C. v. Korff Schmising, M. Bargheer, M. Kiel, N. Zhavoronkov, M. Woerner, T. Elsaesser, I. Vrejoiu, D. Hesse, and M. Alexe, *Coupled Ultrafast Lattice and Polarization Dynamics in Ferroelectric Nanolayers*, PRL **98**, 257601 (2007).
- ²⁶ P. Ruello, S. Zhang, P. Laffez, B. Perrin, V. Gusev, *Laser-induced coherent acoustic phonon mechanisms in Metal–Insulator compounds NdNiO₃: thermal and non-thermal processes*, PRB **79**, 094303 (2009)

-
- ²⁷ B. Kundys, *Photostrictive materials*, Appl. Phys. Rev. **2**, 011301 (2015)
- ²⁸ M. Lorenc, Ch. Balde, W. Kaszub, A. Tissot, N. Moisan, M. Servol, M. Buron-Le Cointe, H. Cailleau, P. Chasle, P. Czarnecki, M.L. Boillot, E. Collet, *Cascading photoinduced, elastic, and thermal switching of spin states triggered by a femtosecond laser pulse in an Fe(III) molecular crystal*, PRB **85**, 054302 (2012)
- ²⁹ E. Aksel and J. L. Jones, *Advances in Lead-Free Piezoelectric Materials for Sensors and Actuators*, Sensors **10**, 1935-1954 (2010)
- ³⁰ V. M. Fridkin, *Photoferroelectrics* (Springer, 1979)
- ³¹ J. Kreisel, M. Alexe and P. A. Thomas, *A photoferroelectric material is more than the sum of its parts*, Nat. Mater. **11**, 260 (2012)
- ³² Charlson and Mott, Proc. IEEE **51** (1963) 1239.
- ³³ V. K. Wadhawan, *Introduction to Ferroic Materials* (Gordon and Breach, 2000)
- ³⁴ Brahim Dkhil, Thèse de Doctorat Univ. Pierre et Marie Curie (1999).
- ³⁵ G. Catalan and J. F. Scott, *Physics and Applications of Bismuth Ferrite*, Adv. Mater., **21**, 2463–2485 (2009)
- ³⁶ D. Sando, A. Barthelemy and M. Bibes, *BiFeO₃ epitaxial thin films and devices: past, present and future*, J. Phys.: Condens. Matter **26**, 473201 (2014)
- ³⁷ R. Palai, R. S. Katiyar, H. Schmid, P. Tissot, S. J. Clark, J. Robertson, S. A. T. Redfern, G. Catalan, and J. F. Scott, *β phase and γ - β metal-insulator transition in multiferroic BiFeO₃*, PRB **77**, 014110 (2008)
- ³⁸ T. P. Gujar, V. R. Shinde, C. D. Lokhande, *Nanocrystalline and highly resistive bismuth ferric oxide thin films by a simple chemical method*, Mater. Chem. Phys. **103**, 142 (2007)
- ³⁹ A. Kumar, R. C. Rai, N. J. Podraza, S. Denev, M. Ramirez, Y-H. Chu, L. W. Martin, J. Ihlefeld, T. Heeg, J. Schubert, D. G. Schlom, J. Orenstein, R. Ramesh, R. W. Collins, J. L. Musfeldt, V. Gopalan. *Linear and Nonlinear Optical constants of BiFeO₃*, Appl. Phys. Lett. **92**, 121915 (2008).
- ⁴⁰ B. Gu, Y. Wang, J. Wang, and W. Ji, *Femtosecond third-order optical nonlinearity of polycrystalline BiFeO₃*, Opt. Expr. **17**, 10970 (2009)
- ⁴¹ S. G. Choi, H. T. Yi, S.-W. Cheong, J. N. Hilfiker, R. France, and A. G. Norman, *Optical anisotropy and charge-transfer transition energies in BiFeO₃ from 1.0 to 5.5 eV*, PRB **83**, 100101(R) (2011)

-
- ⁴² J.-P. Rivera, & H. Schmid, *On the birefringence of magnetoelectric BiFeO₃*, *Ferroelectrics* **204**, 23–33 (1997)
- ⁴³ D. Lebeugle, D. Colson, A. Forget, M. Viret, P. Bonville, J. F. Marucco, S. Fusil, *Room-temperature coexistence of large electric polarization and magnetic order in BiFeO₃ single crystals*, *PRB* **76**, 024116 (2007)
- ⁴⁴ A. K. Zvezdin, A. M. Kadomtseva, S. S. Krotov, A. P. Pyatakov, Y. F. Popov, G. P. Vorob'ev, *J. Magn. Mater.* 2006, 300, 224.
- ⁴⁵ M. Bibes, A. Barthélémy, *Towards a magnetoelectric memory*, *Nat. Mater.* **7**, 425 (2008)
- ⁴⁶ R. W. Schoenlein, W. Z. Lin, J. G. Fujimoto and G. L. Eesley, *Femtosecond Studies of Nonequilibrium Electronic Processes in Metals*, *PRL* **58**, 16 (1986)
- ⁴⁷ S. D. Brorson, A. Kazeroonian, J. S. Moodera, D. W. Face, T. K. Cheng, E. P. Ippen, M. S. Dresselhaus and G. Dresselhaus, *Femtosecond room-temperature measurement of the electron-phonon coupling constant λ in metallic superconductors*, *PRL* **64**, 18 (1990)
- ⁴⁸ Z. Jin, Y. Xu, Z. Zhang, G. Li, X. Lin, G. Ma, Z. Cheng and X. Wang, *Structural dependent ultrafast electron-phonon coupling in multiferroic BiFeO₃ films*, *APL* **100**, 071105 (2012)
- ⁴⁹ Y. M. Sheu, S. A. Trugman, Y.-S. Park, S. Lee, H. T. Yi, S.-W. Cheong, Q. X. Jia, A. J. Taylor and R. P. Prasankumar, *Ultrafast carrier dynamics and radiative recombination in multiferroic BiFeO₃*, *APL* **100**, 242904 (2012)
- ⁵⁰ Y. Yamada, T. Nakamura, S. Yasui, H. Funakubo and Y. Kanemitsu, *Measurement of transient photoabsorption and photocurrent of BiFeO₃ thin films: Evidence for long-lived trapped photocarriers*, *PRB* **89**, 035133 (2014)
- ⁵¹ P. Ruello T. Pezeril, V. Avanesyan, G. Vaudel, V. Gusev, I.C. Infante, B. Dkhil *Photoexcitation of gigahertz longitudinal and shear acoustic waves in BiFeO₃ multiferroic single crystal*, *APL* **100**, 212906 (2012)
- ⁵² L. Y. Chen, J. C. Yang, C. W. Luo, C. W. Laing, K. H. Wu, *Ultrafast photoinduced mechanical strain in epitaxial BiFeO₃ thin films*, *APL* **101**, 041902 (2012)
- ⁵³ B. Kundys, M. Viret, D. Colson and D. O. Kundys, *Light-induced size changes in BiFeO₃ crystals*, *Nature Mater.* **9**, 803–805 (2010)
- ⁵⁴ H. Wen, P. Chen, M. P. Cosgriff, D. A. Walko, J. H. Lee, C. Adamo, R. D. Schaller, J. F. Ihlefeld, E. M. Dufresne, D. G. Schlom, P. G. Evans, J. W. Freeland and Yuelin Li, *Electronic Origin of Ultrafast Photoinduced Strain in BiFeO₃*, *PRL* **110**, 037601 (2013)

-
- ⁵⁵ D. Schick, M. Herzog, H. Wen, P. Chen, C. Adamo, P. Gaal, D. G. Schlom, P. G. Evans, Y. Li and M. Bargheer, *Localized Excited Charge Carriers Generate Ultrafast Inhomogeneous Strain in the Multiferroic BiFeO₃*, PRL **112**, 097602 (2014)
- ⁵⁶ S. Gomez-Salces et al., *Effect of pressure on the band gap and the local FeO₆ environment in BiFeO₃*, PRB **85**, 144109 (2012)
- ⁵⁷ D. Daranciang et al., *Ultrafast Photovoltaic Response in Ferroelectric Nanolayers*, PRL **108**, 087601 (2012)
- ⁵⁸ D. S. Rana, K. Takahashi, K. R. Mavani, I. Kawayama, H. Murakami, and M. Tonouchi, *Structural dependence of terahertz radiation from multiferroic BiFeO₃ thin films*, PRB **77**, 024105 (2008)
- ⁵⁹ K. Takahashi, N. Kida, and M. Tonouchi, *Terahertz Radiation by an Ultrafast Spontaneous Polarization Modulation of Multiferroic BiFeO₃ Thin Films*, PRL **96**, 117402 (2006)
- ⁶⁰ M. Lejman, G. Vaudel, I. C. Infante, P. Gemeiner, V. E. Gusev, B. Dkhil & P. Ruello, *Giant ultrafast photo-induced shear strain in ferroelectric BiFeO₃*, Nat. Commun., **5**, 4301 (2014).
- ⁶¹ Y.-C. Wen et al., *Photogeneration of coherent shear phonons in orientated wurtzite semiconductors by piezoelectric coupling*, PRB **80**, 195201 (2009)
- ⁶² Z. Shao, *Refractive indices for extraordinary waves in uniaxial crystals*, Phys. Rev. E **52**, No. 1 (1995)
- ⁶³ A. Devos, J.-F. Robillard, R. Côte, and P. Emery, *High-laser-wavelength sensitivity of the picosecond ultrasonic response in transparent thin films*, PRB **74**, 064114 (2006).
- ⁶⁴ S. L. Shang et al., *Elastic properties of cubic and rhombohedral BiFeO₃ from first-principles calculations*, PRB **80**, 052102 (2009)
- ⁶⁵ N. N. Krainik, N. P. Khuchua, V. V. Zhdanova and V. A. Evseev, *Phase transition in BiFeO₃*, Sov. Phys. Solid State **8**, 654 (1966)
- ⁶⁶ Z. Chen, et al., *Coexistence of ferroelectric triclinic phases in highly strained BiFeO₃ films*, PRB **84**, 094116 (2011)
- ⁶⁷ S. Murakami, et al., *Development of piezoelectric MEMS vibration energy harvester using (100) oriented BiFeO₃ ferroelectric film*, J. Phys. Conf. Ser. **476**, 012007 (2013)
- ⁶⁸ C. Kittel, *Theory of the structure of ferromagnetic domains in films and small particles*, Phys. Rev. **70**, 965 (1946).
- ⁶⁹ J. A. Schneeloch, Z. Xu, J. Wen, P. M. Gehring, C. Stock, M. Matsuda, B. Winn, G. Gu, Stephen M. Shapiro, R. J. Birgeneau, T. Ushiyama, Y. Yanagisawa, Y. Tomioka, T. Ito, and

G. Xu, *Neutron inelastic scattering measurements of low-energy phonons in the multiferroic BiFeO₃*, PRB **91**, 064301 (2015)

⁷⁰ O. Delaire, M. B. Stone, J. Ma, A. Huq, D. Gout, C. Brown, K. F. Wang, and Z. F. Ren, *Anharmonic phonons and magnons in BiFeO₃*, PRB **85**, 064405 (2012)

⁷¹ K. I. Doig, F. Aguesse, A. K. Axelsson, N. M. Alford, S. Nawaz, V. R. Palkar, S. P. P. Jones, R. D. Johnson, R. A. Synowicki, and J. Lloyd-Hughes, *Coherent magnon and acoustic phonon dynamics in tetragonal and rare-earth-doped BiFeO₃ multiferroic thin films*, PRB **88**, 094425 (2013)

⁷² D. F. Nelson, P. D. Lazay and M. Lax, *Brillouin Scattering in Anisotropic Media: Calcite*, Phys. Rev. B, Vol. 6, No. 8 (1972).

⁷³ B. N. Grechushnikov, O.V. Kachalov, N. M. Kreines, M. A. Talalaev, *Mandel'Shtam-Brillouin scattering in calcite*, Soviet Physics JETP **30**, 850 (1970)

⁷⁴ Sandercock, J. R. *Trends in Brillouin-Scattering - Studies of Opaque Materials, Supported Films, and Central Modes. Light Scattering in Solids III*. Recent Results. M. Cardona and G. Guntherodt, Eds. Berlin, Springer-Verlag. 51 173-206 (1982).

⁷⁵ L.I. Mandelstam, *Light Scattering by Inhomogeneous Media*, Zh. Russ. Fiz-Khim., Ova. 58, 381 (1926)

⁷⁶ T. Bienville, and B. Perrin, *Generation and detection of quasi-transverse waves in an anisotropic crystal by picosecond ultrasonics*, Proceedings of the 5th World Congress on Ultrasonics, p813 (2003), unpublished, p. 813, sfa.asso.fr/wcu2003/procs/website/

⁷⁷ A. Boes, D. Yudistira, T. Crasto, H. Steigerwald, V. Sivan, T. Limboeck, J. Friend, S. Mailis, E. Soergel, and A. Mitchell, *Ultraviolet laser induced domain inversion on chromium coated lithium niobate crystals*, Opt. Mater. Express **4**, 241-254 (2014)

⁷⁸ D. E. Zelmon, D. L. Small and D. Jundt, *Infrared corrected Sellmeier coefficients for congruently grown lithium niobate and 5 mol. % magnesium oxide-doped lithium niobate*, J. Opt. Soc. Am. B, Vol. **14**, No. 12 (1997)

⁷⁹ R. S. Weis and T. K. Gaylord, *Lithium Niobate: Summary of Physical Properties and Crystal Structure*, Appl. Phys. A **37**, 191-203 (1985)

⁸⁰ A. R. Hutson and D. L. White, *Elastic wave propagation in piezoelectric semiconductors*, J. Appl. Phys. **33**, No. 1, 40-47 (1962)

⁸¹ J. J. Kyame, *Wave propagation in piezoelectric crystals*, J. Acoust. Soc. Am. **21**, 159-167 (1949)

-
- ⁸² A. W. Warner, M. Onoe, and G. A. Coquin, *Determination of Elastic and Piezoelectric coefficients for Crystals in Class (3m)*, J. Acoust. Soc. Am. **42**, 1223–1231 (1967)
- ⁸³ D. F. Nelson and R. M. Mikulyak, *Refractive indices of congruently melting lithium niobate*, J. Appl. Phys. **45**, 3688 (1974)
- ⁸⁴ D. F. Nelson, P. D. Lazay and M. Lax, *Brillouin Scattering in Anisotropic Media: Calcite*, PRB, Vol. 6, No. 8 (1972)
- ⁸⁵ Chen X. *et al.*, *Macroscopic invisibility cloaking of visible light*, Nat. Commun. **2**:176 doi: 10.1038/ncomms1176 (2011)
- ⁸⁶ B. Zhang, Y. Luo, X. Liu, and G. Barbastathis, *Macroscopic Invisibility Cloak for Visible Light*, PRL **106**, 033901 (2011)
- ⁸⁷ G. Ghosh, *Dispersion-equation coefficients for the refractive index and birefringence of calcite and quartz crystals*, Optics Communications **163**, 95–102 (1999)
- ⁸⁸ D. W. Thompson, M. J. DeVries, T. E. Tiwald, J. A. Woollam, *Determination of optical anisotropy in calcite from ultraviolet to mid-infrared by generalized ellipsometry*, Thin Solid Films **313-314**, 341-346 (1998)

Thèse de Doctorat

Mariusz LEJMAN

Photogénération et Photodétection Ultrarapide de Phonons Acoustiques Cohérentes dans le Ferroélectrique BiFeO₃

Ultrafast Photogeneration and Photodetection of Coherent Acoustic Phonons in Ferroelectric BiFeO₃

Résumé

La technique d'optique ultra-rapide pompe-sonde, qui repose sur l'emploi de lasers à impulsion ultra-courte (femtoseconde), permet de déclencher et étudier des processus ultrarapides dans la matière. L'acoustique picoseconde concerne pour sa part l'étude des processus de génération et détection de phonons acoustiques haute fréquence ainsi que l'analyse des nanomatériaux avec ces phonons (nanoéchographie).

Les travaux de recherche de cette thèse avaient pour but l'étude des couplages électron-phonon acoustique dans le matériau ferroélectrique BiFeO₃ par acoustique ultrarapide. Nous avons pu mettre en évidence que selon l'orientation du cristal photo-excité, l'émission des phonons acoustiques cohérents longitudinaux (LA) et transverses (TA) pouvait être modulée. De manière spectaculaire, nous avons pu révéler un couplage électron-phonon acoustique transverse très efficace comme cela n'avait jamais été observé jusqu'alors dans les métaux, semi-conducteurs ou nanostructures artificielles. Une étude détaillée indique que le mécanisme piézoélectrique inverse semble être le moteur de ce couplage électron-phonon (Lejman et al, *Nature Communications*, 2014).

Dans une seconde partie, nous avons montré que BFO, ainsi qu'un autre ferroélectrique biréfringent LiNbO₃ (LNO), peuvent être utilisés pour la conversion de mode ultra-rapide par processus acousto-optique (manipulation de la polarisation de la lumière à l'échelle de la picoseconde avec des phonons acoustiques). Cet effet, jamais mis en évidence jusqu'alors dans le domaine GHz, pourrait potentiellement être exploité dans de nouveaux dispositifs photoniques/phononiques pour des modulations acousto-optiques à haute cadence.

Mots clés
Phénomènes ultra-rapides, Phonons,
Ferroélectriques, Acoustique picoseconde

Abstract

Ultrafast optical pump-probe technique, by exploiting ultrashort laser pulses (femtosecond), allows to initiate and monitor ultrafast processes in matter. Picosecond acoustics is a research field that focuses on the generation and detection mechanisms of high frequency coherent acoustic phonons in different media, as well as on their application in testing of nanomaterials and nanostructures.

This PhD's research project was devoted to study of electron-acoustic phonon coupling in ferroelectric BiFeO₃ (bismuth ferrite, BFO) by ultrafast acoustics. We have evidenced that depending on the BFO crystal orientation it was possible to tune the coherent phonons spectrum with in particular variable amplitude of longitudinal (LA) and transverse (TA) acoustic modes. In some grains with particular crystallographic orientations much stronger TA than LA signal was observed. Spectacularly, we have revealed an efficient coupling between electron and transverse acoustic phonon. Such high ratio never reported before in any metal, semiconductor or nanostructure before, can be principally attributed to the photoinduced inverse piezoelectric effect (Lejman et al *Nature Communications* 2014).

In a second part, we have shown that BFO as well as another birefringent ferroelectric LiNbO₃ (LNO) can be used for ultrafast acousto-optic mode conversion (manipulation of light polarization at the picosecond time scale with coherent acoustic phonons). This effect, never reported at GHz up to now, can be potentially applied in photonics for ultrafast manipulation of light polarization by coherent acoustic phonons in next generation photonic/phononic devices.

Key Words
Ultrafast phenomena, Phonons, Ferroelectrics,
Picosecond acoustics